Nutzung von Lorentzkräften für Mischprozesse in der Chemie- und Glasindustrie

DISSERTATION

zur Erlangung des akademischen Grades

DOKTORINGENIEUR

(Dr.-Ing.)

vorgelegt der

Fakultät für Maschinenbau der

Technischen Universität Ilmenau

von Herrn

M.Sc. Jose Oskar Torres Perez

geboren am 14.02.1979 in Lima/Peru

1. Gutachter: Dr.-Ing. Bernd Halbedel
2. Gutachter: Univ.-Prof. Dr. rer.nat. habil. André Thess
3. Gutachter: Prof. Dr.-Ing. Egbert Baake

Tag der Einreichung: 06.07.2016

Tag der wissenschaftlichen Aussprache: 21.12.2016

urn:nbn:de:gbv:ilm1-2016000844

Zusammenfassung

Gegenwärtig werden in der Glas- und Chemieindustrie mechanische Rührer zum Mischen, Homogenisieren und zur Fluidbewegung eingesetzt. Nachteile sind der mechanische Verschleiß und die damit verbundene Verunreinigung des Fluids – insbesondere bei chemisch korrosiven Fluiden und höheren Temperaturen (Schmelzen). Hinzu kommt, dass die Strömungs beeinflussungen örtlich limitiert sind. In elektrisch leitfähigen Fluiden kann die Lorentzkraft mechanische Rührer ersetzen.

Ziel ist es, mittels Simulationen und Experimenten zu zeigen, dass die Lorentzkraft die Strömung von Glasschmelzen trotz ihrer niedrigen elektrischen Leitfähigkeit und großen Viskosität beeinflussen kann. Dazu ist es erforderlich, den Wärme- und Stofftransport in schwach Ionen leitfähigen Fluiden, wie Glasschmelzen und Salzlösungen, unter dem Einfluss von elektrischen und magnetischen Feldern zu modellieren sowie die dafür notwendigen Elektroden- und Magnetsysteme für Anwendungen in der Chemie- und Glasindustrie auszulegen und deren Design zu optimieren.

Die Bearbeitung erfolgt in drei anwendungsnahen Projekten.

Im Projekt I zeigte sich, dass in laminar strömenden, hochviskosen Fluiden mit einer Drei-Elektroden-Anordnung und mit einem axialen Magnetfeld schon die erforderlichen Streckungen und Faltungen von Inhomogenitäten erzeugt werden, aus denen sich Mischungsgrade ergeben, die von mechanischen Rührzellen erzielt werden.
Die Simulationsergebnisse wurden mit Experimenten überprüft und dann auf reale Anordnungen übertragen.

Im Projekt II wurden mit numerischen Studien für einen realen Färbefeeder die optimale Anordnung von aus in die Glasschmelze hineinragenden Elektroden und dazwischenliegenden, aber im Isoliermaterial des Feederbodens angeordneten Spulen und deren Betriebsparameter ermittelt. Die Elektroden-Spulen-Anordnung erzeugt in der Glasschmelze eine Lorentzkraftverteilung, die die Sedimentation der Fritten (in Glas gelöste Metalloxide) reduziert und die Einströmbedingungen in die Rührzone verbessert.

Im Projekt III wurde eine ausreichende Fluidbewegung einer wässrigen Salzlösung bereits mittels zwei Elektroden und eines extern erzeugten magnetischen Feldes erzeugt.
Zur Bewertung der Mischverhältnisse waren geeignete Turbulenzmodelle zu prüfen, da die Strömung turbulent ist.

Abstract

Currently, mechanical stirrers are used for mixing and homogenizing fluids in the glass and chemical industries. Disadvantages are the mechanical wear and the associated contamination of the fluid, particularly in corrosive fluids and in high temperatures. In addition, the influences on the flow are locally limited. In conducting fluids, the mechanical stirrer can be replaced by the Lorentz force.

The aim of this work is to show by means of simulations and experiments that the Lorentz force can influence the fluid flow in spite of its low electrical conductivity and high viscosity in the case of molten glass. For this purpose, it is necessary to model the heat and mass transport in weakly ionic conductive fluids such as molten glasses and salt solutions, under the influence of electric and magnetic fields. Also, it is necessary to design and to optimize the electrode and magnetic systems for applications in the chemical and glass industries.

This PhD thesis is divided in three research projects.

The project I, shows that in laminar flow, highly viscous fluids can be stretched and folded by the Lorentz force with an arrangement of three electrodes and an axial magnetic flux density of 28 mT, obtaining similar blending levels as achieved with a mechanical stirring cell. The simulation results are validated with experiments and then transferred to a real configuration.

The project II, shows that the Lorentz force can be used to prevent the sinking process of the frits (dissolved metal oxides used to color the glass) within the molten glass flow, reducing the sedimentation and also enhancing the input flow condition of the stirring battery used to homogenize the color. For that purpose, an optimal arrangement of three electrodes and two coils are used. The numerical model of a real forehearth coloring is validated with temperature measurements in the molten glass as well as on the surface of the structure.

The project III, shows that the Lorentz force can be used to create a main azimuthal flow in turbulent regime of an aqueous salt solution. For that purpose, and arrangement of two electrodes and an axial magnetic flux density of 10 mT is used. To evaluate the mixing process, several turbulence models are examined.

Acknowledgements

Since the moment that I started my PhD, I always had the support and encouragement of my supervisor Dr. Bernd Halbedel and Prof. André Thess.

The expertise, encouragement and guidance of my direct supervisor Dr. Bernd Halbedel, made possible to accomplish this PhD thesis.

I would also like to extend my gratitude to all my colleagues of the Department of Inorganic-Nonmetallic Materials under the direction of Prof. Edda Rädlein and to the Research Training Group (RTG) ”Lorentz Force Velocimetry and Lorentz Force Eddy Current Testing” , for supporting my work.

Also, I express my gratitude to Henning Schwanbeck and Maik Rosenberger from the Technische Universität Ilmenau, for the support in using the high performance computing facility and to provide the necessary tools (e.g. position control unit) to accomplish my experimental work respectively.

Finally, I am very grateful for the support and understanding of my wife Hanna Nordblom and my family in Peru during all these years, as well as for her help during the English correction of my thesis.

This thesis was funded by Deutsche Forchungsgemeinschaft (DFG) and by the German Academic Exchange Service (DAAD).

Contents

CHAPTER I

General introduction

This chapter shows in section 1 a short general motivation of the work made in this Ph.D. thesis about the electromagnetic control of fluids with low electrical conductivity that has not yet being used in the glass and chemical industry. Section 2 shows the main objectives of this thesis and section 3 presents a short overview of the projects developed to achieve the goals imposed in the objectives.

1 Motivation

In the glass and chemical industry there are some processes, that require a better control of the fluid flow. These could be realized by changing the geometry such as adding a wall in the glass melting tank to increase the residence time [75] or by means of a mechanical stirrer to enhance the homogenization that cannot be achieved by natural diffusion needed for example, in the coloring of molten glasses [73, 72], in the production of optical glasses [67, 68, 69] or in the crystallization processes of inorganic materials [71]. Processes such as coloring of molten glasses in forehearths where the minerals used to give the color have a tendency to sink and therefore are not possible to control with standard techniques such as temperature gradients, bubbling or barriers [72, 73].

Some disadvantages appear when using the standard techniques such as the mechanical wear of the mechanical stirrer that contaminates the fluid, particularly in chemically corrosive fluids and in high temperatures. Also, another drawback of the mechanical stirrer is its local action around its impeller blades.

This Ph.D. thesis proposes an alternative novel technique called the Lorentz force technique. It is based on the non negligible electrical conductivity of molten glasses and chemical solutions to generate the Lorentz force and thus to influence and control the flow of those fluids. This contactless control, due to absence of moving parts, is used to mix those fluids without the drawbacks of the mechanical stirrer as well as to push up the fluid avoiding the sinking process of the minerals used to color glasses.

Up to now there are not industrial applications of the Lorentz force in the production of glasses nor in the crystallization of inorganic low conductive solutions but, there exist experimental as well as numerical investigations using a laboratory scale physical model, [6], [7], [5].

2 Objectives

The objectives of this Ph.D. thesis is to show by means of numerical simulations and experiments that the Lorentz force can influence the fluid flow of molten glasses and chemical solutions in spite of their low electrical conductivity ($< 100\,S/m$) [69], [71], compared to liquid metals ($\approx\ 10^6\,S/m$) [4], and in a large range of viscosities. For this purpose, it is necessary to model the heat and mass transfer in such fluids under the influence of electric and magnetic fields as well as to design and optimize the suitable electrode and coil arrangements. Attention has to be given to the temperature dependence of the physical properties (conductivity, viscosity, density), leading to a nonlinear coupling of mass, heat transfer and electric fields, and also to the thermal boundary conditions in each application case where the Lorentz force technique is studied.

3 Overview of the thesis

3.1 Overview

The study of the Lorentz force technique application is developed in three main projects:

- Project I: Electromagnetic mixer
- Project II: High-performance Forehearth Coloring using Lorentz Forces
- Project III: Electromagnetic crystallizer

Each project follows the same analysis strategy. First of all, the description and simplification of the problem is made in order to carry out a first analytical study. When the complexity of the problem is increased, the numerical computations of the coupled partial differential equations describing the electrodynamics, the heat transfer and the fluid mechanics of the given problem are made using the commercial computational fluid dynamics software FLUENT [2] and / or the open source software OpenFOAM [3]. Finally, the validation of the numerical results is carried out with experimental measurements.

3.2 Electromagnetic mixer

The project is a proposal to the glass industry of a new technique to homogenize the molten glass that has the advantage of static parts and more precise flow control by means of electrical parameters. The disadvantages of the actual technique that uses a mechanical stirrer to homogenize the molten glass are the formation of undesirable particles due to the mechanical wear, produced mainly in the moving parts, and an expensive sophisticated design made of platinum or platinum alloy, increasing the process costs.

The electromagnetic mixer consist of a special electrode arrangements and activation, generating time- as well as space-dependent electric current density in the molten glass. Such current density together with an externally created magnetic field, oriented axially, create a Lorentz force density distribution which depends also on time and space, and is used to control the flow. The high viscosity of the molten glass (1-100 Pas), which depends on the glass composition, together with its low flow velocities (mm/s -cm/s) give an small Reynolds number, meaning that the fluid flow is in laminar regime and it can be stretched and folded (necessary condition for the mixing) by the Lorentz force. Nevertheless, the Lorentz force technique has some limitations such as:

- The maximum increment on the glass temperature due to the Joule heating and therefore a limitation on the electric current density.
- The corrosion of the electrodes that limits also the electric current density to prevent or reduce that process.
- The high viscosity of the molten glass which increases the friction force and consequently reduces the influence of the Lorentz force in the molten glass.

The first part of the study is focused on the numerical analysis of a physical model exploring the mixing capabilities of a highly optimized mechanical stirrer provided by SCHOTT AG Mainz [1] and of the electromagnetic mixer developed in a previous work made by Sugilal Gopalakrisnan as an extension of Aref's blinking vortex model [19]. The potential of this new technique is proved comparing its stirring index, parameter that quantify the homogenization degree using the spatial distribution of passive particles, with that of the mechanical stirrer.

The second part of the study is the experimental validation of the numerical results comparing their stirring indices. The stirring index is determined experimentally using a camera-laser system that records the position of micro particles introduced in the physical model and a self-developed image processing technique. The third part of the study is the scale up of the validated model to a real plant. For that, it is necessary to introduce the heat transfer in the model.

3.3 High-performance Forehearth Coloring using Lorentz Forces

This project originates from the collaboration between the Technische Universität Ilmenau and FERRO GmbH in Frankfurt to develop a method/ technique of High-performance Forehearth Coloring using Lorentz Forces.

In the start-up project together with the FERRO's partner Iittala Glass Factory/ Finland, a numerical model for the simulation of the heat and mass transport under the influence of electric and magnetic fields is developed to show the feasibility of the Lorentz force technique using a realistic technical configuration of the electrode arrangements and magnetic system in a small forehearth ($\approx$ 2 t/d) to prevent the sinking process of the minerals [63].

Based on the numerical results of the first project, a second project is developed between the Technische Universität Ilmenau, Ferro Frankfurt and Ferro France S.A.R.L. as well as O-I GLASSPACK GmbH & Co. KG Rinteln. It should also be observed in a larger forehearth ($\approx$ 80 t/d) that the minerals (frits) used to color the molten white glass tend to sink, degrading the glass coloring, because the stirring battery needs a certain frits level to perform a good homogenization, and contaminating the lower part of the molten glass when they sediment. The main focus of the second project is to scale-up and validate with temperature measurements the numerical model to later study the push effect created by the Lorentz force to prevent the sinking process and thus to improve the input flow conditions of the stirring battery [64].

3.4 Electromagnetic crystallizer

This project is a proposal to the chemical industry of a new technique for crystallizing inorganic material (liquid solution) as a replacement of the mechanical stirrer used for the mixing process. Good mixing of the solution, in both global and local scales, is required to enable sufficient mass transfer needed for achieving desired crystal growth rate. But the mechanical wear (introduction of foreign particles producing undesirably advanced nucleation), and its local flow influence (poor mixing in far regions) are some disadvantages of the traditional technique.

To overcome these problems, the Lorentz force technique can replace the mechanical stirrer used in inorganic solutions (electrolytes). The advantage of the Lorentz forces is that the velocity flow is generated by means of volumetric forces in the solution, spreading in the whole volume having a better impact on the homogenization, instead of shear stress forces on the interface between the stirrer and the solution. But the Lorentz force technique applied on chemical solutions is also not exempt of limitations. The maximal current that is possible to apply and therefore the maximum value of the Lorentz force is limited by the material used in the electrodes as well as by the maximal current that is possible to apply in chemical solutions such as aqueous solution, before the ignition of the water electrolysis.

Unlike the study in section 3.2 and section 3.3, here the study is focused on the analytical and numerical computation of the velocity flow field from the laminar to the turbulent regime controlled with the magnitude of the Lorentz force while the viscosity of the solutions is very low, approximately like water. Different RANS turbulence models are analyzed and compared with a more accurate model (LES) but more demanding in terms of computational resources. The RANS model that copes the LES results is the $k-\omega$ SST and it is used to compute the mixing capabilities of the Lorentz force. Finally the design of the physical model is realized to validate in a further study the numerical results.

4 Summary

This Ph.D thesis is divided in three main projects. The first one is the continuation of the numerical work made by Sugilal Gopalakrishnan [19] and the experimental work made by Uwe Krieger [12] to propose to the glass industry a novel technique called Lorentz force technique for the mixing process needed in the production of optical glasses and coloring glasses without the problems found in the current technique.

The second project supported by our industrial partners, investigates the push up effect created by the Lorentz force in the molten glass flow to avoid or reduce the sinking of the minerals used for coloring glasses. Until now, there is no technique that can resolve this problem.

The third project analyzes the mixing capabilities of the Lorentz force technique in chemical solutions. Difference to the first two projects, where the molten glass flow is in laminar regime, here the chemical solution flow is in turbulent regime. Therefore, it is necessary to investigate several turbulence models and then to propose an experimental design for their validations.

The physical system that is defined by the analyzed region in each project must be simplified in order to describe it with a mathematical model. These simplifications are made in the physical properties of the fluid that cannot be measured, in the internal chemical reactions, in the exchange of matter with the surrounding as well as in the geometry.

The mathematical model that describes the action of the Lorentz force in the fluid flow is composed of coupled differential equations which are computed numerically with well validated numerical codes such as the commercial software ANSYS / FLUENT [2] and the open source software OpenFOAM [3].

CHAPTER II

State of the Art

This chapter shows in section 1 the state of the art in the application of Lorentz forces to molten glasses as well as in inorganic solutions. The section 2 presents the manufacturing process of glasses with a special attention to optical and coloring glasses.

1 Lorentz Force Applications in Electrolytes

1.1 Overview

This section shows the state of the art of the application of Lorentz forces to control the fluid flow of electrolytes such as molten glasses and inorganic chemical solutions which are used as a basis or support of the different projects developed in this thesis.

1.2 Control of molten glass flow

The study of the applications of Lorentz forces to control the molten glass flow goes back to the early investigations of Osmanis et al. in 1984 [6]. The investigation showed that Lorentz forces can improve the homogeneity of molten glass, but that study didn't make a direct measurement in the molten glass which could be helpful for understanding the Lorentz force effect in the velocity and temperature fields of the molten glass.

In the period 2001 - 2009, the Magnetofluiddynamics research group of the Technische Universität Ilmenau funded by Prof. André Thess, performed a direct measurement of the temperature distribution and density variations using an electric current density in the molten glass between 5-20 mA/mm^2 and an externally generated magnetic flux density of 44 mT to explore the effects of Lorentz forces on the homogeneity of the molten glass under the direction of D. Hülsenberg, B. Halbedel, et al. [6]. As well as an image analysis of the striae formation in glass during the stirring process with calculated mean velocities between -1.5 mm/s and 8.3 mm/s using a magnetic flux density of 42 mT, an electric current density of 1-2 A/cm^2, to proof that the Lorentz force can stir the molten, made by U. Krieger et al. (Fig. II.1) [7, 12]. Also, analytical studies with a one-dimension model [8] as well as numerical studies with a three-dimension model [9] were performed to show the temperature and velocity field of the molten glass during the mixing process.

The success of these researches formed the basis for a cooperative relationship between the glass manufacturers, particularly SCHOTT AG and the Technische Universität Ilmenau. From this fertile collaboration emerged a joint patent, C. Kunert et al. Aktenzeichen DE 102004015055 [15] and B. Halbedel et al. WO 2007065937 [16], a joint publication in the journal Physics of Fluids [8], as well as two dissertations from Cornelia Griessler [11] and Uwe Krieger [12].

These previous works, that clearly demonstrated that the externally applied electromagnetic field connected with an electric current density in the glass melt impressed about electrodes can effectively control the glass melt flow. These together with the studies made by SCHOTT AG [10] are used to numerically illustrate that chaotic mixing, controlled by electromagnetic means, can effectively improve the glass melt homogenization through repeated stretching and folding of the fluid layers, facilitating the mixing by diffusion [17], [18] and [19].

Also, at the Technische Universität Ilmenau, in colaboration with [75], the application of the Lorentz force to control the molten glass in melting tanks with electromagnetic boosting is studied. This is used to increase the convection flow, which in return help to separate the melting zone from the fining zone. It was shown numerically that the Lorentz force enhance the electromagnetic boosting, creating an electromagnetic wall [75].

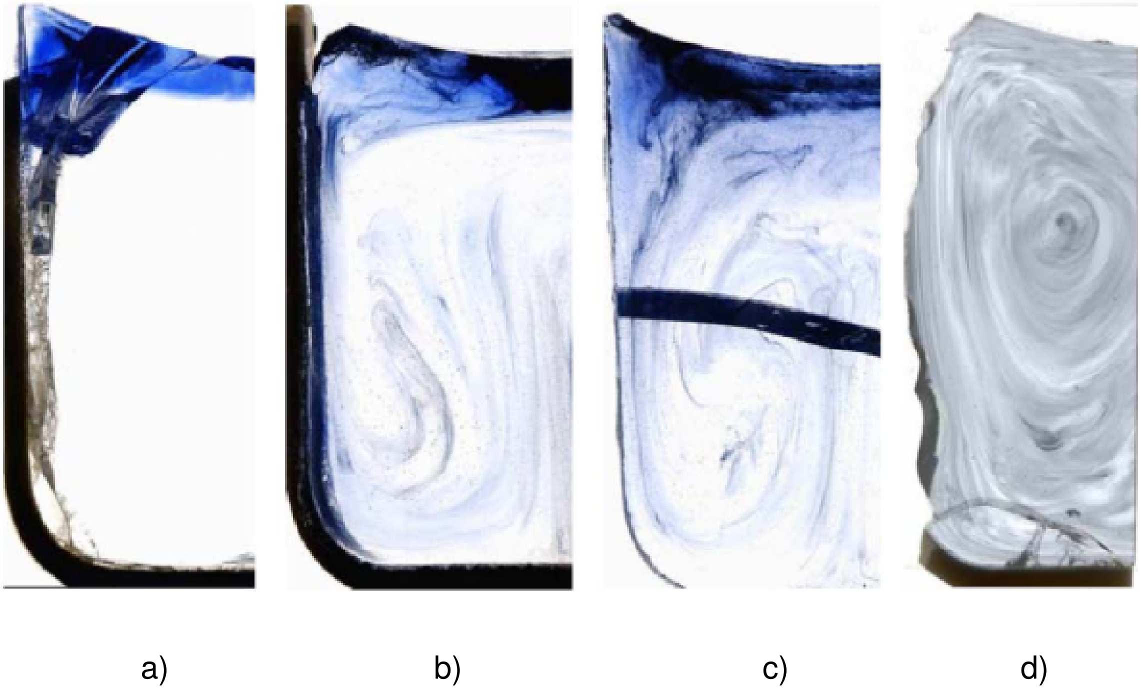
a) b) c) d)

Figure II.1: Images courtesy of Krieger et al. [7], visualizing the electromagnetic stirring effects in a crucible filled with a siliceous molten glass colored with CoO on the top. a) Effect of electric heating after 5 min. b) Effect of electric heating after 25 min. c) Effect of electric heating and Lorentz forces after 5 min. d) Effect of electric heating and Lorentz forces after 25 min.

1.3 Control of inorganic chemical solutions flow

The studies of the Lorentz force applications to control inorganic chemical solution flow are mainly found in microfluidic devices such as lab on a chip devices used to conduct chemical and biochemical analysis.

One of the necessities of those devices is the transport of chemical solutions that can be made by electromagnetic micropumps. In [20], the electromagnetic micropump is made of electrodes located inside the device in contact with the fluid operating in DC mode and of an external permanent magnet. The electric current density impressed in the fluid by the electrodes interacts with the magnetic flux density created by the magnet, producing a Lorentz force density pointing to the desired direction (Fig. II.2.a). This force drives the fluid with a voulmetric flow rate of 2.5 μL/min, using a magnetic flux density of 490 mT and an electric current of 5 mA. The advantage of the DC mode is the use of permanent magnets for the generation of a magnet field which doesn't require a connection to a power supply. But, in microfluidic devices using aqueous fluids, this configuration is not adequate because the voltage applied on the electrodes generates electrolysis. The consequence of that, are bubbling creation as well as the corrosion of the electrodes reducing their life time and contaminating the fluid.

To overcome these problems, [21] and [22] proposed to add to the fluid electroactive redox species increasing the electrical conductivity and decreasing the necessary voltages on the electrodes, and thus to reduce the electrolysis and its drawbacks.

Also, another solution to avoid the electrolysis was investigated by [23]. Here, the electrodes are in AC mode and they are synchronized with the phase shift of an electric current applied on an electromagnet, to keep the Lorentz force pointing in the same direction (Fig. II.2.b). This force drives the fluid with a velocity of 1.51 mm/s in the center of the channel using a magnetic field density of 18.7 mT and an electric current of 140 mA. In the AC mode the bubbling threshold depends on the electric current frequency at the same time decreasing the magnetic flux density.

Another necessity in microfluidic devices is the mixing of two or more species. Typically these devices work at low Reynolds number, where turbulent mixing does not occur and hence molecular diffusion of the species plays a major role on the mixing process. Nevertheless, the slowness of the process is not suitable for the microfluidic devices. One way to overcome the problem is to use Lorentz forces to enhance the mixing. In [24], the Lorentz forces, which are generated with electrodes in DC mode using a voltage of 4 V and neodymium permanent magnets with typically magnetic flux densities between 300 mT - 400 mT, are used to create secondary flows that may enhance mixing by changing the polarity of the electrodes and thus the direction of the Lorentz forces.

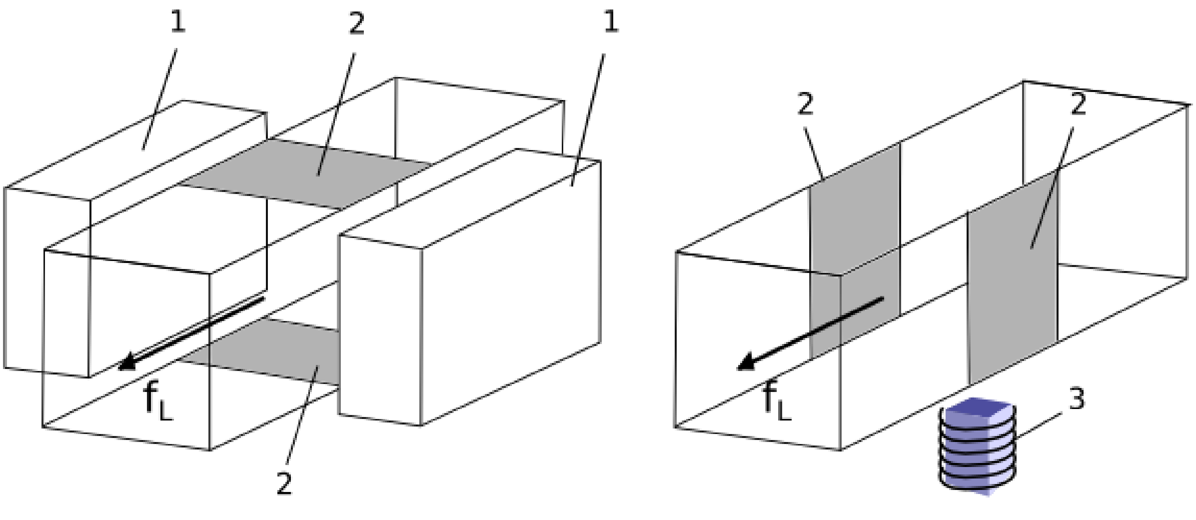

a) b)

Figure II.2: Schematics of the electrode and magnetic system to create the Lorentz force density $\mathbf{f}_{\mathrm{L}}$ and thus to pump the solution. 1- permanent magnets, 2- electrodes, 3- electromagnet. a) Lorentz force density created with electrodes working in DC mode and permanent magnets. b) Lorentz force density created with electrodes working in AC mode and an electromagnet.

A better enhancement of the mixing using Lorentz forces, was provided in the study made by [25] that was inspired by the Aref blinking vortex model as it was also in the study made by Gopalakrisnan et al. [19] to create chaotic advection using an arrangement of three electrodes. Here also the Lorentz forces were created with the electrodes working in DC mode using a voltage between 0.3 V - 7 V and permanent magnets with magnetic flux densities of 300 mT.

2 Melting and coloring in the glass industry

2.1 Glass definition

There exist several definitions of what is glass, depending from which area of study come from as well as in which period was made. One of them is found in the German standard "Glas ist ein anorganisches Schmelzprodukt, das im wesentlichen ohne Kristallisation erstarrt" saying that glass is an inorganic product of fusion that solidifies without crystallizing [37]. Here that definition is extended to take into account also organic materials used in the composition that exhibit a glass transition.

Generally, in the process of cooling a melted material, the liquid state can solidified glassy or crystalline (Fig. II.3). If the solidification is connected with a continuous not jumped decreasing of the volume (supercooling) then glass is formed (Fig. II.3.b). Its viscosity decrease until a transformation range η = 10^{12} Pas - $10^{13.5}$ Pas [28, 12], which defines the transformation temperature T_g. There, the curve deviates, and below this point the material is called glass and considered that it is in solid or glassy state without having a clear phase change because it has retained its disordered nature from the liquid state. If the rate of cooling is enough slow, the crystallization takes place at the melting point T_m where a clear phase change from liquid to solid happens [37], [40].

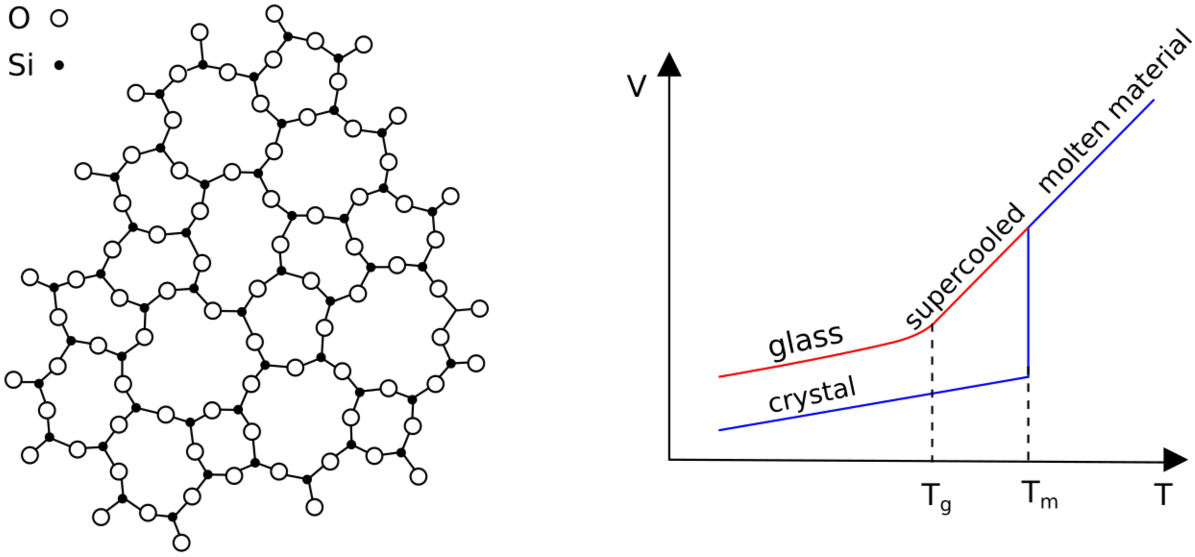

a) b)

Figure II.3: a) Two dimensional schematic of a random SiO_2 network according to Zachariesen [33], [34]. b) Schematic of the temperature - volume diagram for the cooling process of a molten material to the glassy material or to a crystallized material.

Glasses in solid state have a short range order on the Angstrom scales but no large range order as in crystals as was schematized by Zachariasen in his random network model (Fig. II.3.a) [33], [34]. Therefore no Bragg peaks has been seen in diffraction experiments [38].

The mechanical and optical properties of glasses depend on their chemical compositions, melting processes and thermal treatments which can vary widely opening a wide range of applications such as packing, tableware, automotive, construction, electronics, medical technology, optics and others.

The chemical composition also defines the physical properties of the molten glass such as the density, viscosity and electrical conductivity, depending strongly on the temperature. During the increment of the temperature, the electrical conductivity increases while the viscosity and the density decrease and accordingly, the mobility of the ions as well as the volume enlarge, meaning that for the same working temperature tow different compositions will behave differently to the action of the Lorentz forces. The one with a large viscosity will oppose more to the modification of its flow, while the one with a large electrical conductivity will allow the creation of more intense Lorentz forces and additionally the Lorentz force decreases while the electrical conductivity also decreases.

The temperature dependence of the viscosity η is well described by the Vogel-Tammann-Fulcher (VTF) equation,

$$lg(\eta) = A_\eta + \frac{B_\eta}{T - T_0} \tag{II.1}$$

where A_η and B_η are fitting constants and T_0 an arbitrary parameter. According to [27], the VTF is useful to describe the behavior of the viscosity when $T > T_g$ + 50 K. Also, the electric conductivity σ follows an exponential temperature dependence [51, 12], which is described by the Eq. II.2 written in logarithmic form,

$$lg(\sigma) = A_\sigma + \frac{B_\sigma}{T} \tag{II.2}$$

where A_σ and B_σ are fitting constants.
Otherwise, the temperature dependence of the density ρ has a linear behavior [12, 53],

$$\rho = A_\rho + B_\rho T \tag{II.3}$$

where A_ρ and B_ρ are fitting constants.

The other physical properties, such as thermal conductivity and thermal capacity can be considered constant because they change little in the range of the molten glass temperatures [12].

These physical properties are important for the production of glasses because, e.g. the forming temperature is determined by the viscosity, the weight of the final product is determined by the density, as well as the improvement of the temperature homogenization using electrodes and the necessary or possible amount of directly electrical heating is determined by the electrical conductivity.

2.2 Glass production

The glass industry production in the year 2014 for the European market is divided in five main sectors [33], [39].

- Container glass, e.g. for glass packing products which represents about 70 %.
- Flat glass, e.g. for building and automotive industries which represents about 25 %.
- Glass fiber, e.g. for composite materials which represents about 2%.
- Domestic glass, e.g. for tableware which represents about 2 %.
- Special glass, e.g. for optical glass which represents about 1%.

Following the classification established by Zachariasen for the composition of glasses, there are three groups, the network formers, which are the base raw materials, (e.g. silica (SiO_2), cullet), the network modifiers used, e.g. to decrease the melting point (e.g. soda (Na_2O), lime

($CaCO_3$)) and the intermediate oxides used as, e.g. coloring/decoloring agents (e.g. iron oxide (Fe_2O_3)) [41], [35], which are mixed in proper proportion called batch [41].

The batch charging is introduced mechanically into the melting tank (see Tab. II.1) quasi-continuously and melted with burners located along the side walls (see Tab. II.2), cross-fired system, or at the end of the melting tank, end-fired system, using mainly natural gas or fuel oil and / or electric energy for all or only additionally electrical heating respectively to form the molten glass that happens at temperatures around 1500 ^{o}C (Fig. II.4).

During this process, two main convection flows are generated. One brings the molten glass to the batch region enhancing the melting process and the other is responsible for the removal of gas bubbles and dissolved gases, which when necessary, the convection flows can be enforced using a bubbler system, electrical booster or a wall.

The conditioning at the required thermal homogeneity and therefore viscosity of the molten glass is made in the forehearth that connects the melting tank with the forming machine (Fig. II.4) [42].

Table II.1: Typical geometrical data of melting tank for continuous glass furnace [52]

Length [m]	Width [m]	Glass level [m]
8-40	5-15	0.6-1.8

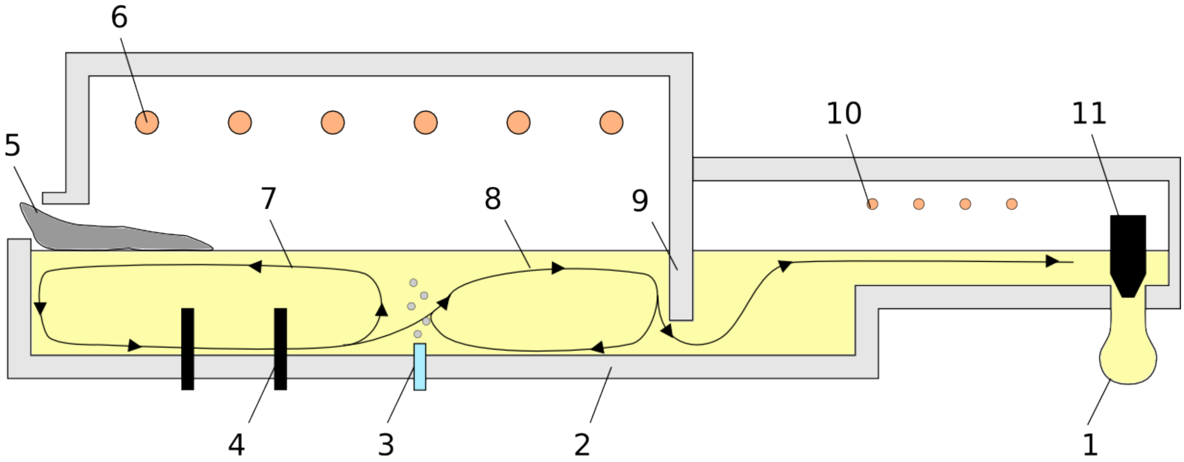

Figure II.4: Schematic of a cross fired glass melting tank with an additional electrical heating in the melting zone and a bubbler in the spring zone, and a forehearth. 1- Gob forming, 2- layer of refractory and insulating material, 3- bubbler, 4- electrodes, 5- batch charging, 6- cross-fired burners, 7- zone of batch melting, 8- fining zone, 9- throat, 10- forehearth burners, 11- plunger.

Typical container glass like beer or wine bottles doesn't need an homogenization enhancement because the color comes from the composition of the batch and/or cullet.

However, in novel container glass tanks the coloring is not done in the tank, but directly in the forehearth by means of colorants (minerals or concentrates) [47]. Here, when a non standardized color (e.g. perfume industry) or a low striae content (optical glass) are required, the natural diffusion is not enough to homogenize the melt or to reduce the striae content, therefore mechanical stirrers are needed to improve the mixing already started by this natural diffusion (see section 2.4).

Table II.2: Furnace type [52]

Furnace type	Glass type	Glass pull rate [t/d]
Regenerative cross fired	Float glass	500 - 1000
Regenerative cross fired	Container glass, tableware	100 - 600
Regenerative end port fired	Container Glass, tableware	100 - 400
Recuperative cross-fired	Fiber glass, tableware container glass	20 - 400
Oxy-fuel (cross-fired)	Fiber glass, tableware, container glass	1 - 400
Oxy-fuel (cross-fired)	Float glass	500 - 800

2.3 Optical glass

Currently, there exits more than 100 optical glass types [43] which are produced in a large range of compositions, melting processes and thermal treatments depending on its application that goes from the infrared to the ultraviolet spectrum [32]. Typically crown glass (soda-lime silicates) or flint glass is used as a base glass to which is added other materials, e.g. borosilicate glass Schott BK7 that is based in crown glass and is used in lens [43].

Optical glasses need to have high spatial homogeneity of refractive index [54], very low striae content and bubble concentration [55]. These requirements are achieved by using platinum or platinum alloys in crucibles or forehearths as well as in stirrers to reduce the impurities found when using other materials (Fig. II.4.b) [30]. These stirrers smooth out the inhomogeneities (striae) that are mainly produced in an unfinished homogenization or by contamination in the melting tank [31], [32]. To achieve the high levels of homogeneity needed in these glasses, the complete volume of the molten glass has to be forced to cross the rotation plane of the stirrers, therefore the molten glass flows parallel to rotation axis of the stirrer (Fig. II.5 (a)).

The stirrer design and composition depends on the glass properties such as viscosity, chemical composition and in its application. To reduce the contamination due to corrosion, high-resistant platinum or platinum alloys is used as a bulk material or as a coating with a core made of, e.g. molybdenum with an helical or coplanar design. Also this core helps to increase the durability of the stirrer that it is reduced by the shear stresses done by the molten glass which are proportional to its viscosity [45], [46].

In the installations of the industrial partner Schott AG, a coplanar design with several stages is used to homogenize the molten glass with a density of 2350 Kg/m^3 and a viscosity of 27 Pas using a pull rate of 1.4 t/d (Fig. II.5 (a)).

2.4 Coloring glass

As is described in section 2.2, traditionally, to give color to the glass, colorants were added to the glass tank, but since 1970 a new way of coloring glasses was introduced [47]. Instead of adding the colorants in the glass melting tank, they are added in the forehearth offering a better production flexibility because :

- several forehearths can be attached to one glass tank running different colors,
- changing the color in the forehearth is faster and cheaper (lower energy requirements) than in the glass tank,
- more colors (see Tab. II.3) are possible while the redox state can be changed,
- reduction of potential contaminants.

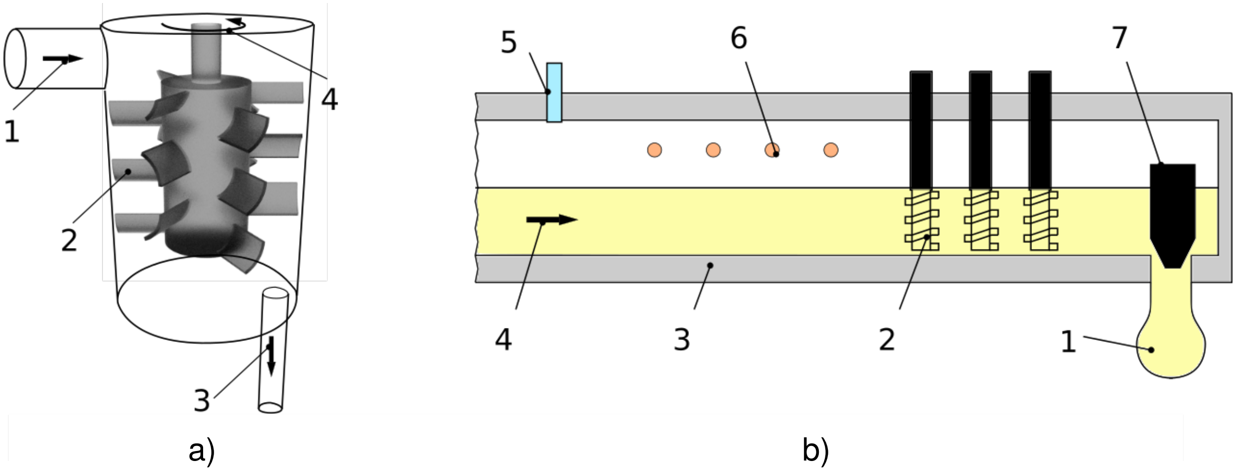

Figure II.5: a) Mechanical stirrer to homogenize the molten glass. Stirring design courtesy of the industrial partner Schott AG. 1- direction of the molten glass flow, 2- mechanical stirrer, 3- outflow, 4- counterclockwise rotation of the mechanical stirrer. b) Schematic of the forehearth with a battery of stirrers to homogenize the colorants. 1- Gob forming, 2- battery of mechanical stirrers, 3- layer of refractory and insulating material, 4- direction of the molten glass flow, 5- feed tube, 6- cross-fired burners, 7- plunger.

In order to give color to the molten glass, the forehearth has to be enlarged to include the colorant feeding, the melting of the colorant and after that the mixing of the melted colorant with the molten glass. The colorants are deposit on the surface of the molten glass through feed tubes melting and diffusing progressively, but this process is not enough to mix the melted colorants with the non colored molten glass, therefore a battery of stirrers is used to enhance the mixing (Fig. II.5.b) [29].

The traditional stirrer has an spiral design and its made of, e.g. molybdenum [48], alumino-silicate ceramic [45], and to enhance its durability can be coated with platinum [45]. The color of the glass depends on the redox of the added minerals (colorants) that normally are transition metals (e.g. Cr, Mn, Fe, Co, Ni, Cu) or rare earths (e.g. Y, La, Gb, Yb), the molten glass itself, as well as at which temperature it happen and how the heat transport distributes the temperature in the molten glass.

The pull rate of the molten glass can be as low as 2 t/d, e.g. in the installation of the industrial partner Iittala Glass Factory/ Finland [63] or up to 90 t/d, e.g. in the installation of the industrial partner O-I GLASSPACK GmbH & Co. KG Rinteln [64] with a maximum pull rate of 140 t/d reported in 2005 by [47]. The higher the pull rate is, less time the colorants have to melt and therefore a compromise between the colorant pull rate with the molten glass pull rate and working temperature must to be found.

Table II.3: Some coloring ions used to give color to the molten glass [49, 50]

Product	Coloring ion	Feed rate	Color loadings	Melt zone temperature [°C]
Smoke Grey	Ni	0.4 %	-	-
Ramlosa Blue	Co/Cu	0.8 %	-	-
Clearly Canadian	Co/Cu	0.5 %	-	-
Bacardi Limon	Ni/Co/Cr	0.25 %	-	-
Dead-leaf Green	Mn/Cr	1.00 %	-	-
Emerald green	Cr	-	up to 15 %	1230-1315
Brown	Ni	-	up to 17 %	1230-1315
Deep blue	Cu	-	up to 30 %	1220-1260
Green blue	Cu	-	up to 30 %	max.1220
Amethyst	Mn	-	up to 32 %	low as possible
Pink	Se	-	up to 1 %	1220-1250
Black	Cr/Mn	-	-	-

CHAPTER III

Theoretical Framework

In this chapter a brief description of the mathematical framework is shown in the section 1. Then, in the section 2, the generation of electric and magnetic fields to create Lorentz forces in weakly conducting fluids are explained. In the section 3, the Navier-Stokes equation describing the fluid flow under the influence of the Lorentz forces as well as the heat transport equation describing the heat transfer within the fluid is shown. Finally in the section 5, different mathematical tools to quantify the degree of homogenization produced by the Lorentz force as well as the mixing processes in laminar and turbulent regime are presented.

1 Introduction

The theoretical framework is composed of differential equations describing the different interactions within the physical system as well as constitutive relations describing the interaction with external fields. The studied system is comprised of electrically neutral matter, their interaction energies and it is defined by boundaries through which the system exchanges energy with the surrounding environment.

This Ph.D thesis deals with physical systems of macroscopic dimensions (in the order of meters), which are larger than the distance between molecules (mean free path) exchanging only thermal energy but not matter with its surrounding environment. At this scale, the matter is no longer granular but continuous allowing to sub-divide the system in small volumes (elementary volumes) with physical properties such as temperature and pressure as well as physical quantities such as mass and momentum that spread uniformly in the bulk matter. Therefore, the system can be modeled by differential equations that describe its behavior under the action of external fields, which are derived from fundamental physical laws such as the conservation of mass, the conservation of momentum, and the conservation of energy, as well as constitutive relations.

The interaction of the system with external fields is governed by the electromagnetism via electric and magnetic fields as well as by the gravitation. The gravitational field and its interaction with matter that carries mass, is described by the laws of motion established by Isaac Newton and published in 1687 in the book ”Philosophiae Naturalis Principia Mathematica”. The electromagnetic fields and its interaction with matter that carries electrical conductivity and also magnetic permeability, is described by a set of differential equations established by James Clerk Maxwell, published in 1864 in the paper ”A dynamical theory of electromagnetic fields” [80].

The focus of this Ph.D. thesis is on continuous electrically neutral conducting matter in liquid state with a magnetic permeability μ_0 of $4\pi \times 10^{-7} N/A^2$ under the action of time varying electric and magnetic fields with low frequencies, which is modeled with a set of differential equations known as the Navier-Stokes equations derived around 1840. The type of matter analyzed are electrolytes such as molten glasses and inorganic solutions that have low electrical conductivity mainly carried by ions ($< 100\, S/m$) compared to metals ($\approx 10^6\, S/m$) and a magnetic permeability of approx. same as vacuum μ_0.

2 Lorentz forces in electrolytes

The low electrical conductivity ($< 100\, S/m$) found in molten glasses and inorganic solutions (e.g. solved salts, acids and bases) reduces the capabilities to influence the flow motions of these fluids, because the electric currents induced by an externally created time varying low frequency magnetic field are negligibly small. Otherwise, the induced electric current densities can be enhancing by using high frequencies in the range of kHz up to MHz [81].

Therefore it is necessary to create additional time varying electric currents within these fluids to enhance the Lorentz force keeping the magnetic flux density low ($< 100\, mT$). It is important to notice that the creation of an electric current density in such fluids are only feasible by applying an electric potential difference about electrodes, located in the fluid, and consequently it carries a magnetic field called, *eigenfeld*, which also interacts with the impressed electric current density [13].

The time varying electric current density created in the fluid by the immersed electrodes must be tuned with the time varying external magnetic field in order to control the magnitude and direction of the Lorentz force. For this purpose, the external magnetic field is created by a time varying electric current density imposed on an group of coils located outside of the fluid by applying on it an electric potential difference.

Several configurations can be developed using the oscillation frequencies of these two electric current densities, one in the electrodes and fluid and the other in the coils, as well as the phase difference. From all of them, a configuration with same frequency and no phase difference is selected by the research group ”Electromagnetic Processing of Materials” under the direction of Bernd Halbedel of the Technische Universität Ilmenau [77].

This configuration produces a Lorentz force that points always to the same direction and it is created with electric currents that have an oscillation frequency of standard installation lines which run at a frequency of 50 Hz (Europe) defined by the norm DIN EN 60038 [14].

2.1 Electromagnetism

The behavior of the electric and magnetic fields is described by a set of equations known as Maxwell's equations that summarize the laws of electricity and magnetism, depending on the electrical conductivity σ, permitivity ε_e and permeability μ_0 (same as vacuum) of the fluid that they penetrate.

These equations are the Coulomb's or Gauss's law Eq. III.1 that is equal to zero because the studied fluids are electrically neutral ($\rho_e = 0$), the Ampère's law Eq. III.2 with the correction added by Maxwell, the Faraday's law Eq. III.3 and the solenoidality of the magnetic field III.4. The corrected Ampère's law includes two sources for the magnetic field; a steady state conduction current and a changing electric flux through any surface S bounded by path C.

$$\nabla \cdot \mathbf{E} = -\frac{\rho_e}{\varepsilon_e} = 0 \tag{III.1}$$

$$\nabla \times \mathbf{B} = \mu_0 \mathbf{J} + \mu_0 \varepsilon_e \frac{\partial \mathbf{E}}{\partial t} \tag{III.2}$$

$$\nabla \times \mathbf{E} = -\frac{1}{\mu_0}\frac{\partial \mathbf{B}}{\partial t} \tag{III.3}$$

$$\nabla \cdot \mathbf{B} = 0 \tag{III.4}$$

The quantities $\mathbf{E}$, $\mathbf{B}$, $\mathbf{J}$ and ρ_e correspond to the electric field, the magnetic flux density, the electric current density of free charges and the electric charge density respectively.

2.2 Electric current densities in the fluid created by the electrodes

The electric field, created by the electric potential difference applied on the immersed electrodes, oscillates at low frequencies ($50Hz << KHz$) with wavelengths large compared to the size of the studied systems ($\approx$ 1m), implying that the variation in time of the electric field can be neglected from the Eq. III.2. Therefore, the wave propagation mechanics is lost and the electric field propagates instantaneously.

The free ions of the electrically conducting fluids response to this electric field $\mathbf{E}$ as an electric current density $\mathbf{J}$ whose magnitude is determined by the electrical conductivity of the fluid σ. These quantities are related by constitutive relations such as the Ohm's law,

$$\mathbf{J} = \sigma \mathbf{E} = -\sigma \nabla \varphi \tag{III.5}$$

where φ is the electric potential.

The electric currents that flow in the fluid as well as in the electrodes carry a magnetic field, eigenfeld, described by the Eq. III.2 and illustrated by the Fig. III.1, which oscillate at low frequencies. Therefore their contribution to the electric field can be neglected from Eq. III.3, meaning that the electric field is expressed only in terms of the electric potential gradient as is shown in Eq. III.5.

The computation of the eigenfeld can be simplified rewriting the Eq. III.2 using the magnetic vector potential $\mathbf{A_{ef}}$ of the eigenfeld:

$$\nabla^2 \mathbf{A_{ef}} = -\mu_0 \mathbf{J} \tag{III.6}$$

and then computing the mangetic flux density of the eigenfeld with the relation:

$$\mathbf{B_{ef}} = \nabla \times \mathbf{A_{ef}} \tag{III.7}$$

The Biot-Savart equation, which is a solution of the Eq. III.6, is not used because the distribution of the electric current density in the fluid has not in general, an analytical form.

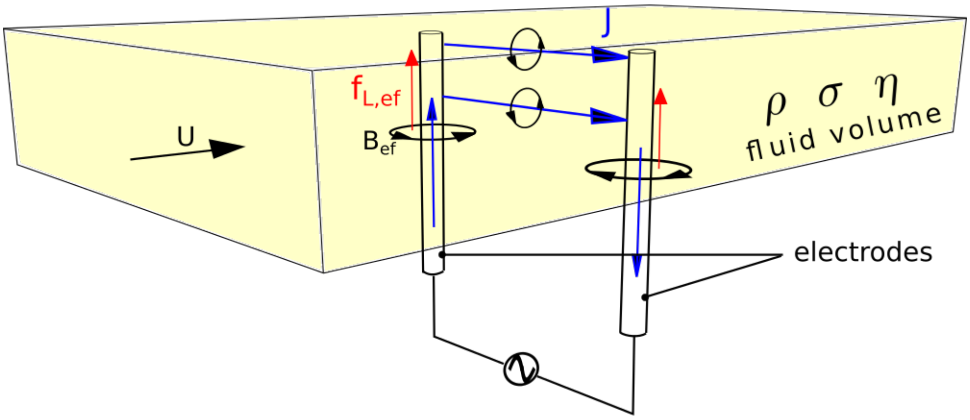

Figure III.1: Schematic of the submerged electrodes which impose a time varying electric current density $\mathbf{J}$ in the fluid. This electric current density flows in the electrodes and in the fluids, produces a magnetic field, "eigenfeld" $\mathbf{B_{ef}}$ which interacts with $\mathbf{J}$ generating a Lorentz force density $\mathbf{f_{L,ef}}$.

2.3 External magnetic flux density created by the coils

The electric potential applied on the coils creates an electric current density generating a magnetic field, which oscillates at low frequencies $(50Hz << KHz)$, described by Eq. III.2 and illustrated by the Fig. III.2. Here also the small contribution of the time varying electric field to the electric current density found in Eq. III.2 is neglected and therefore the magnetic field propagates instantaneously.

The Biot-Savart equation (Eq. III.8), which is a solution of the Eq. III.2, can be used to calculate the externally created magnetic flux density because the electric current density is considered constant over time along the coils.

$$\mathbf{B_e} = \frac{\mu_0}{4\pi} I \int \frac{d\mathbf{l} \times \mathbf{r}}{|\mathbf{r}|^3} \tag{III.8}$$

The quantity dl is a line element of the coil that contributes to the magnetic flux density at the position r measured from this element, and I correspond to the electric current in the coil.

When this magnetic flux density penetrates the fluids, its variation in time induces electric currents in the fluid σE_i but its contribution to the electric current density described by the Ohm's law (Eq. III.9) is negligible. Also, when the fluid is in motion, a further electric current density $\sigma(\mathbf{U} \times \mathbf{B_e})$ is created but the velocities $\mathbf{U}$ of the studied fluids are in the range of millimeters to centimeters per second, therefore its contribution to the total current is also neglected.

$$\mathbf{J} = \sigma(\mathbf{E} + \mathbf{E_i} + \mathbf{U} \times \mathbf{B_e}) = \sigma\mathbf{E} \tag{III.9}$$

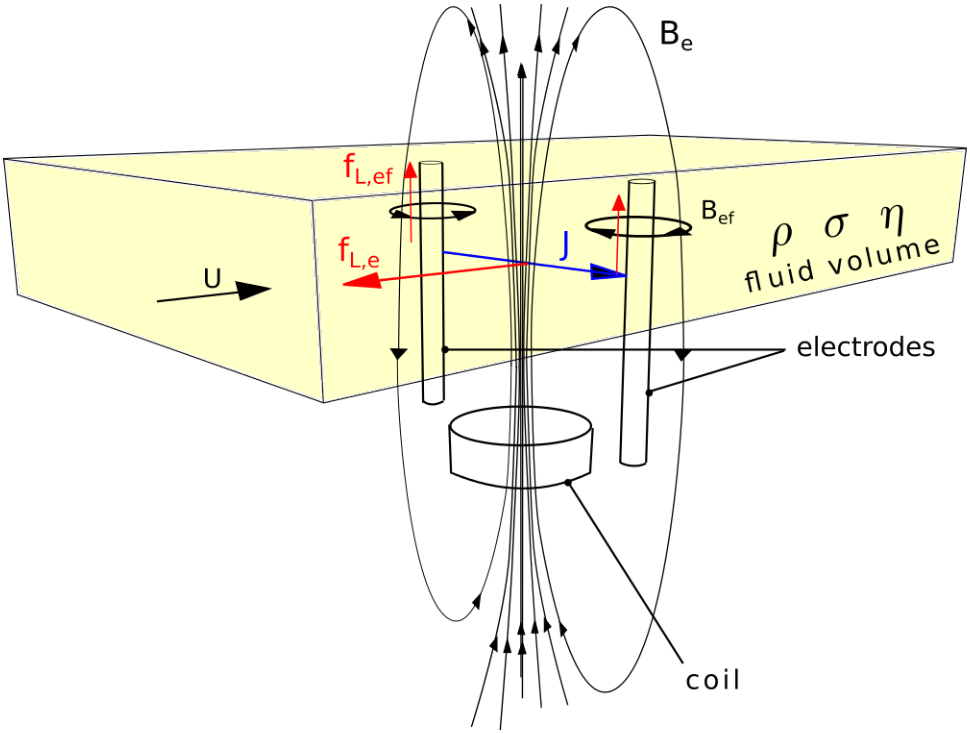

Figure III.2: Schematic of the electric current density $\mathbf{J}$ in the fluid imposed by the electrodes interacting with the external magnetic field density $\mathbf{B_e}$, created by a coil, and with the eigenfeld $\mathbf{B_{ef}}$ giving born to different directed Lorentz force densities $\mathbf{f_{L,e}}$ and $\mathbf{f_{L,ef}}$.

2.4 Lorentz force

The electric current density $\mathbf{J}$, created by the application of a electric potential differential on the electrodes, interacts with the eigenfeld $\mathbf{B_{ef}}$ carried by this current as well as with the external magnetic flux density $\mathbf{B_e}$ created by the electric current imposed on the coils. This interaction produces an electromagnetic force density (Eq. III.10), called Lorentz force density f_L (Eq. III.10), that modifies the motion of the fluid flow, illustrated in the Fig. III.2.

$$\mathbf{f_L} = \mathbf{f_{L,e}} + \mathbf{f_{L,ef}} = \mathbf{J} \times (\mathbf{B_e} + \mathbf{B_{ef}}) = \mathbf{J} \times \mathbf{B} \tag{III.10}$$

3 Governing equations

3.1 Mass transport in electrolytes under the influences of Lorentz forces

Navier-Stokes equations and constitutive relations

The mass transport of incompressible fluids under the action of pressure, friction, gravity and the Lorentz force density is described by the Navier-Stokes equations (III.11 and III.12) that are derived from the conservation of momentum or from the Newton's second law and from the conservation of mass respectively [82], [83] and [84].

$$\rho\left(\frac{\partial \mathbf{U}}{\partial t} + (\mathbf{U}\cdot\nabla)\mathbf{U}\right) = -\nabla p + \nabla \cdot \bar{\bar{\mathbf{T}}} + \rho \mathbf{g} + \mathbf{J} \times \mathbf{B} \tag{III.11}$$

$$\frac{\partial \rho}{\partial t} + \nabla \cdot \mathbf{U} = 0 \tag{III.12}$$

The variable $\mathbf{U}$ is the instantaneous velocity field distribution of the fluid, p the pressure, t the time, ρ the density of the fluid, $\mathbf{g}$ the gravitational acceleration and $\bar{\bar{\mathbf{T}}}$ the shear stress tensor.

The Eq. III.11 refers to the conservation of momentum that relates the variations of the velocity in time and space (convective acceleration) with the applied normal stresses (the pressure p) and shear stresses (the shear tensor $\bar{\bar{\mathbf{T}}}$) as well as volumetric forces like the gravitational force density $\rho\mathbf{g}$ where the amount of $\mathbf{g}$ is 9.81 m/s^2 and the Lorentz force density ($\mathbf{J} \times \mathbf{B}$). To resolve this equation, it is necessary to model the pressure and the shear tensor with constitutive relations. The first one is done by an state equation F relating the pressure, density and temperature of the fluid [83],

$$F(\rho, p, T) = 0 \tag{III.13}$$

The second by means of experimental observations that relate the shear tensor with the deformation of the fluid. This deformation moves different layers of the fluid with different velocities producing internal frictions.

Assuming small velocity gradients and linearity, the shear stress tensor takes the form [82]:

$$\bar{\bar{\mathbf{T}}} = \eta \left(\nabla\mathbf{U} + (\nabla\mathbf{U})^{T} \right) + \xi(\nabla \cdot U)I_{\delta} \tag{III.14}$$

where I_{δ} is the identity matrix and, η and ξ are coefficients that measure the resistance to the deformation, η called dynamic viscosity. The fluids that follows this rule (Eq. III.14) are called Newtonian fluids and the electrolytes analyzed in this thesis such a molten glasses and inorganic chemical solutions are considered as that.

The Eq. III.12 refers to the conservation of mass, where a variation in time of the density implies an admission or ejection of the fluid in the analyzed elementary volume, compressing or expanding it. These effects take importance when the speed of the velocity gets close to the speed of the sound in the fluid. The speed of the studied fluids are in the range of millimeters to centimeters per second which are lower than the speed of sound in these electrolytes, higher than kilometers per second.
With these assumptions, the Navier-Stokes equations (Eq III.11 and Eq. III.12) can be written in the form:

$$\rho \left(\frac{\partial \mathbf{U}}{\partial t} + (\mathbf{U} \cdot \nabla)\mathbf{U} \right) = -\nabla p + \eta \nabla^{2}\mathbf{U} + \rho\mathbf{g} + \mathbf{J} \times \mathbf{B} \tag{III.15}$$

$$\nabla \cdot \mathbf{U} = 0 \tag{III.16}$$

The pressure p, with the incompressibility assumption, becomes independent of the thermodynamic state (Eq. III.13), losing the connection with the density. In this case, the pressure is defined with the divergence of the Navier-Stokes equation (Eq. III.15) where p satisfies a Poisson's equation,

$$\nabla^{2} p = \nabla \cdot (\rho\mathbf{g} + \mathbf{J} \times \mathbf{B} - \rho(\mathbf{U} \cdot \nabla)\mathbf{U}) \tag{III.17}$$

Dimensionless parameters

The Eq. III.15 in its dimensionless form, where the dot ”$^{\cdot}$” indicates the dimensionless variables, provides three dimensionless number, the Reynolds number Re, the Froude number Fr and the ”interaction parameter” N which are written in terms of a characteristic length L of the system [89].

The Reynolds number Re defines the ratio of inertial forces $\rho U^{2} L^{2}$ to shear forces $\eta U L$ (Eq. III.19). When this number is smaller than a critical value [1], the small disturbances are dissipated and the flow remains laminar, otherwise the disturbance are amplified and the transition to turbulence occurs.

---

[1] In circular pipe flow this critical number around 2300 ± 50 was measured by Julius C. Rotta in 1956 [86],[87].

The Froude number Fr defines the ratio of inertial forces $\rho U^2 L^2$ to gravitational forces $\rho g L$ (Eq. III.20). When it is higher than 1, the formation of surface waves starts, but in this thesis the surface configuration won't be analyzed, therefore this dimensionless number is not used.

The interaction parameter N_{ip} defines the ratio of Lorentz forces JBL^3 to inertial forces $\rho U^2 L^2$ (Eq. III.21), which is related to the dimensionless number M called by [19] "the square of the modified Hartmann number".

The importance to write a differential equation, like the Navier-Stokes equation, in a dimensionless form is the ability to extract parameters such as the Reynolds number to assess the relative importance of the terms of the equation that says something about the properties of the system. In this case, if it is in laminar or turbulent regime. Also it facilitates the scale up of the physical model to a real flow conditions. The dimensionless Navier-Stokes equation is given by the Eq. III.18:

$$\left(\frac{\partial \dot{\mathbf{U}}}{\partial \dot{t}} + (\dot{\mathbf{U}} \cdot \dot{\nabla})\dot{\mathbf{U}}\right) = -\dot{\nabla}\dot{p} + \frac{1}{Re}\dot{\nabla}^2\dot{\mathbf{U}} + \frac{1}{Fr}\dot{\mathbf{g}} + N_{ip}\dot{\mathbf{J}} \times \dot{\mathbf{B}} \tag{III.18}$$

$$Re = \frac{\rho U L}{\eta} \tag{III.19}$$

$$Fr = \frac{U^2}{gL} \tag{III.20}$$

$$N_{ip} = \frac{JBL}{\rho U^2} = \frac{M}{Re} \tag{III.21}$$

The Navier-Stokes equations resolve the velocity distribution in each elementary volume of the fluid, transporting the mass contained in it. But, the equations don't resolve the velocity at the boundaries defined by the surface of the vessel that contains the fluid as well as at the interface between the fluid and the surrounding air when a side of vessel is open allowing this contact. At the surface of the vessel a non-slip condition is used where the velocity is equal to zero $\mathbf{U} = 0$ and at the interface fluid-surrounding air, a zero stress condition is used $\bar{\bar{\mathbf{T}}} = 0$.

Laminar and turbulent regime

From the three dimensionless numbers described in the previous section, the most important for this study is the Reynolds number that gives some insight about the flow, if it is in laminar regime or turbulent regime.

In laminar flows, small disturbances artificially produced, e.g. the vessel roughness, vibrations or changes in temperature, are dissipated keeping the flow steady [85], [87]. Therefore the inertial forces $(\mathbf{U} \cdot \nabla)\mathbf{U}$ can be neglected from the Navier-Stokes equation (Eq. III.15).

By contrast, when the flow gets close to the critical Reynolds number, these disturbances are amplified and the flow becomes unsteady and chaotic. Turbulent flows are very sensitive to small changes in the initial conditions, boundary conditions and physical properties of the fluids.

The variation in time and space of the velocity field in turbulent flows produces a wide range of length scales, with the large scales (comparable to the size of the vessel) influenced by the geometry of the vessel and the mean velocity field, and the small scales influenced by the kinetic energy rate received from the large scales. The successive transfer of this energy to smaller scales happen when the larger scales break up, and when it achieves the smallest scale, this energy is dissipated by the viscosity [85].

A quantification of this process was proposed by Kolmogorov [85], stating that at sufficient high Reynolds number, the velocity field of the small scales are statistically similar because they are independent of the main flow structure and geometry, therefore they could have a general form. Assuming isotropy for the small scales, the general form defined by its length l_k, time t_k and velocity u_k, called Kolmogorov scales (Eq. III.22, Eq. III.23 and Eq. III.24), is determined only by the cinematic viscosity ν and the dissipation rate ε_k (equal to the kinetic energy rate) [85].

$$l_k = \left(\frac{\nu^3}{\varepsilon_k}\right)^{1/4} \tag{III.22}$$

$$t_k = \left(\frac{\nu}{\varepsilon_k}\right)^{1/2} \tag{III.23}$$

$$u_k = (\nu\varepsilon_k)^{1/4} \tag{III.24}$$

3.2 Heat transport in electrolytes under the influences of Lorentz forces

Joule heating

The impressed electric current density about electrodes not only contributes to the production of the Lorentz force density by the interaction with the externally created magnetic field but also releases heat in the form of a volumetric heat source p_V (Eq. III.25). This heat source increases the temperature of the fluid and therefore creates temperature gradients that induces heat transport by conduction, radiation and convection connected with an additional mass transport created by the gravitational force. This process is known as Joule's heating.

$$p_V = \frac{\mathbf{J}^2}{\sigma} \tag{III.25}$$

Heat transport by convection

The transport of mass created by the gravitational force and the Lorentz force also carries heat (thermal energy), transporting it from one place to another, modifying the temperature distribution in the fluid. When the transport of mass is created only by the gravitational forces, the process is called natural convection, and it occurs when different densities exists in the fluid produced by a temperature gradient. When the transport of mass is created by other type of forces, like the Lorentz forces, the process is called forced convection [90].

This mode of heat transport depends on the velocity distribution of the fluid computed with the Navier-Stokes equations. The convective transport of the surrounding flow motion is modeled as thermal boundary condition in the form of convective heat flux q_{cv} applied on the surface of the vessel. This flux is modeled by the Newton's cooling law stating, that the heat flux is proportional to the difference between the surface temperature T_s and the surrounding air temperature T_∞ with the heat transfer coefficient α as a parameter of proportionality.

$$q_{cv} = \alpha(T_s - T_\infty) \tag{III.26}$$

Also, it is important to notice that at the surface the fluid velocity is zero and the heat transport mode in the boundary layer is only by conduction, therefore the heat transfer coefficient takes into account also the thermal conductivity of the surrounding air [90].

Heat transport by conduction

The mass in each elementary volume of the fluid contains randomly agitated atoms that transport energy via constant collisions from the more energetic (higher kinetic energy) to the low energetic state. In terms of temperature, that is proportional to the average of the kinetic energy, the heat flows from higher temperatures to lower temperatures, opposite to the direction of the temperature gradient. This mode of heat transport is called heat transport by conduction and the relation between these two quantities is obtained from experimental observation [90]. The conductive heat flux q_c is modeled by the Fourier's law that relates q_c with the temperature gradient by means of the thermal conductivity k_c of the fluid.

$$q_c = -k_c \nabla T \tag{III.27}$$

Heat transport by radiation

Also, the velocity variation of the random agitation of the atoms transports thermal energy in the form of electromagnetic waves whose wavelength depends on the temperature of the fluid. This mode of transport is called heat transport by radiation. Inside the fluid, there is constant emission, absorption and scattering of these waves but only the region close to the surface of the fluid ($\approx 1\mu m$) emits to the surroundings. The heat flux density emitted by the fluid surface is a fraction of a perfect absorber/emitter surface (blackbody radiation) that radiates in all directions (diffuse surface). The spectral intensity I_b of a black body was formulated by Planck around the year 1900 [91],

$$I_b = \frac{2hc_0^2}{n_r^2 \lambda^5 e^{\frac{hc_0}{n\lambda k_B T}} - 1} \tag{III.28}$$

where h is the Planck constant, k_B is the Boltzmann constant ($k_B = 1.38x10^{-23} m^2 Kg s^{-2} K^{-1}$), n_r is the refractive index of the surrounding which is assumed constant, λ is the wavelength and c_0 is the speed of light in vacuum. The corresponding heat flux density q_b for the black body is obtained integrating the spectral intensity over the wave length,

$$q_b = n_r^2 \sigma_s T^4 \tag{III.29}$$

$$q_r = \varepsilon \sigma_s T^4 \tag{III.30}$$

where σ_s is the Stefan-Boltzmann constant ($\sigma_s = 5.67x10^{-8} W m^{-2} K^{-4}$). The dimensionless proportionality factor between the heat flux density q_r of the fluid surface and the blackbody is called emissivity ε_r which depends on the wavelength, emission direction (specular surface) and temperature. The electromagnetic radiation can also come from the walls that enclose the surrounding air with a net radiation acting as a boundary condition.

Inside the fluid, the radiative heat flux q_r is obtained integrating the spectral intensity I_r, that is energy per unit of time, of projected surface area, and of solid angle, over the wavelength and solid angle. When this intensity crosses the fluid, the material in each elementary volume can absorb and scatter as well as emit radiation.

The radiative transfer equation [92] that describes how the intensity changes along a path through an elementary volume of the fluid at position r in the direction s is,

$$\frac{\partial I_r(\mathrm{r}, \mathrm{s})}{\partial s} + aI_r(\mathrm{r}, \mathrm{s}) + \alpha_s I_r(\mathrm{r}, \mathrm{s}) = an_r^2 \frac{\sigma_s T^4}{\pi} + \frac{\sigma_s}{4\pi} \int_0^{4\pi} I_r(\mathrm{r}, \mathrm{s}') \Phi(\mathrm{r}, \mathrm{s}') d\Omega_{as} \tag{III.31}$$

where s' is the scattering direction vector, s is the path length, a is the absorption coefficient, α_s is the scattering coefficient, Φ is the phase function that describes the angular distribution of the scattered intensity, and Ω_{as} is the solid angle. The first left term corresponds to the intensity changes along a path, the second to the loss by absorption and the third to the loss by scattering. The first term of the right corresponds to the gain by emission and the second to the gain by scattering to the s' direction.

The heat transport by radiation not always plays a significant role like in the study of chemical solution flow which happens at room temperature and the heat transport is dominated by conduction and convection.

On the other hand, the study of molten glass flow happens at high temperature ($>$ 1000 ^{o}C) where the heat transport by radiation plays a key role.

Molten glasses are semi-transparent in the infrared and visible region of the spectrum with a dependence on the wavelength of its absorption coefficient whose distribution depends on the glass composition. Nevertheless, it is not always possible to obtain this data and therefore in this study the optical properties such as emission and absorption are considered constant, independent of wavelength, direction or temperature which means that the molten glass is considered as a gray media [94].

Numerically, it is not possible to solve the radiative transfer equation (Eq. III.31) for every direction s', therefore several models have been proposed to solve the Eq. III.31 but in this study the Discrete Ordinate Method, which solves the Eq. III.31 in a define number of direction, is chosen due to its proved accuracy [94].

Heat transport equation

It is important to notice that the three mode of heat transport, convection, conduction and radiation only occur when exists a temperature gradient and therefore a non thermodynamic equilibrium state of the system. The determination of the temperature distribution T (which represents how the temperature varies with position in the medium) as function of time is obtained by solving the energy conservation equation (Eq. III.32),

$$\rho c_p \left(\frac{\partial T}{\partial t} + \mathbf{U} \cdot (\nabla T) \right) = \nabla \cdot (\bar{\bar{\mathbf{T}}}\mathbf{U}) + \nabla \cdot (k_c \nabla T) - \nabla \cdot (q_r) + \frac{(\mathbf{J})^2}{\sigma} \tag{III.32}$$

where c_p is the specific heat capacity of the fluid. The first term of the left corresponds to the rate of change of thermal energy stored by the material in an elementary volume of the fluid and the second term to the rate of convective heat flux. The first term of the right corresponds to the viscous dissipation, the second term to the net heat conduction, the third term to the net radiative heat and the last term to the volumetric heat source corresponding to the Joule heating.

Dimensionless parameters

The Eq. III.32 in its dimensionless form (Eq. III.33), where the dot ”·” indicates the dimensionless variables, provides two known dimensionless number, the Strouhal number St and the Peclet number Pe, which are written in terms of a characteristic length L, frequency f and velocity U of the system using a reference radiative heat flux density $q_{r,0}$ [90].

The Strouhal number St defines the ratio of the steady part of flow to the oscillating part of the flow. When this number is higher than 1, the oscillation motion dominates and it can be used to characterize, e.g. vortex shidding.

The Péclet number Pe defines the ratio of the rate of the heat transport by convection to the rate of the heat transport by diffusion.

Another dimensionless number is the Prandtl number Pr, that defines the ratio of the momentum diffusivity to the thermal diffusivity. When this number is higher than 1, e.g. the momentum boundary layer thickness is larger than the thermal boundary layer thickness.

$$\begin{aligned} St\frac{\partial \dot{T}}{\partial \dot{t}} + \dot{\mathbf{U}} \cdot (\dot{\nabla}\dot{T}) = \frac{\eta U}{\rho c_p L}\dot{\nabla}\left((\dot{\nabla}\dot{\mathbf{U}} + (\dot{\nabla}\dot{\mathbf{U}})^T)\dot{\mathbf{U}}\right) + \frac{1}{Pe}\dot{\nabla}\cdot(\dot{\nabla}\dot{T}) - \frac{q_{r,0}}{U\Delta T}\dot{\nabla}\cdot(\dot{q}_r) \\ + \frac{LJ^2}{U\Delta T\sigma\rho c_p}(\dot{\mathbf{J}})^2 \end{aligned} \tag{III.33}$$

$$St = \frac{Lf}{U} \tag{III.34}$$

$$Pe = \frac{UL\rho c_p}{k_c} \tag{III.35}$$

$$Pr = \frac{\eta c_p}{k_c} \tag{III.36}$$

4 Numerical methods

4.1 Lorentz force density

The electrode and coil arrangements used to generate the Lorentz force density in the fluid are energized with a single-phase alternating current. Therefore, the electric current density $\mathbf{J}$ impressed in the fluid and the externally generated magnetic flux density $\mathbf{B_e}$ oscillate both sinusoidally at the same frequency f = 50 Hz and no phase shift. The resulting Lorentz force density $\mathbf{f_{L,e}}$ always points to the same direction oscillating sinusoidally and positively. This force is separated in a steady and unsteady part where $\hat{\mathbf{J}}$ and $\hat{\mathbf{B_e}}$ correspond respectively to the steady vector of the electric current density and the externally generated magnetic field (Eq. III.37).

$$\mathbf{f_{L,e}} = \mathbf{J} \times \mathbf{B_e} = \hat{\mathbf{J}}sin(2\pi ft) \times \hat{\mathbf{B}}_\mathbf{e}sin(2\pi ft) = \frac{1}{2}\hat{\mathbf{J}} \times \hat{\mathbf{B}}_\mathbf{e} - \frac{1}{2}\hat{\mathbf{J}} \times \hat{\mathbf{B}}_\mathbf{e}(cos(4\pi ft)) \tag{III.37}$$

The typical velocities U of molten glasses, in the order of millimeters per second and inorganic solutions in the order of millimeters to centimeters per second, analyzed along this thesis, allow to neglect the oscillatory part of $\mathbf{f_{L,e}}$, because its effect is noticed in a region lower than 1 mm $\left(\frac{U}{2 \times 50\,Hz} << 1mm\right)$. Therefore, the mean Lorentz force density $f_{L,e}$ determines the flow and its magnitude is defined by the Eq. III.38,

$$f_{L,e} = JB_e sin(\theta_{JB_e}) \tag{III.38}$$

where J and B_e are the root mean square values (RMS), and θ_{JB_e} is the angle between $\mathbf{J}$ and $\mathbf{B_e}$.

Therefore, the steady part of $\mathbf{f_{L,e}}$ is used to control the fluid flow reducing the simulation complexity because it doesn't need to be made in transient mode to take into account the effects of the unsteady part of $\mathbf{f_{L,e}}$.

The electric current density $\mathbf{J}$ is computed using the User Defined Scalar (UDS) transport Equations of the solver Fluent that is loaded dynamically by means of the User Defined Function (UDF). The UDS computes the Laplace equation of the electric potential $\nabla^2\varphi$ and then $\mathbf{J}$ is computed with the Eq. III.5.

The externally created magnetic flux density $\mathbf{B_e}$ is computed with the Eq. III.8 implemented in a UDF. The Eigenfeld $\mathbf{B_{ef}}$ (see section 2.2) is computed using the vector potential approach (Eq. III.6). Therefore, for each component of the vector potential $\mathbf{A_{ef}}$ a UDS is defined in a UDF, which computes directly the Eq. III.6. Then the Eigenfeld is calculated with the Eq.III.7 in a UDF.

Finally, the computation of $\mathbf{f_{L,e}}$ and $\mathbf{f_{L,ef}}$ is made also in a UDF and loaded dynamically by the Fluent solver.

4.2 Mathematical model

The mathematical model is composed of the Navier-Stokes equations (Eq. III.11 and III.12), including the Lorentz force density, and the heat transport equation (Eq. III.32), including the Joule heating.

This set of equations are discretized with the finite volume method, which are implemented in the solvers used along this thesis such as Ansys/Fluent [2] and OpenFOAM [3].

For this purpose, the geometry is divided into discrete control volumes Ω (cells) where the equations are integrated, with some terms transformed into surface integrals, where $\mathbf{S}$ is a surface vector, using the divergence theorem.

$$\rho\left(\int\frac{\partial\mathbf{U}}{\partial t}d\Omega+\int\mathbf{U}\cdot\mathbf{U}d\mathbf{S}\right)=-\int p d\mathbf{S}+\eta\int(\nabla\mathbf{U}+(\nabla\mathbf{U})^T)d\mathbf{S}+\int\mathbf{J}\times\mathbf{B}d\Omega \tag{III.39}$$

$$\int\mathbf{U}d\mathbf{S}=0 \tag{III.40}$$

In turbulent regime, the flow is irregular and its quantities, such as velocity and pressure, change randomly in time and space in a a wide range of scales.

The whole range of scales (larger than the Kolmogorov scales Eq. III.22 and Eq. III.23) is calculated with a Direct Navier-Stokes Simulation (DNS), which solves the Navier-Stokes equations to determine the instantaneous velocity field $\mathbf{U}$, but it needs a mesh density and time step that make the simulation unpractical with today computational resources.

The DNS needs a number of total mesh points $N_d \approx Re^{9/4}$ [88] therefore, an statistical approach is used to analyze the flow.

Reynolds averaging approach (RANS)

In a Reynolds averaging approach, the instantaneous quantities are decomposed in a mean or time averaged ($^-$) and fluctuating parts ($'$),

$$\mathbf{U} = \bar{\mathbf{U}} + \mathbf{u}', \qquad p = \bar{p} + p' \tag{III.41}$$

where $\mathbf{U}$ is the instantaneous velocity vector field and p is the instantaneous pressure field. Replacing these quantities by their decomposed counterpart in the Navier-Stokes equations, and applying the mean operator ($^-$), the Reynolds Average Navier-Stokes equations (RANS) is obtained,

$$\begin{aligned}\rho\left(\int \frac{\partial \bar{\mathbf{U}}}{\partial t} d\Omega + \int \bar{\mathbf{U}}(\bar{\mathbf{U}})^T d\mathbf{S}\right) = -\int \bar{p} d\mathbf{S} + \eta \int (\nabla \bar{\mathbf{U}} + (\nabla \bar{\mathbf{U}})^T) d\mathbf{S} + \int \mathbf{J} \times \mathbf{B} d\Omega \\ -\rho \int \overline{\mathbf{u}'(\mathbf{u}')^T} d\mathbf{S}\end{aligned} \tag{III.42}$$

$$\int \bar{\mathbf{U}} d\mathbf{S} = 0 \tag{III.43}$$

The Reynolds stress tensor $\rho\overline{\mathbf{u}'(\mathbf{u}')^T}$ includes all turbulent scales and has to be modeled in order to close the Eq. III.42. One method is the Boussinesq hypothesis (Eq. III.44), which relates this tensor with the gradient of the mean velocity by means of the turbulent viscosity η_t, assuming it as an scalar isotropic quantity.

$$\rho\overline{\mathbf{u}'(\mathbf{u}')^T} = -\eta_t(\nabla \bar{\mathbf{U}} + (\nabla \bar{\mathbf{U}})^T) + \frac{2}{3}\rho k I_\delta = -2\eta_t \bar{\bar{\bar{S}}} + \frac{2}{3}\rho k I_\delta \tag{III.44}$$

Here, I_δ is the identity matrix and the last term is included because the trace of the Reynolds stress tensor is the turbulent kinetic energy k.

This assumption is not always valid because the larger scales are affected by the shape of the geometry, unlike the smaller scales that are less sensitive to the geometry and therefore more isotropic.

Currently, there are several RANS turbulence models based on the Boussinesq hypothesis to resolve the turbulent viscosity [126], but the turbulence models used along this thesis are those offered by the solver Fluent, based on two transport equations that can resolve rotating flow [2].

These are the Renormalization group (RNG) $k-\varepsilon$ model, the Realizable $k-\varepsilon$ model and the Shear-stress transport (SST) $k-\omega$ model.

The RNG and Realizable $k-\varepsilon$ models are an improvement of the standard k- ε model, which assumes that the flow is fully turbulent (high Reynolds number model) needing a damping function close to the walls where the viscous effects are more important. The RNG $k-\varepsilon$ model accounts for low-Reynolds-number effects or viscous forces enhancing the accuracy for swirling or rotating flows. The Realizable k- ε model includes terms to better predict rotating flows, boundary layers under strong adverse pressure gradients, separation, and recirculation [2]. Also, from [2], the last model gives the best performance for complex secondary flow.

The SST $k-\omega$ model blends the standard $k-\omega$ model in the near wall region with the standard $k-\varepsilon$ model in the far field. These equations have been written in terms of the $k-\omega$ model introducing a cross diffusion term C_ω and blending functions F_ω. Therefore, it takes the advantage of the low Reynolds formulation of $k-\omega$ model, which predicts the effects of adverse pressure gradient in the boundary layer and the experimental parameter of the law of the wall (see section 4.3). And of the high Reynolds formulation of the $k-\varepsilon$ model for the free shear flow [2].

All these turbulence models are based on the kinetic energy of the turbulent fluctuations per unit of mass k, often called turbulent kinetic energy. It is defined by the trace of the Reynolds stress tensor and thus, its transport equation is obtained from the Eq. III.42.

The dissipation rate per unit of mass ε or simply called as the dissipation rate of the standard k- ε model is computed with an empirical transport equation with its closure coefficients defined by experimental data. The transport equation for ε in the RNG k- ε model is modified with additional term, using other closure coefficients. The Realizable $k-\varepsilon$ model uses other closure coefficients and redefines the transport equation for ε.

The dissipation per unit turbulence kinetic energy or specific dissipation rate ω is obtained also from an empirical transport equation.

From a dimensional analysis, the η_t is proportional to a combination of k and ε or ω. The $k-\varepsilon$ models compute the turbulent viscosity η_t as,

$$\eta_t = \rho C_\mu \frac{k^2}{\varepsilon} \tag{III.45}$$

with $C_\mu = 0.0845$ in the standard $k-\varepsilon$ model, $C_\mu = 0.09$ in the RNG $k-\varepsilon$ model, but C_μ is a function in the Realizable $k-\varepsilon$ model.

The SST $k-\omega$ model computes the turbulent viscosity η_t as,

$$\eta_t = \frac{\rho k}{\omega} \times max[\alpha^*, F^*] \tag{III.46}$$

where α^* is coefficient that reduces η_t (correction for low Reynolds number), and F^* is a function proportional to the blending functions of the SST k- ω model (see [2]).

The SST $k-\omega$ model is elected for the analysis of the flow after a validation with a Large Eddy Simulation (LES) and also because it has a more robust implementation (see section 4.3). Therefore, only the transport equations of this model are presented.

The transport equation for k has the form,

$$\rho\left(\frac{\partial k}{\partial t} + \nabla \cdot (\mathbf{U}k)\right) = \nabla\left(\left(\eta + \frac{\eta_t}{\sigma_k}\right)\nabla k\right) + f_{cc}P_k - D_k \tag{III.47}$$

where $P_k = min(\eta_t \bar{\bar{S}}^2, 10\rho\beta k\omega)$ is the production of k and $D_k = \rho\beta^* k\omega$ is the dissipation of k.

The transport equation for ω has the form,

$$\rho\left(\frac{\partial \omega}{\partial t} + \nabla \cdot (\mathbf{U}\omega)\right) = \nabla\left(\left(\eta + \frac{\eta_t}{\sigma_\omega}\right)\nabla \omega\right) + f_{cc}P_\omega - D_\omega + C_\omega \tag{III.48}$$

where $P_\omega = P_k\rho/\gamma$ is the production of ω, $D_\omega = \rho\beta k\omega^2$ is the dissipation of ω and C_ω is the cross diffusion term.

The closure coefficients γ, β, β^*, σ_k and σ_ω of the transport equations, Eq. III.47 and Eq. III.48, depend on the blending functions of this model (see [2]).

The disadvantage to model all the turbulent scales is that, the larger scales are insensitive to the surface curvature of the geometry, which can suppress or amplify turbulence [136, 137] whether it is convex or concave curvature respectively. Therefore a curvature correction f_{cc} is necessary to introduce in the transport equation of k, ε and ω modifying their production terms.

In the RNG $k-\varepsilon$ and Realizable $k-\varepsilon$ models, the curvature correction could produce unexpected results because these models have already their own terms to take into account rotating flow.

Large Eddy Simulation (LES)

In the large eddy simulation (LES) approach, the larger scales of the turbulence, which are in the same order of the dimension of the geometry, are computed with the Navier-Stokes equations while the smaller scales are modeled. Therefore, it is expected that LES is more accurate than the RANS turbulence models for flows in which large scales are important.

The larger scales are affected by the boundary conditions and the shape of the geometry, contributing the most to the Reynolds stresses while the smaller scales contributes less to the Reynolds stresses and thus are less critical. The smaller scales can be considered statistically isotropic with nearly universal characteristics and thus, it is more likely to find a universal turbulence model for them.

The advantage of this approach is that, the smallest cell can be much larger than the Kolmogorov length (Eq. III.22), therefore it needs less cells than a DNS as well as larger time step, which reduce the computational cost. But anyway, it needs finer mesh and shorter time step than RANS as well as enough computation time to obtain stable statistics of the flow.

The instantaneous velocity vector field $\mathbf{U}$ is decomposed into a filtered or resolved time dependent component $\widetilde{\mathbf{U}}$ that contains the large scales and a residual or subgrid-scale (SGS) by means of a filtering operation.

The filtering operation is defined by,

$$\widetilde{\mathbf{U}} = \int G\mathbf{U}d\Omega \tag{III.49}$$

where G is the filter function that determines the resolved scale and $d\Omega$ an infinitely volume of the geometry. The residual velocity is defined by,

$$\mathbf{u}' = \mathbf{U} - \widetilde{\mathbf{U}} \tag{III.50}$$

The instantaneous velocity field $\mathbf{U}$ is replaced by the Eq. III.50 in the Navier-Stokes equations,

$$\begin{aligned}\rho\left(\int \frac{\partial \widetilde{\mathbf{U}}}{\partial t} d\Omega + \int \widetilde{\mathbf{U}}(\widetilde{\mathbf{U}})^T d\mathbf{S}\right) = -\int \widetilde{p} d\mathbf{S} + \eta \int (\nabla\widetilde{\mathbf{U}} + (\nabla\widetilde{\mathbf{U}})^T) d\mathbf{S} + \int \mathbf{J}\times\mathbf{B}d\Omega \\ -\rho\int \mathbf{U}\widetilde{(\mathbf{U})}^T + \rho\int \widetilde{\mathbf{U}}(\widetilde{\mathbf{U}})^T d\mathbf{S}\end{aligned} \tag{III.51}$$

$$\int \widetilde{\mathbf{U}} d\mathbf{S} = 0 \tag{III.52}$$

with the last two terms of the Eq. III.51, being the residual stress tensor or the SGS stress tensor $\rho\mathbf{U}\widetilde{(\mathbf{U})}^T - \rho\widetilde{\mathbf{U}}(\widetilde{\mathbf{U}})^T$. This tensor is modeled in the solver Fluent with the Boussinesq hypothesis (Eq. III.53) as in the RANS models (Eq. III.42), where the turbulent viscosity becomes the SGS turbulent viscosity η_{sgs}.

The solver Fluent offers four models to compute the η_{sgs}. The Smagorinsky-Lilly model, the dynamic Smagorinsky-Lilly model, the Wall-Adapting Local Eddy-Viscosity (WALE) model, and the dynamic kinetic energy subgrid-scale model.

Different to the RANS turbulence models, the turbulent kinetic energy k is not included into the Bussinesq hypotesis but into the filtered pressure $\widetilde{p}$. Therefore, the isotropic part, the trace, of the sub grid stresses are not modeled.

$$\rho\mathbf{U}\widetilde{(\mathbf{U})}^T - \rho\widetilde{\mathbf{U}}(\widetilde{\mathbf{U}})^T = -\eta_{sgs}(\nabla\widetilde{\mathbf{U}} + (\nabla\widetilde{\mathbf{U}})^T) = -2\eta_{sgs}\bar{\bar{S}}_{sgs} \tag{III.53}$$

The turbulent viscosity η_{sgs} is computed by the Smagorinsky-Lilly model with the relation,

$$\eta_{sgs} = \rho L_{sgs}^2\sqrt{2\bar{\bar{\mathbf{S}}}_{\mathbf{sgs}}\bar{\bar{\mathbf{S}}}_{\mathbf{sgs}}} \tag{III.54}$$

where $L_{sgs} = min\left(\kappa d_w, C_s\Omega^{1/3}\right)$, with d_w the distance to the closest wall, κ the von Kármán constant and $C_s = 0.17$ the Smagorinsky constant, but the solver Fluent uses $C_s = 0.1$ because it gives better results in a wide range of flows.

The Dynamic Smagorinsky-Lilly Model computes dynamically C_s varying in time and space based on the resolved scales.

In the WALE model, the relation for η_{sgs} is reformulated (see [2]). The dynamic subgrid-scale kinetic energy model includes the subgrid-scale kinetic energy k_{sgs} (Eq. III.55), computed with a transport equation,

$$\eta_{sgs} = C_k k_{sgs}^{1/2}\Omega^{1/3} \tag{III.55}$$

where C_k is determined dynamically.

4.3 Boundary layer

Near the walls of the geometry, the mean velocity vectors are nearly parallel to the surface of the wall decreasing until a value of zero at the wall surface (non slip condition). The momentum boundary layer thickness is the distance from the wall to the position where the mean velocity is equal to 99% of the free stream velocity [85].

In turbulent flows, the mean velocity vectors vary logarithmically in relation with the distance y_s from the surface. This behavior was validated with measurements [126] and it is called the law of the wall.

Near the wall surface, the Reynolds stress tensor is close to zero and the wall shear stresses τ_w is manly due to viscous effects. From that is defined a friction velocity u_τ and a length scale δ_τ.

$$u_\tau = \sqrt{\frac{\tau_w}{\rho}}, \qquad \delta_\tau = \frac{\eta}{\rho u_\tau} \tag{III.56}$$

as well as a dimensionless distance from the surface y^+,

$$y^+ = \frac{y_s}{\delta_\tau} = \frac{u_\tau y_s \rho}{\eta} \tag{III.57}$$

This y^+ is used to define three regions within the boundary layer. The viscous sublayer ($y^+ < 5$) where viscous forces are more important, the buffer layer ($5 < y^+ < 30$) where both inertial and viscous forces are important and the logarithmic layer ($30 < y^+ < 300$) where inertial forces are more important [85, 2].

In the viscous sublayer, the dimensionless velocity u^+ has a linear behavior respect to y^+ ($u^+ = y^+$), but in the logarithm layer, it has a logarithm behavior (logarithm law of the wall),

$$u^+ = \frac{U}{u_\tau} = \frac{1}{\kappa} lny^+ + C_{lw} \tag{III.58}$$

In the buffer layer, u^+ has not a define behavior.

From DNS computation and measurements, the constant $C_{lw} \approx 5$ and the von Kármán constant $\kappa \approx 0.41$, which is also obtained from an analytical analysis [85].

This constant C_{lw} is predicted successfully by the SST $k-\omega$ model without modification of its closure coefficients but not by the $k-\varepsilon$ models [126].

The k- ε models and the LES model were validated for free shear stress flow. Therefore, a special consideration needs to be given near the wall. In the other hand, the $k-\omega$ model was designed to be applied throughout the boundary layer.

There are two methods to resolve the flow near the wall. One method is to model the viscous sublayer and the buffer layer with wall functions to bridge these regions with the turbulent region (logarithmic layer). Therefore, it is not necessary to modify the turbulence models (closure coefficients) near the walls. The second method modifies the turbulence models to resolve the complete boundary layer.

When the mesh is enough coarse, and the centroid of the computational cell adjacent to the wall is in the logarithmic or buffer layer, the law of the wall is used by the solver Fluent (wall functions), otherwise when the centroid of the computational cell is in the viscous sublayer, the relation $u^+ = y^+$ is used. When it is in the buffer layer, the values of the logarithmic layer and viscous sublayer are blended.

The turbulent kinetic energy k of the RANS models is solved in the whole domain with a boundary condition at the wall,

$$\frac{\partial k}{\partial n_w} = 0 \tag{III.59}$$

where n_w is a unitary vector normal to the wall.

The dissipation rate ε, the specific dissipation rate ω as well as the production P_k are not solved near the wall, instead they are computed with relations defined in [2].

The thermal boundary layer is divided in a thermal conduction layer (linear law) and a convection layer (logarithmic law) where the thermal transport by the turbulence is important. Also here, there are two methods to resolve the thermal boundary layer, one is using wall functions and the other is resolving the temperature profile up to the wall.

Discretization

The solver Fluent offers several discretization methods to interpolate the velocity $\mathbf{U}$ and pressure p from the cell center to the faces of the cell, which is used to resolve the equations of the mathematical model (see section 4.2).

The velocity interpolation is made by an upwind schema (relative to the direction of the normal velocity), which uses a Taylor series expansion around the cell center value. For a first order, the face value $\mathbf{U_f}$ is equal to the cell center value $\mathbf{U_c}$, and for a second order, it includes a first derivate for the velocity, giving more accuracy, where d_{cf} is the distance between the center and the face.

$$\mathbf{U_f} = \mathbf{U_c} + d_{cf}\nabla\mathbf{U_c} \tag{III.60}$$

The velocity gradient of the Eq. III.60 as well as the different velocity gradients found in the mathematical model are computed with the least-squared cell-based method which assumes a linear variation between cells. In LES a second order bounded central differencing scheme is used.

The standard method for the pressure interpolation imposes a zero normal pressure gradient on the walls that is not true in presence of curvatures. For that reason, a second order interpolation (based on central differences) is used.

The time derivative, is discretized with a first order accuracy,

$$\frac{\partial \mathbf{U}}{\partial t} = \frac{\mathbf{U}^{n+1} - \mathbf{U}^{n}}{\Delta t} \tag{III.61}$$

where n is the current time level.

The equations of the mathematical model are resolved in an iterative way with the Semi-Implicit Method for Pressure Linked Equations (SIMPLE), which uses an starting guess pressure, and then the velocity is corrected with a pressure-correction equation to satisfy the continuity (Eq. III.40).

5 Homogenization of electrolytes

The process of the Lorentz force generation in the fluid described by the Maxwell's equations as well as how it modify the fluid flow, described by the Navier-Stokes equations, and the temperature distribution, described by the heat transport equation are presented in the previous sections.

The mathematical model is used to analyze the possibilities to modify the flow in a beneficial way by means of the Lorentz force such as for the mixing of the fluid until obtaining a high homogenization degree.

The characterization of the mixing process is done using the trajectories of a group of passive particles that follow the fluid flow and the quality of the resulting homogenization is quantified by several parameters such a the stirring index, the local stretch ratio, the lambda Alfons and the residence time presented in the next section. But along this thesis, only the stirring index is used.

5.1 Ideal Homogenization

An ideal homogenization happens when a physical magnitude is spread uniformly through the whole volume of the system. This uniform distribution has the property of self-similarity, based in fractal geometries, remaining the same at different scales (reduced copy of the whole). The uniformity is obtained bringing initially distant parts close together and separating initially close parts. That produces an exponential divergences or convergences of the distance $l(t)$ between the particles over time (Eq. III.62), and therefore their trajectories (physical magnitude) [95].

$$l(t) = l(0) \times exp(\lambda_L t) \tag{III.62}$$

This exponential increase of the distance between two close trajectories $l(t)$ is measured with the Lyapunov exponent λ_L which is the slope of the linearized Eq. III.62 (Eq. III.63), applying the logarithmic function on both sides.

$$ln\left[\frac{l(t)}{l(0)}\right] = \lambda_L t \tag{III.63}$$

This exponential separation produces a chaotic pattern for the particles distribution which has the property of self-similarity as fractal geometries. Therefore, it is possible to calculate its fractal dimension using the box counting method. The region is covered with a regular grid of size r_{box} and then counting the number of grid boxes $K(r_{box})$ which contains at least one particle. Both quantities are related with the Eq.(III.64) when $r_{box} \to 0$.

$$K(r_{box}) = \left(\frac{1}{r_{box}}\right)^{D_{box}} \tag{III.64}$$

Applying the logarithm to the Eq.(III.64), it becomes,

$$ln[K(r_{box})] = D_{box} \times ln\left[\frac{1}{r_{box}}\right] = -D_{box} \times ln[r_{box}] \tag{III.65}$$

where D_{box} is the slope of the Eq.(III.65) and represents the box counting fractal dimension. A geometry is said fractal when the box counting fractal dimension is a non-integer value.

In a fluid, the intrinsic mechanism to bringing initially distant parts close together and separating initially close parts in a fluid is by means of stretching and folding. These can be described with the Baker map model where a slice of the fluid with two defined unmixed regions is stretching and then folding sequentially. Then, repeating this process several times, two points initially together suffer an exponential divergence, Fig. III.3.

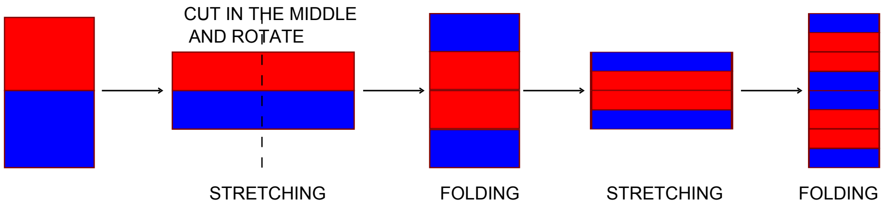

Figure III.3: The blue and red color represent two unmixed regions which are stretching and folding several times producing a chaotic mixing.

From these considerations, the mixing process made by the Lorentz force must stretch and fold the fluid several times until achieving a good homogenization quality [98] and [99] quantified by mixing parameters.

5.2 Mixing parameters

The analysis of the mixing grade (homogenization quality) produced by the Lorenz forces is made using the trajectories of a group of passive particles (the physical magnitude) that follow the streamlines of the fluid. The quantification of the mixing grade can be characterized by different mixing parameters found in the literature [99], [97] and [101] such as:

- Local stretch ratio
- Stirring index
- Lambda Alfons
- Residence time distribution

The Local Stretch Ratio (s_{ST})

The local stretch ratio is the ratio between the total distance $d(t)$ at the time t and the total distance $d(t_0)$ at the initial time t_0 of N particles. It is computed taking the sum of the distance r_i between two consecutive particles,

$$d(t) = \sum_{i=1}^{N-1} |r_{i+1}(t) - r_i(t)| \tag{III.66}$$

then divided by the initial distance $d(t_0)$, and applying on it the natural logarithmic,

$$s_{ST}(t) = ln \left[\frac{d(t)}{d(t_0)} \right] \tag{III.67}$$

From the description of an ideal homogenization, the exponential divergence characterized by the Lyapunov exponents, Eq.(III.63), is compared with the slope λ_s of the local stretch ratio s (Eq. III.67). More the result grows monotonically more the divergence has an exponential behavior and the particle distribution approaches the chaotic pattern [99].

The Stirring Index (ε_{SI})

The stirring index measures the particle distribution respect to an ideal homogenization. It is calculated using a fixed number K of boxes which covers a plane of the volume or the volume itself covered by cubes.

$$\varepsilon_{SI} = \frac{1}{K} \sum_{i=1}^{K} \omega_i \tag{III.68}$$

$$\omega_i = \frac{n_i}{m} \qquad n_i < m \tag{III.69}$$

$$\omega_i = 1 \qquad n_i \geq m \tag{III.70}$$

Here, n_i is the number of particles in the box i and m the number of particles per box for an uniform distribution, defined as $m = N/K$. A stirring index equal to one means that the number of particles in each box is the same and the distribution is ideal for the given K [101].

The Lambda Alfons (λ_{Alfons})

The Lambda Alfons measures the total stretching of each trajectory $p_i(t)$. It is calculated taking the strain matrix for each point j,

$$\frac{1}{2}\left(\nabla v_i^j + (\nabla v_i^j)^T\right) \tag{III.71}$$

defined with the velocity v_i^j at the point j for the trajectory i. To obtain the principal strain directions, a suitable coordinate transformation has to be applied to the Eq.(III.71) to transform it to a diagonal matrix. The eigenvalues λ_i^j of this diagonal matrix are the values of the principal strains.

The maximum eigenvalue $\lambda_{max,i}^j$ for each point j is selected and integrated over each trajectory $p_i(t)$. Finally, the Lambda Alfons $\lambda_{Alfons,i}$ for each trajectory is computed applying the natural logarithm to this integral [97].

$$\lambda_{Alfons,i} = ln\left[\int_{t_i}^{t_f} \lambda_{max,i}(t)|\vec{v}_i|dt\right] \tag{III.72}$$

The idea behind is that the strain matrix is related to the viscous dissipation, which can be related to the energy dissipated in the stretching of the fluid [99].

The Residence Time Distribution RTD

The time that the particles needs to travel from the injection position to the outlet in continuous mode of the vessel or until the process is finished in a batch mode of the vessel is called the residence time t_{RTD}. The residence time of each particle is not the same, forming a residence time distribution $f_{RTD}(t)$ (RTD). The RTD is a discrete probability distribution function with its cumulative distribution function $F_{RTD}(t)$ defined by the minimum residence time MRT, the mean residence time $\bar{t}_{RTD}$ (see Eq. III.73) and the width of the distribution measured by the standard deviation σ_{RTD} [76, 103] (see Eq. III.74).

$$\bar{t}_{RTD} = \frac{V}{\dot{m}} \tag{III.73}$$

$$\sigma_{RTD} = \frac{1}{N}\sqrt{\sum_{i=1}^{N}(t_{RTD,i} - \bar{t}_{RTD})^2 f_{RTD,i}} \tag{III.74}$$

where V is the volume of the vessel, $\dot{m}$ is the mass flow trough the vessel and N the total particle number. In an ideal case $\sigma_{RTD} = 0$.

In the case of an ideal homogenization, the exponential divergence grows up over time (see Eq. III.63 and Fig. III.3), then, more time the particles stay in the vessel, better the homogenization will be. Assuming that the Lorentz force stretches and folds the fluid in a proper way, the residence time could be used as indirect measure of the homogenization quality.

5.3 Laminar homogenization processes

In laminar flows characterized by a low Reynolds number such as molten glass flow, the small disturbances are dissipated resulting in a steady flow. That property allows the flow to follow a path designed by an external force such as the Lorentz force that when its magnitude is enough high to break the inertia of the fluid ($f_L > \rho U^2 L^2$), it can be used to stretch and fold the fluid and thus to set the conditions for the mixing process. Therefore, the quality of the homogenization depends on the geometry of the vessel as well as on the Lorentz force distribution.

Without the use of this external force, the homogenization would be determined only by the diffusion. The very low value of the diffusion coefficient of molten glasses $\approx 10^{-8}$ makes that this process takes a long time [102].

5.4 Turbulent homogenization processes

In turbulent flows characterized by a high Reynolds number such as the flow of chemical solutions, the small disturbances are amplified resulting in a unsteady and chaotic flow. In this case, the stretching and folding of the fluid cannot be controlled by an external force such as the Lorentz force because it won't follow strictly the path defined by it.

However, turbulent flows transport and mix the fluid much more effectively than a comparable laminar flow due to the wide range of scales, therefore this characteristic can be used to start the mixing process in chemical solutions [85].

First of all, the chemical solution flow is driven to the turbulent regime by the Lorentz force. Then the variation in time and space of the velocity field that produces a wide range of length scales will be the responsible to stretch and fold the fluid and thus to start the mixing process.

As in the previous case, the homogenization quality depends on the geometry of the vessel as well as on the distribution of the Lorentz force in the volume.

CHAPTER IV

Project I: Electromagnetic mixer

1 Introduction

This project is focused on the study of a new technique, the Lorentz force technique, replacing the mechanical stirrer used currently in the glass industry e.g. for the production of optical glass, requiring a high degree of homogenization (See chapter I section 3.4).

The first part of the study is focused on the design, construction and description of the physical model for the homogenization of the molten glass. Following by a numerical analysis of the physical model that explores the mixing capabilities of the electromagnetic mixer, initially developed in a previous work made by Sugilal Gopalakrisnan [19] as an extension of the Aref's blinking vortex model. The physical model uses a fluid model in order to work at room temperature, 25 °C - 35 °C, decreasing the complexity of the experimental study so that the influence of the heat transport on the mass transport can be neglected.

The potential of this new mixing technique is showed by means of the stirring index (Eq. III.68), a parameter that quantifies the homogenization quality using the spatial distribution of passive particles. The stirring index of the electromagnetic mixer is compared with the stirring index of a highly optimized mechanical stirrer provided by SCHOTT AG Mainz [1] . Due to the laminar regime of the fluid, these particles flow vertically in the outlet channel, therefore the stirring index is computed in a cross section plane of it.

The second part of the study is the experimental validation of the numerical results regarding the calculated stirring indices. The stirring index is determined experimentally using a camera-laser system that records the position (x_i , y_i, z_i) of nearly inertia-free, micrometer-sized silicon nitride particles (Si_3N_4) introduced in the input of the physical model and a self-developed image processing technique.

In the third part of the study, the results of the experimental model are scaled up with the validated model to a real mixer of soda-lime glass. For that, it is necessary to introduce the heat transport in the model as well as the dependencies of the physical properties on the temperature, together with realistic mass flow and wall temperature of the mixer.

2 Description of the physical model

2.1 Derivation of the main parameter

The design of the physical model is based on a real stirring cell provided by SCHOTT AG (Fig. IV.1) which is needed in the production of optical glass. Here, a low variation of the refractive index $< \pm 0.0005$ for the standard quality of fine annealed glasses is necessary according to ISO 12123 [114].

The physical properties of the molten glass, homogenized in the stirring cell, are density ρ_{AG} of 2350 Kg/m^3 and viscosity η_{AG} of 27 Pas. Molten glass flows with a rate of 1440 Kg/d within the real stirring cell having a diameter D_{AG} of 240 mm and a length L_{AG} of 360 mm giving a mean axial velocity $U_{AG,z}$ of 0.157 mm/s. The mechanical stirrer rotates with a speed of 30 min^{-1}.

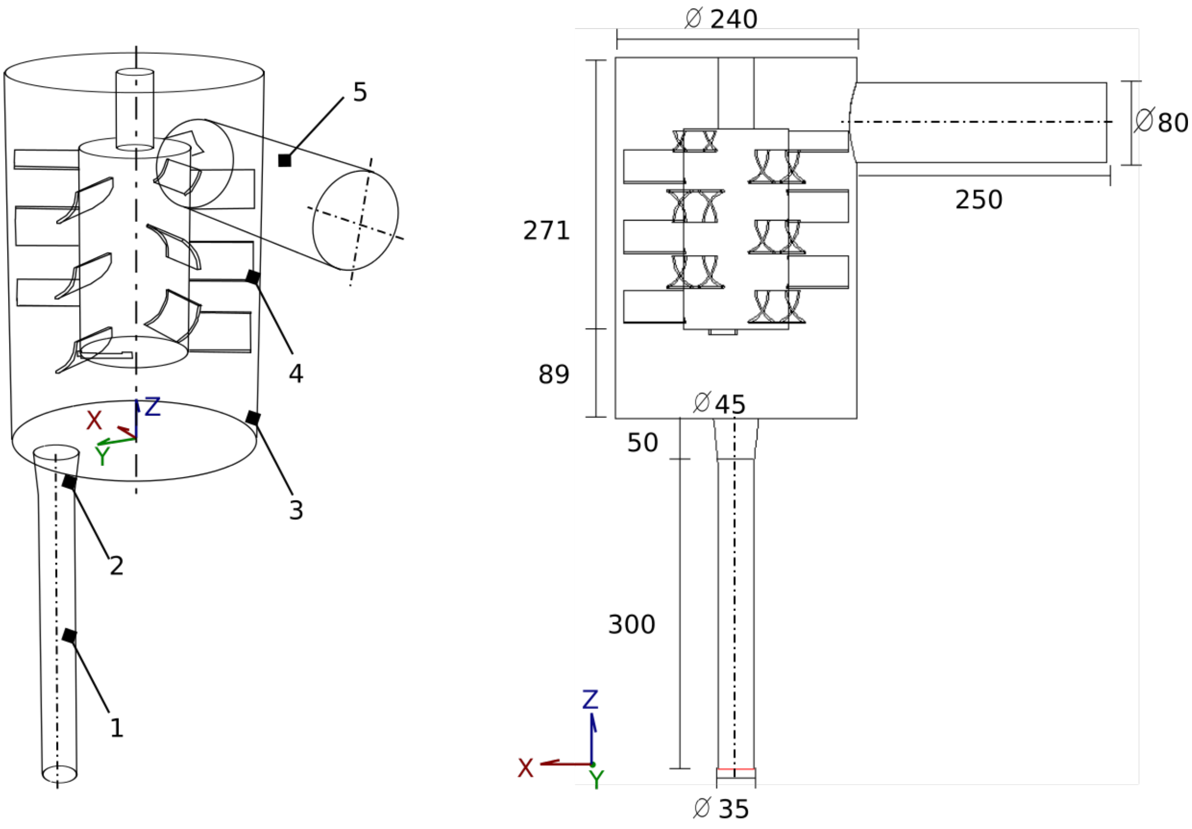

a) b)

Figure IV.1: Schematic of the real stirring cell. a) Perspective view. 1- outlet channel, 2- conical joint, 3- outside wall, 4- mechanical stirrer, 5- inlet channel. b) Side view with the geometrical data in mm.

With these values it is possible to scale down the real stirring cell, yet keeping constant its Reynolds number Re_{AG} (Eq. IV.1) and obtaining the same mass transport behavior in the physical model (Re_{PM}).

$$Re_{AG} = \frac{\rho_{AG} U_{AG,z} D_{AG}}{\eta_{AG}} = 0.003 = Re_{PM} = \frac{\rho_{FM} U_{FM,z} D_{PM}}{\eta_{FM}} \tag{IV.1}$$

The physical model of the electromagnetic mixer (Fig. IV.2) is composed of a double wall cylindrical container made of Plexiglas (PMMA- Polymethyl methacrylate) in which is located one outer electrode and two inner electrodes made of stainless steel (1.4301). The outer electrode and one of the inner electrode are always connected to an AC voltage with a frequency of 50 Hz, at the same time the electric activation of both inner electrodes alternates in a constant time interval (Fig. IV.4). The electromagnetic mixer also consists of ten coils made of copper wire [106] surrounding the mixer positioned along its axis (Fig. IV.2.b). The electric current applied on the coils has the same frequency as the voltage applied on the electrodes without phase shifting, producing a magnetic field parallel to the axis of the mixer (Fig. IV.6.a). For a detail description of the construction and the design of the physical model see [105].

The relation between the magnetic flux density, the geometrical data and the electric potential applied on the electrodes is based on a parametric study performed at the TU Ilmenau [19].

2.2 Physical properties of the fluid model

The molten glass is replaced by a fluid model. The fluid model is made of glycerin (99,5 %, Stockmeier Chemie GmbH & Co. KG), deionized water and sulfuric acid (95 – 98 %, Merck KGaA) in composition of 80 wt-% glycerin, 10 wt-% H_2O and 10 wt-% H_2SO_4 respectively.

The physical properties of this fluid at room temperature (25°C) are density ρ_{FM} of 1285 Kg/m^3, dynamic viscosity η_{FM} of 0.2 Pas, and electrical conductivity σ_{FM} of 0.49 S/m (see [104], [105]). To avoid the redox reactions of the water (water electrolysis), it is necessary to impose a limitation on the electric potential difference applied between the electrodes equal to the standard potential of the water electrolysis of 1.229 V at 25°C [107].

Table IV.1: Physical properties of the fluid model at 25°C
and the molten glass at 1200°C [43]

Material	Density ρ_{FM} [kg/m^3]	Viscosity η_{FM} [Pas]	Electrical conductivity σ_{FM} [S/m]
Fluid model	1280	0.2	0.49
Molten glass*	2350	27	-

*The physical properties of molten glass is provided by SCHOTT AG. The electrical conductivity is not used in the simulation of the mixing process made by the mechanical stirrer.

2.3 Design of the electromagnetic mixer

The inner diameter of the physical model is limited by the inner diameter of the available coils of 86 mm and by the thickness of the used materials as well as the region where the water flows to control the temperature of the fluid model. As a result, a diameter of 56 mm is chosen (see [105]).

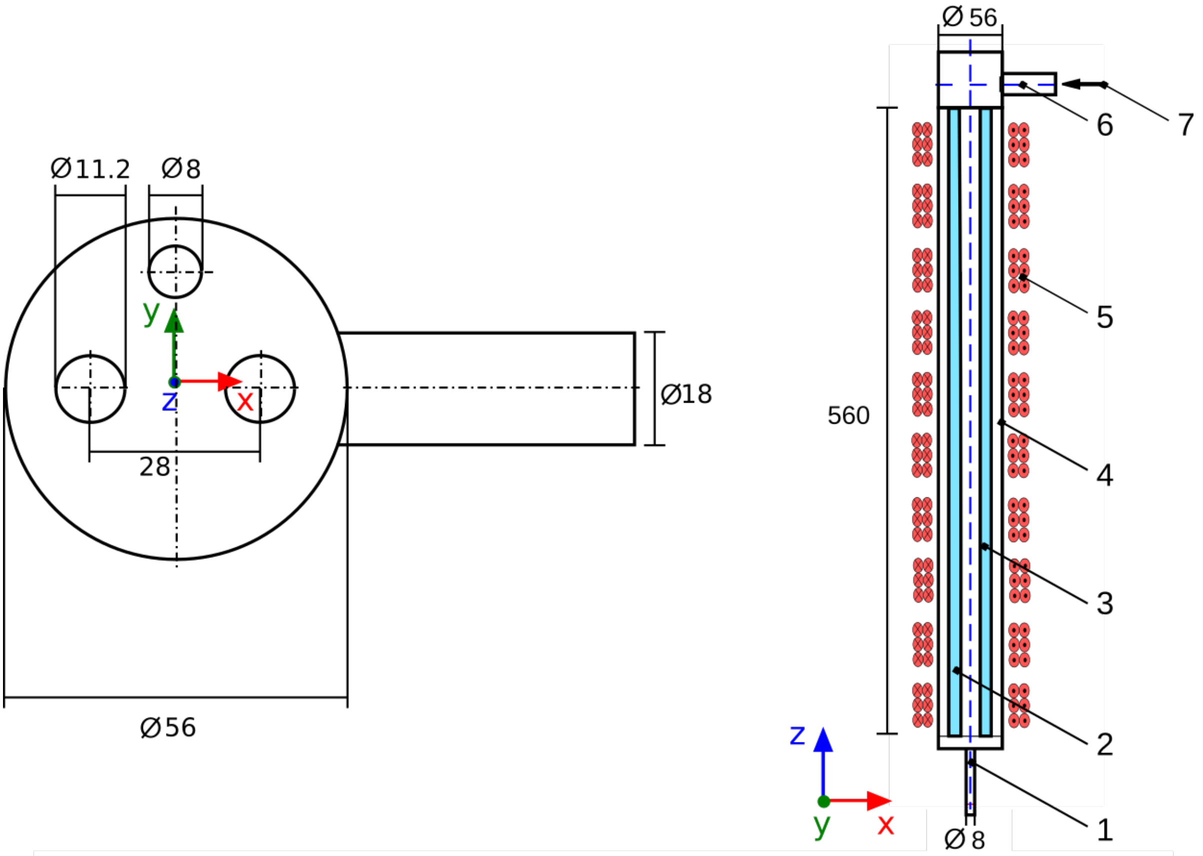

a) b)

Figure IV.2: Schematics of the physical model of the electromagnetic mixer with the geometrical data in mm. a) Top view with the geometrical data in mm. b) Side view with the geometrical data in mm. 1- outlet channel, 2- left electrode, 3- right electrode,4- outer electrode, 5- coils, 6- inlet channel, 7- flow direction.

The optimal ratio between the diameter D_{PM} of the outer electrode and the length of the physical model L_{PM} is described by Eq. IV.2. The optimal ratio between D_{PM} and the diameter of the inner electrodes d_{PM} is described by Eq. IV.3. And the optimal ratio between D_{PM} and the distance between the inner electrodes b_{PM} is described by Eq. IV.4 (results of the parametric study made by [19]).

$$L_{PM} = 10D_{PM} \tag{IV.2}$$

$$d_{PM} = \frac{D_{PM}}{5} \tag{IV.3}$$

$$b_{PM} = \frac{D_{PM}}{2} \tag{IV.4}$$

Therefore, the length of the electromagnetic mixer is set to 560 mm, the inner electrode diameters to 11.2 mm and the separation distance between them to 28 mm. With the ratio of D_{PM} to D_{AG}, D_{AG}/D_{PM} = 4.3 fixed by the Reynolds number (Eq. IV.1), the diameter of the outlet channel is set to 8 mm (Fig. IV.2) and the inlet channel to 18 mm.

2.4 Operating parameters

Pull rates

The pull rate $\dot{m}_{FM}$ of the fluid model is set using the value of the Reynolds number corresponding to the SCHOTT stirring cell (Eq. IV.1) in order to keep the same mass transport behavior in the physical model, the physical properties of the fluid model (Tab. IV.1) and the cross section area of the physical model.

$$\dot{m}_{FM} = \frac{\pi}{4} Re_{PM} \frac{\eta_{FM} D_{PM}}{\rho_{FM}} = 1.34\, ml/min \tag{IV.5}$$

With the pull rate $\dot{m}_{FM}$ = 1.34 ml/min is obtained a mean axial velocity $U_{FM,z}$ of 0.009 mm/s in the electrode regions and of 0.4 mm/s in the outlet channel of the physical model (Fig. IV.2.b).

The physical model is filled with the fluid model using a mechanical pump (Masterflex R, Cole-Parmer). The mean pull rate controlled with a mechanical valve (Fig. IV.3.a) is 1.37 ml/min and it is measured with a point laser of 650 nm and 5 mW (class IIIa, www.hbatchen.co.uk) and a web camera with a resolution in video mode of 640 x 480 pixels (C 170, Logitech).

The laser illuminates the drops coming out from the outlet channel and they are recorded with the camera. Then, the average drop volume of 0.0673 ml divided by the time difference between each drop results in the pull rate (Fig. IV.3.a).

Table IV.2: Used pull rates of the fluid model and of the particle suspension

		Fluid model	Suspension
Pull rate [ml/min]	set value	1.34	0.01
	actual value	1.37	0.01

The quality of the homogenization is determined with the position (x_i , y_i, z_i) of nearly inertia-free, micrometer-sized silicon nitride particles in the outlet channel (specification see section 2.5) which are injected as a suspension (made with the fluid model) at the top of the physical model (Fig. IV.3.c -10) by tritrator (SM-Titrino 702, Metrohm AG) with a pull rate of 0.01 ml/min. This ratio is selected in order to have a good spatial distribution of the particles and to avoid the detection of virtual particles due to the multiple scattering at the moment of the image processing (see section 5).

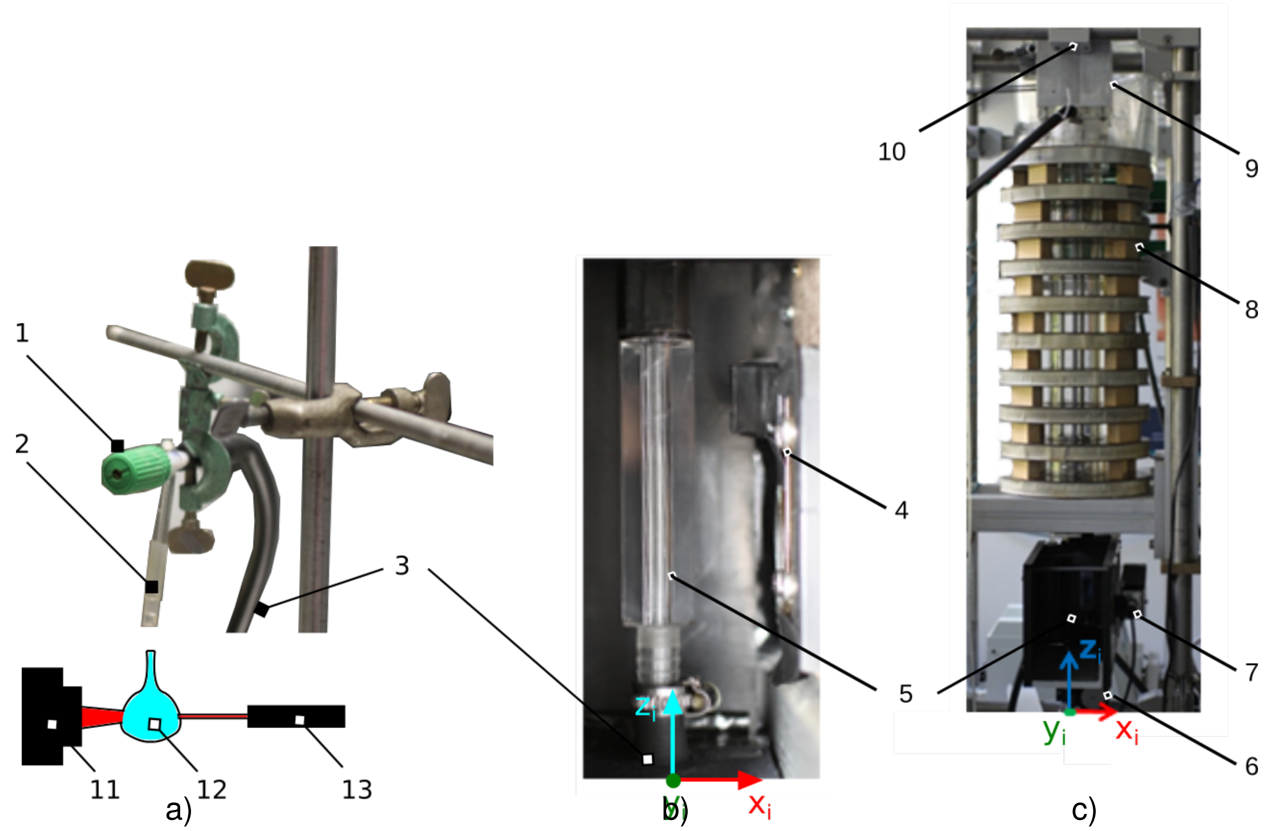

Figure IV.3: a) Photo of the mechanical valve b) Front photo of the outlet channel. c) Front photo of the physical model including the box that contains the camera-laser system. 1- valve, 2- plastic tube connected to the mechanical valve, 3- plastic tube connecting the mechanical valve with the end of the outlet channel, 4- slit of the box window from where comes the laser for the particle detection, 5- outlet channel, 6- box that contains the camera-laser system, 7- laser for the particle detection, 8- coils, 9- outlet channel, 10- position of the particle injection, 11- webcam, 12- model fluid drop, 13- laser for the mass flow measurements.

Temperature control

The electric currents in the coils and electrodes increase the temperature of the fluid model and in the coils by Joule heating. Joule heating depends on the operating parameters and the surrounding temperature. The temperature of the fluid model is stabilized with a water thermostat (F25, JULABO GmbH) fixed at 25 °C and the temperature of the coils is stabilized with an externally installed air blower.

Table IV.3: Measurements of mean temperatures of the electromagnetic mixer

		Fluid model	Coil arrangement
Temperature [°C]	set value	25	25
	actual value	32	43

The temperatures (Tab. IV.3) are measured inside of the fluid model at the top of the electromagnetic mixer and on the surface of one of the coils by means of temperature sensors (LM335Z) controlled by an Arduino Uno SMD board which has an Atmega328P microcontroller (8-bit, Atmel).

Electric current in the fluid model

An electric current $I_{PM,E}$ of 0.78 A with a frequency of 50 Hz (Tab. IV.4) corresponding to a voltage $U_{PM,E}$ of 0.578 V is impressed into the fluid model about one inner and the outer electrode controlled with a regulating transformer (TST 280/6, RFT) and a variable resistor. The AC-RMS of the current is measured with a current meter (VA 18B, TE Electronic) and the shifting between the inner electrodes is done with the Arduino Uno SMD board. The Fig.IV.4 shows the electric circuit energizing the arrangement of three electrodes and thus impressing an electric current in the fluid model.

Table IV.4: Measurements of the mean value of the electric currents

		Electrodes $I_{PM,E}$	Coil arrangement $I_{PM,C}$
Electric current [A]	set value	0.778	6.71
	actual value	0.78	6.73

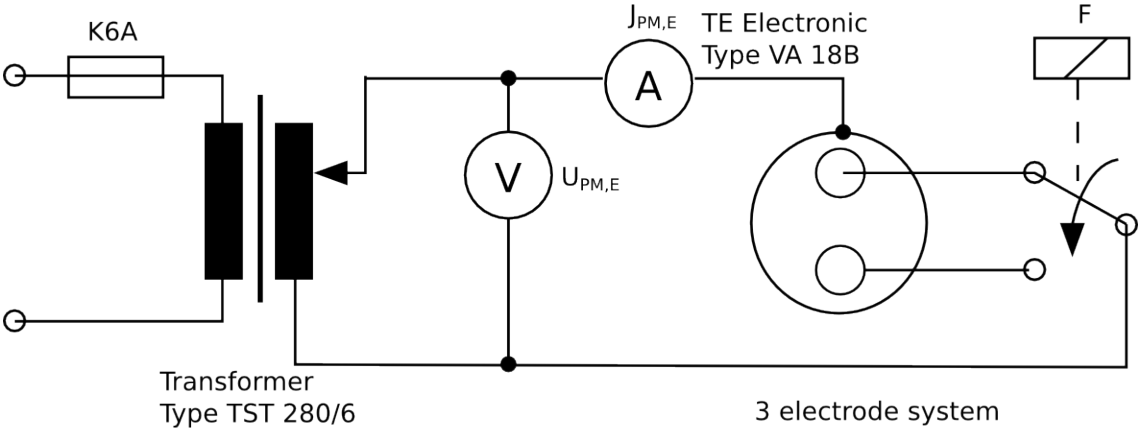

Figure IV.4: Electric circuit for the three electrode system. The electrical activation of the inner electrodes is done with a relay, controlled by the Arduino Uno SMD board with a shifting period of 6120 s and the amount of current $I_{PM,E}$ is controlled manually regulating the value of the variable resistor.

The shifting frequency of the electric activation of the inner electrodes is characterized by a dimensionless switching frequency N_{PM} with an optimal value equal to 12 (results of the parametric study made by [19]). The same study showed that values between 8 and 16 have little influence on the stirring index nevertheless, it was suggested by [105] to set N_{PM} = 10 stating that values bigger than 12 could have a negative impact on the stirring index.

$$N_{PM} = \frac{L_{PM}}{U_{FM,z}\tau_{PM}} = 10 \tag{IV.6}$$

Replacing the length L_{PM} of the physical model and the mean axial velocity $U_{FM,z}$ of the fluid model in the Eq. IV.6 a shifting period τ_{PM} of 6120 s is obtained.

Magnetic field in the fluid model

The magnitude of the magnetic flux density is characterized by the dimensionless parameter M_{PM} (Eq. IV.7) called by [19] "the square of the modified Hartmann number" which is related to the interaction parameter N_{ip} and the Reynolds number Re found in the dimensionless Navier-Stokes equation (Eq. III.18).

The optimal value of M_{PM} is 1000 but the magnitude of the magnetic flux density needed to achieve that value computed with the Eq. IV.7 is of 115 mT which is above the maximum value of 40 mT that the coils can produce [105]. Therefore the mean value of the axial magnetic flux density $B_{PM,z}$ is set to 28 mT [105] which corresponds to M_{PM} = 243.

$$M_{PM} = \frac{\sigma_{FM} V_{FM} B_{PM,z} D_{PM}}{\eta_{FM} U_{FM,z}} = 243 \tag{IV.7}$$

The magnetic field is generated by 10 coils which are located along the axis of the electromagnetic mixer (Fig. IV.3.c). Five of the coils are connected in serial and these two coil groups are connected in parallel (Fig. IV.5).

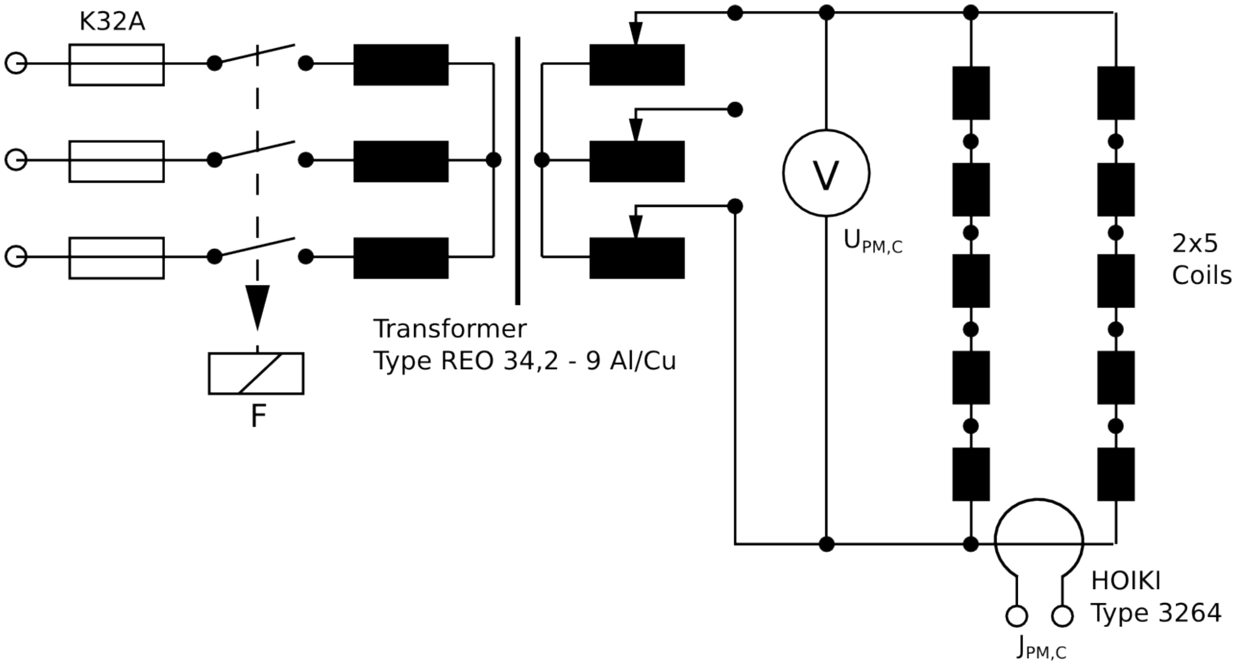

Figure IV.5: Electric circuit for the coil system. The amount of current $I_{PM,C}$ was controlled manually regulating the voltage of the transformer.

The total amount of electric current $I_{PM,C}$ = 6.71 A is controlled by a regulating three phase transformer (Type REO 34,2-9 Al/CU, Transformatoren- und Röntgenwerk Dresden). The AC-RMS value of the total coil current is measured with a clamp amperemeter (Type 3284, Hioki E. E. Cooperation), the AC-RMS magnetic flux density is measured with an axial field sensor (HS-MNK-1904 VH, Magnet-Physik Dr. Steingroever GmbH) and its signal is recorded with a Gauss meter (FH 36, Magnet-Physik Dr. Steingroever GmbH).

The axial field sensor is introduced at the middle and top down on the z-axis of the electromagnetic mixer using a glass pipe as guide with the reference point (z = 0 mm) located at the bottom of the electromagnetic mixer (Fig. IV.2.b).

The measurements are taken from 12 points spacing by 50 mm. Fig. IV.6 shows the z-component magnitude of the magnetic flux density distribution $B_{PM,z}(z)$ in the electromagnetic mixer for an electric current in the coils of $I_{PM,C}$ = 6.71 A.

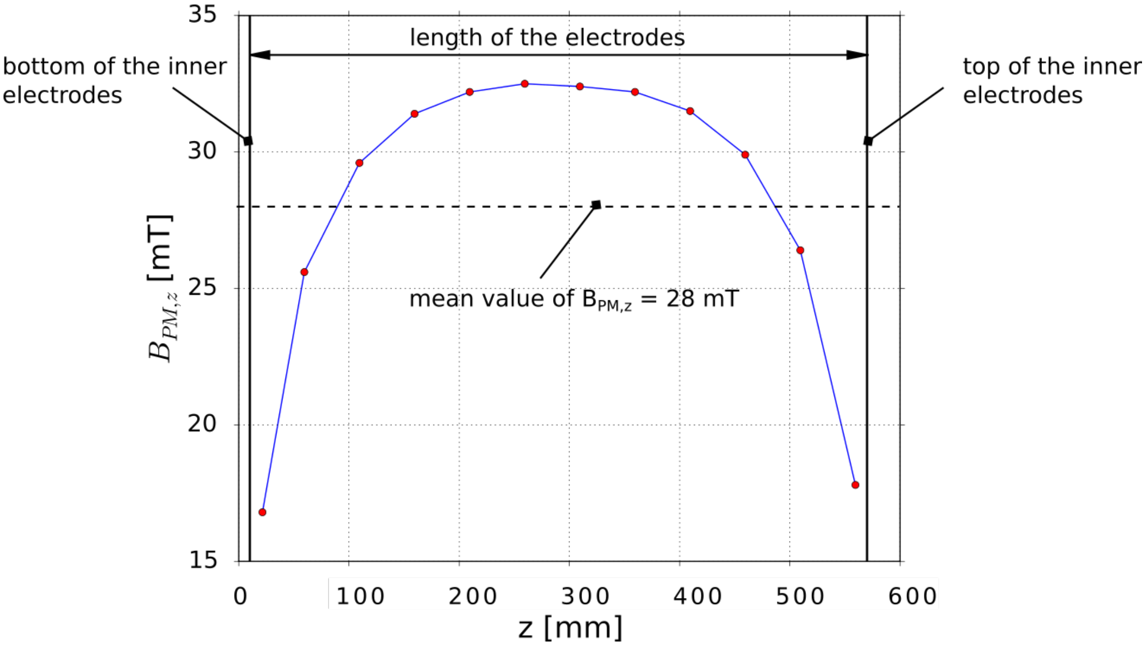

Figure IV.6: Axial magnetic flux density distribution $B_{PM,z}(z)$ at $I_{PM,C}$ = 6.71 A measured in 12 different points spacing by 50 mm with an axial field sensor along the z-axis in the middle of the physical model between the inner electrodes.

2.5 Particle size distribution

The homogenization quality produced by the electromagnetic mixer is characterized with the spatial distribution of silicon nitride particles (Si_3N_4) in the outlet channel which are injected at the top of the mixer as a suspension (Tab. IV.6) made with the fluid model. To reduce its natural agglomeration, the suspension is dispersed mechanically (Ultra-Turrax T25, IKA®-Werke GmbH & Co. KG) and after it, constantly agitated with a magnetic stirrer.
The size distribution of these particles is measured ten times by dynamic light scattering (Zetasizer Nano 3000 HS, Malvern). The Fig. IV.7.a shows the mean frequency distribution H_3(d) from ten measurements, which are weighted with the particle volume. The Fig. IV.7.b shows the associated particle size distribution F_3(d) with a $d_{50,3}$ value of 1.2 μm (Fig. IV.7b).

Table IV.5: Physical and geometrical properties of the particles

Density [kg/m^3]	Particle Size $d_{50,3}$ [μm]
3440	1.2

Table IV.6: Mass and volume of the particles in a suspension made with the fluid model

	Suspension	Fluid model	Particle
mass [g]	800	799.9755	0.0245
Volume [ml] *	622.516	622.549	0.0071

*The volume is calculated with the density and the mass of the particle and the fluid model.

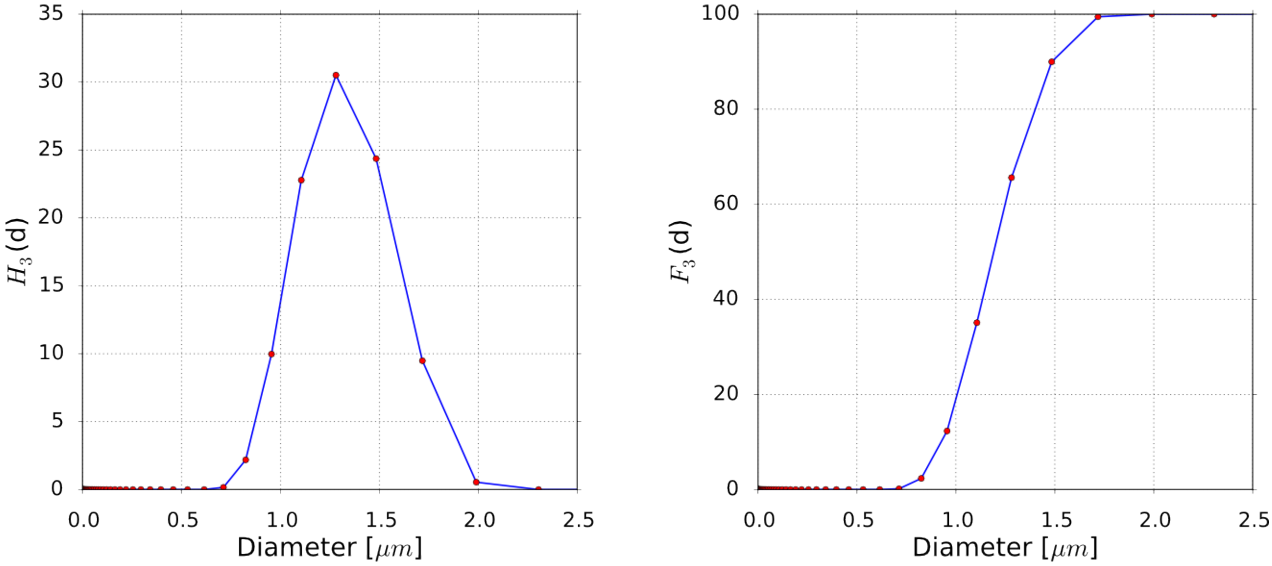

a) b)

Figure IV.7: a) Mean frequency distribution H_3(d) weighted on the particle volume and calculated from 10 measurements, b) mean particle size distribution F_3(d).

3 Numerical study of the physical model

3.1 Numerical implementation of the mathematical model

In the study made by S. Gopalakrisnan [19], it was shown that the time-periodic activation of the inner electrodes can be replaced by an spatial distribution of the electric potential (Fig. IV.8.a) along the inner electrodes and thus obtaining a steady three dimensional flow instead of a time-periodic flow. Therefore, the optimal dimensionless shifting frequency (Eq. IV.6) corresponds now to the number of spatial shifting on the inner electrodes (Fig.IV.8).

The advantages of an steady simulation are twofold; the computation time is reduced significantly and the particle trajectories can be calculated after the computation of the velocity distributions instead of at each time-step of the simulation.

The geometrical model of the electromagnetic mixer's physical model is composed by the surface of the electrodes as well as by the surface of the inlet and outlet channel. It is discretized with a hexahedral mesh containing 3 117 194 cells using the Gambit software v. 2.4.6.

The distribution of the electric current density and the Lorentz force density are computed using the user define functions (UDF) of the commercial software ANSYS/Fluent v.13 and then loaded dynamically by this solver.

After obtaining a steady and well converged simulation with the Fluent solver, the trajectories of these passive particles are computed with the discrete phase model using the Runge-Kutta method. Due to the laminar regime of the flow, it is possible to analyze the particle distributions in a cross section plane of the outlet channel characterized by the stirring index (Eq. III.68).

The boundary conditions applied to the geometrical model are:

- No-slip condition on the electrodes and channel walls (velocity vector equal to zero).
- A pressure outlet at the surface exit of the outlet channel (pressure equal to zero).
- A mass flow inlet of 1.34 ml/min at the surface entrance of the inlet channel.
- An spatial distribution of the electric potential on the inner electrodes of 0 V and 1.16 V.
- An electric potential of 0 V on the outer electrode.

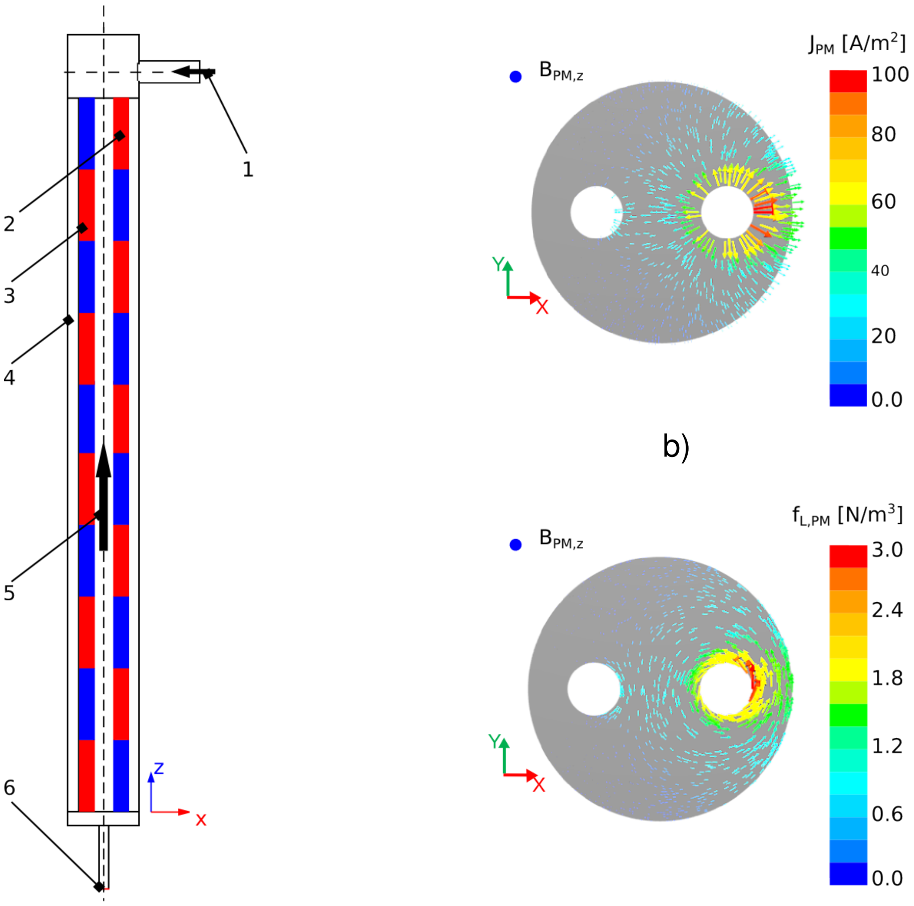

a) b) c)

Figure IV.8: a) Schematics of the geometrical model including the boundary conditions with the active part of the inner electrode in red color and the passive part in blue color. b) Distribution of the electric current density vectors $\mathbf{J_{PM}}$ in a cross section plane x-y at the level of the active part of the right electrode. c) Distribution of the Lorentz force density vectors $\mathbf{f_{L,PM}}$ in a cross section plane x-y at the level of the active part of the right electrode with a maximum value of 3 N/m^3 close to the electrode. 1- mass flow of 1.34 ml/min applied on the inlet channel, 2- right inner electrode and a non-slip condition, 3- left inner electrode and a non-slip condition, 4- outer electrode with an electric potential of 0 V and a non-slip condition, 5- externally created magnetic flux density of 28 mT, 6- pressure outlet condition applied at the outlet channel.

3.2 Numerical results

Velocity distributions

The Fig. IV.8.b shows the computed electric current distribution $\mathbf{J_{PM}}$ in the fluid model which interacts with the constant axial magnetic flux density $\mathbf{B_{PM}}$ that cross the fluid creating a Lorentz force density distribution $\mathbf{f_{L,PM}}$ in it (Fig.IV.8.c) with a maximum value of 3 N/m^3 close to the active part of the inner electrode.

The computed velocity distribution shows that the Lorentz force density creates an additional flow in the x-y plane with a maximum velocity magnitude of 0.15 mm/s (Fig. IV.9.a) to the flow imposed by the pull rate of 1.34 ml/min.

The additional flow in the x-y plane is almost fifteen time faster than the mean axial velocity of 0.009 mm/s.

Therefore, the Lorentz force density can control the laminar flow, driving the flow around the active part of the inner electrodes, stretching and folding the fluid as it is shown in the Fig. IV.9.b by the velocity streamlines.

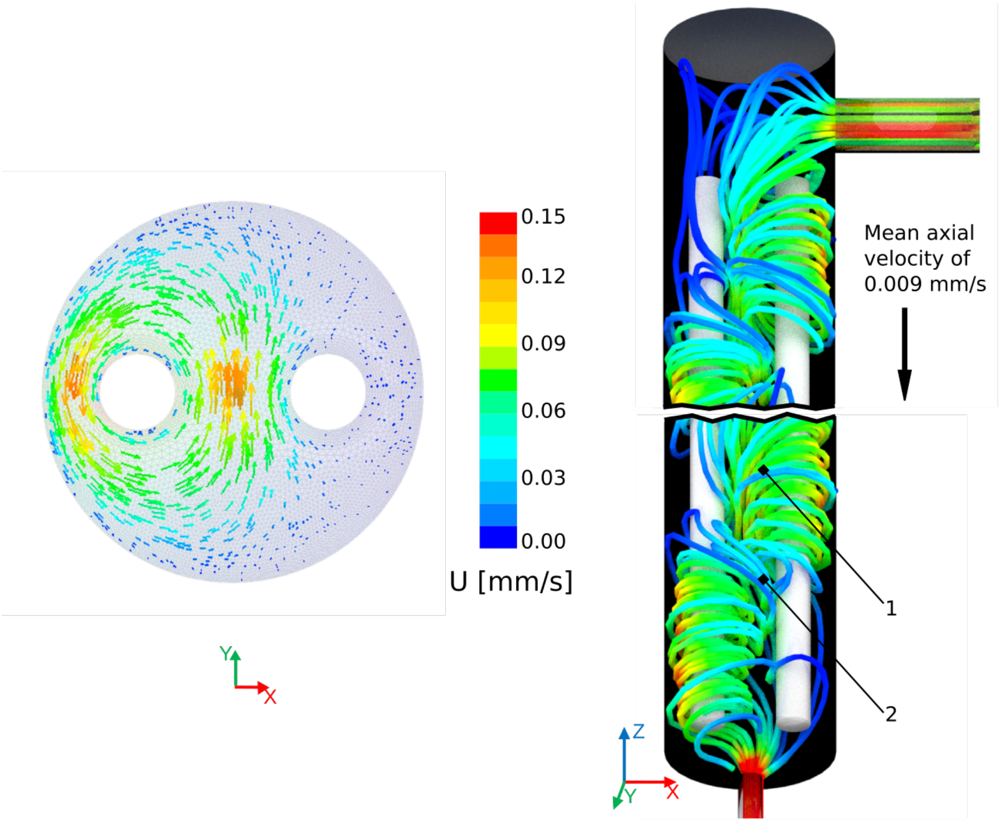

a) b)

Figure IV.9: a) Distribution of the velocity vectors in a cross section plane x-y at the level of the active part of the left electrode with a maximum magnitude of 0.15 mm/s close to electrode for a pull rate of 1.34 ml/min. b) Perspective view of the velocity streamlines colored by the velocity magnitude with a maximum value of 0.15 mm/s close to the active part of the electrode for a pull rate of 1.34 ml/min. 1- folding of the fluid, 2- stretching of the fluid.

3.3 Particle distributions

In order to quantify the mixing capabilities of the Lorentz force density by stretching and folding the fluid, 50 000 massless particles are injected into the inlet channel distributed in a square area of 4 mm^2 over the total cross section area of the inlet channel of 255 mm^2 (Fig. IV.10.b).

The particle positions are determined at each step-time with the velocity distribution of the flow (Fig. IV.9). Initially, the particles start going around the active part of the inner electrodes.

But after a time grater than 6000 s, it presents a chaotic distribution (Fig. IV.10.b) which is a necessary condition to have a good homogenization (see section 5).

Therefore, as presented in the study by [19], it is necessary that the electromagnetic mixer is enough long to obtain a chaotic distribution which increases the residence time of the particles.

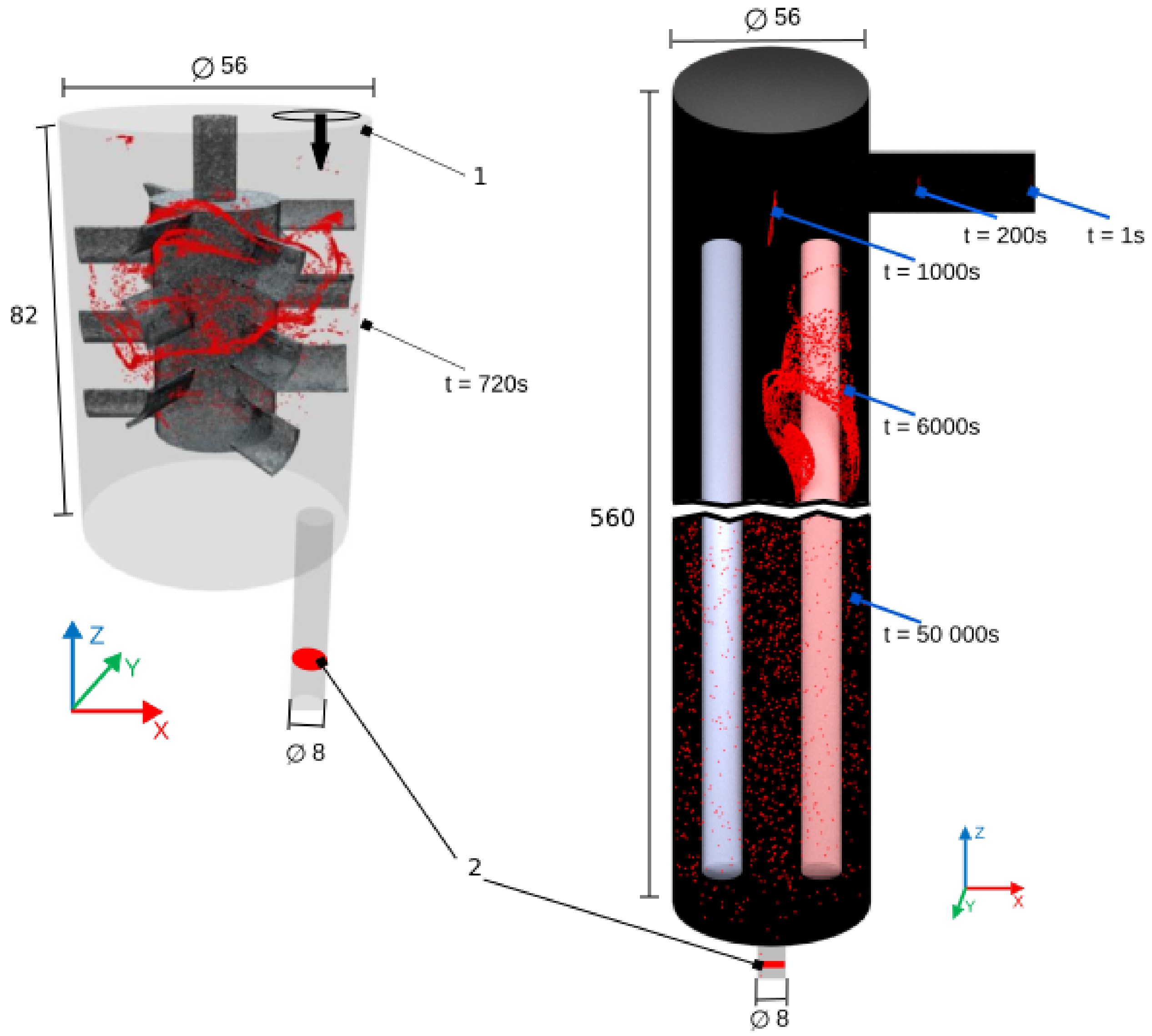

a) b)

Figure IV.10: a) Particles distribution in the mechanical mixer at 720 s with an initial square distribution of 4mm^2 for a pull rate of 1.34 ml/min. b) Particles distribution at different times with an initial square distribution of 4mm^2 for a pull rate of 1.34 ml/min. 1- inlet channel of the mechanical mixer, 2- cross section plane of the outlet channel.

3.4 Stirring index

The mixing process only happens where the Lorentz force exists. When the particles reach the outlet channel, they travel vertically following the velocity streamlines, therefore, the particles keep the same spatial distribution (x_i,y_i) along the axis of the outlet channel.

The quantification of the mixing grade is based on the computed stirring index (Eq. III.68) in a cross section plane of the outlet channel (Fig. IV.10). The computation of the stirring index is made with 50 000 particles and 1600 boxes of 0.2 mm covering the cross section plane. This particle number is selected by increasing its number until obtaining a constant value for the index.

The potential of the Lorentz force technique is illustrated comparing its stirring index (0.71), with that of the mechanical stirrer (0.69) provided by SCHOTT AG.

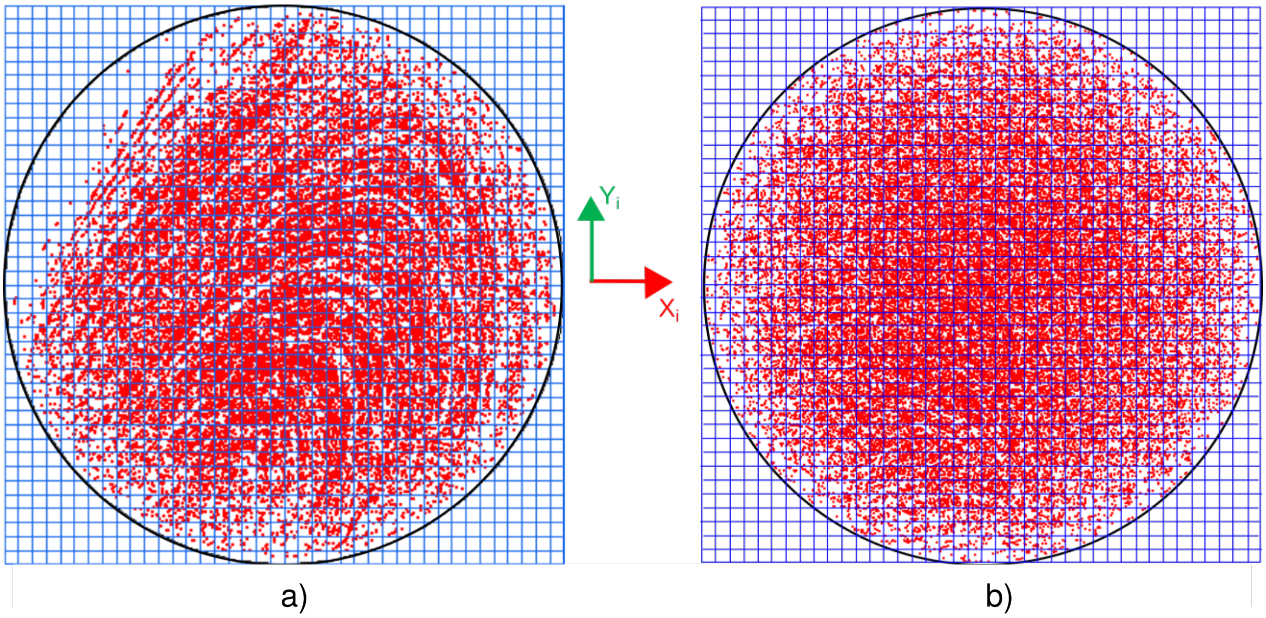

a) b)

Figure IV.11: a) Distribution of 50 000 particles in a cross section plane of the outlet channel of physical model of the mechanical stirrer using a flow rate of 1.34 ml/min and a rotation speed of 8 min^{-1} which gives an stirring index of 0.69. b) Distribution of 50 000 particles in a cross section plane of the outlet channel of the physical model of the electromagnetic mixer using a flow rate of 1.34 ml/min which gives an stirring index of 0.71.

The Fig.IV.11 shows a clear difference between the mixing capabilities of the mechanical stirrer and the electromagnetic mixer, with a clear advantage for the later one despite the similarities on the stirring index. The calculated distribution of the particles in the outlet channel shows clearly inhomogeneities interpretable as cords due to the mechanical stirrer rotation. The stirring index cannot catch these differences because it is a global index that average the difference between the number of particles in each box and the optimal number.

The SCHOTT stirring cell that contains the mechanical stirrer (Fig. IV.1) is down-scaling following the same procedure as for the physical model of the electromagnetic mixer. The physical model of the stirring cell is discretized with a mesh containing 17 millions of cells. The rotation speed of the mechanical stirrer is computed with the Reynolds number evaluated at the end of the stirring blades having a value of 7 and giving a rotation speed of 8 min^{-1}.

4 Experimental study

The numerical results performed on the physical model of the electromagnetic mixer has to be verified with an experimental study to show that the numerical implementation of the mathematical model can describe the reality with enough accuracy. This verification is made comparing the computed with the measured stirring index which is determined with the spatial distribution (x_i , y_i, z_i) of nearly inertia-free silicon nitride micrometric particles. A camera-laser system is used to record the scattered laser made by the particles while they travel through the outlet channel and a self-developed image processing technique is used to determine their positions (x_i , y_i, z_i) from the recorded images.

4.1 Camera-Laser system for the particle imaging

The CCD camera (500D, Canon) and the line diode laser (class IIIa, Pegasus Lasersysteme GmbH) (Tab. IV.8) are fixed in a wooden box which is screwed in a position control unit (PS10, Owis GmbH) (Tab. IV.7) and this in an optical breadboard plate (Fig. IV.12 and IV.13.a). The software that operates the camera-laser system and the step motor is written in the C++ programming language using the EOS Digital Software Development Kit EDSDK from Canon Inc. [112] and the commands provided by OWIS GmbH [110]. This software controls the CCD camera via usb port and the step motor via serial port.

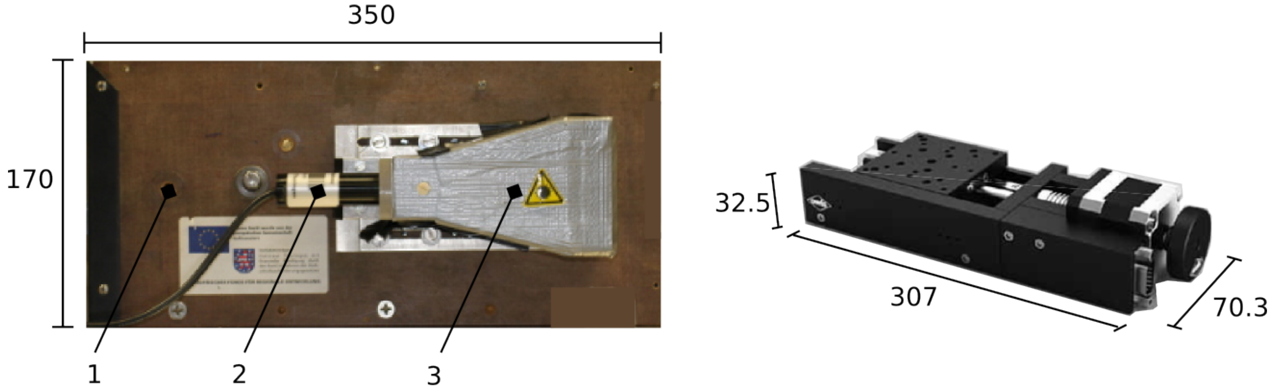

a) b)

Figure IV.12: a) Photo of the box with its geometrical data in mm including 1- the attachment position of the camera, 2- the diode laser, 3- mirror to change the direction of the laser to the slit. b) Photo of the single-axis position control unit with a step motor (PS10, Owis GmbH) having its geometrical data in mm.

Table IV.7: Single-axis position control unit with a step motor (PS10, Owis GmbH)

Maximum speed [mm/s]	Maximum load capacity [N]	Maximum moment of tilt [Nm]	Positioning error [μm/mm]
10	100	7.5	1/100

Table IV.8: Properties of the camera-laser system

	Parameter	value
Diode laser (Class IIIa, Pegasus Lasersysteme GmbH)	Power [mW]	100
	Wave length [nm]	660
	Thickness [mm]	1
CCD camera (500D, Canon)	Type [mm x mm]	CMOS (22.3 x 14.9)
	Pixel size [μm x μm]	4.68 x 4.70
	Objective	50mm F2.8 Ex DG, Sigma
	Shutter speed [s]	1/200
	ISO	6400
	Picture size [px x px]	4752 x 3168 (JPEG)

The laser sheet emitted by the diode laser, goes parallel to the y_i-axis of the outlet channel. Then it is reflected into the mirror towards the direction of the x_i-axis crossing the slit of the box to reduce its thickness up to 0.2 mm (Fig. IV.13.a). The laser scattered by the silicon nitride particles located in the outlet channel (Fig. IV.13.b) is recorded by the CCD camera with its lens aligned perpendicular to the laser sheet (parallel to the y_i-axis).

The determination of the particle positions on the laser sheet plane is made with the image processing technique and in order to do a 3D-scanning of a region of the outlet channel volume, the camera-laser system (Fig. IV.13.a) is moved by the position control unit in steps of 0.01 mm from one corner of the outlet channel to the another.

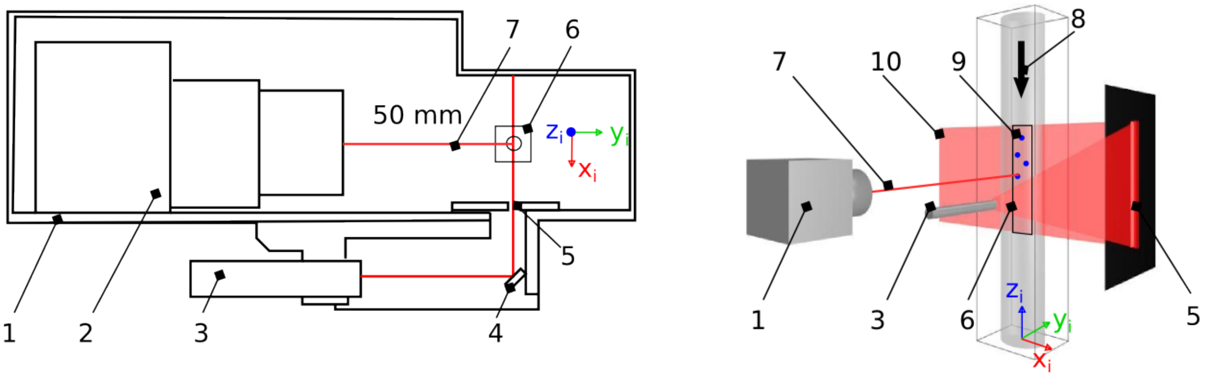

a)

b)

Figure IV.13: a) Schematic of the top view of the camera-laser system inside of the box. b) Schematic of the camera-laser system and the outlet channel. 1- box, 2- CCD camera Canon 500D, 3- laser diode, 4- mirror, 5- slit, 6- outlet channel, 7- scattered laser by the particles, 8- direction of the flow, 9- particles, 10- laser sheet.

4.2 Image processing

Particle detection

Due to the geometry of the outlet channel that acts as a cylindrical lens and the refraction index of the air, of the model fluid and of the material of the outlet channel (Tab. IV.9), it is necessary to compute the refraction of the laser to determine its intensity distribution.

Table IV.9: Optical properties

	PMMA n_p [1]	Fluid model n_f [1]	Air n_a [1]
Refraction index	1.49	1.45	1

This computation is made analytically with the Snell's law (Fig. IV.14.a) as well as with the ZemaxTM software using the non-sequential ray tracing method [108]. This software models the CCD sensor of the camera (Tab. IV.8) as a matrix of same dimensions (22.3 mm x 14.9 mm and 4752 x 3168 pixels), the lens of the camera as a paraxial lens and the particle as a point source (Fig. IV.14.b).

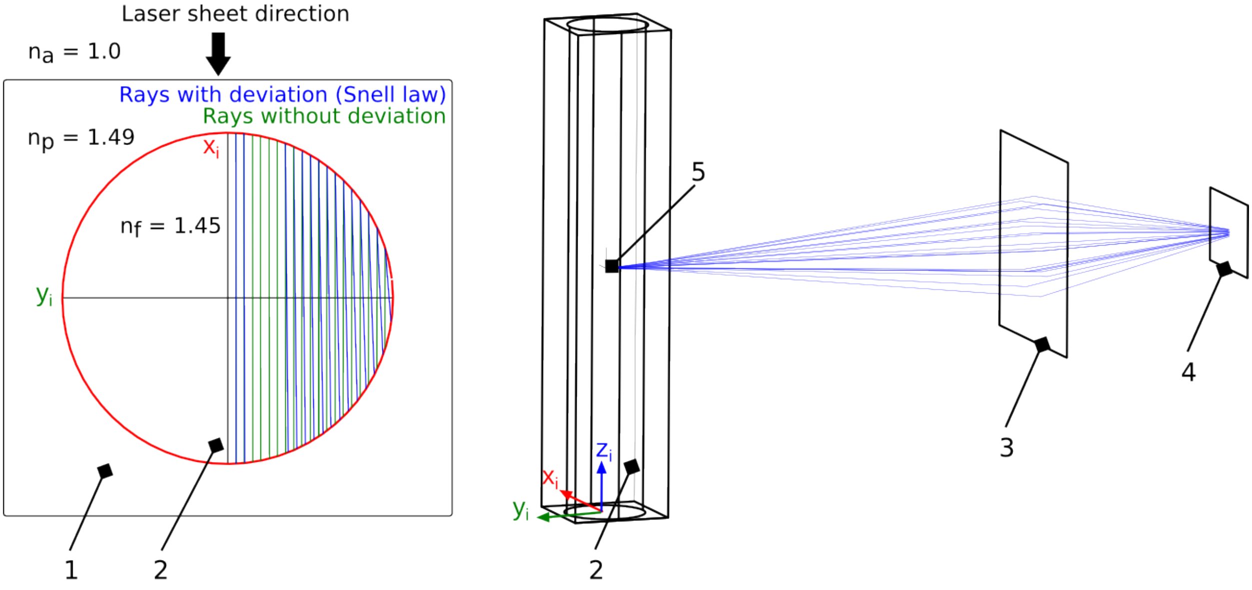

a) b)

Figure IV.14: a) Diffraction of the laser sheet computed with the Snell's law at different points. b) Optical simulation with the ZemaxTM software of the ray path produced by a point source. 1- channel exterior, 2- outlet channel, 3- paraxial lens, 4- CCD camera, 5- point source.

The numerical computation of the intensity distribution of the focused point source (Fig. IV.15.a) shows an elongation in the z_i-axis direction due to the shape of the outlet channel that is also found in the intensity distribution recorded by the camera (Fig. IV.15.b). The difference between the measurement and the simulation comes from the focus plane of the camera as well as the temporal fluctuations of the scattered intensity due to the exposure time (Tab. IV.8, shutter speed).

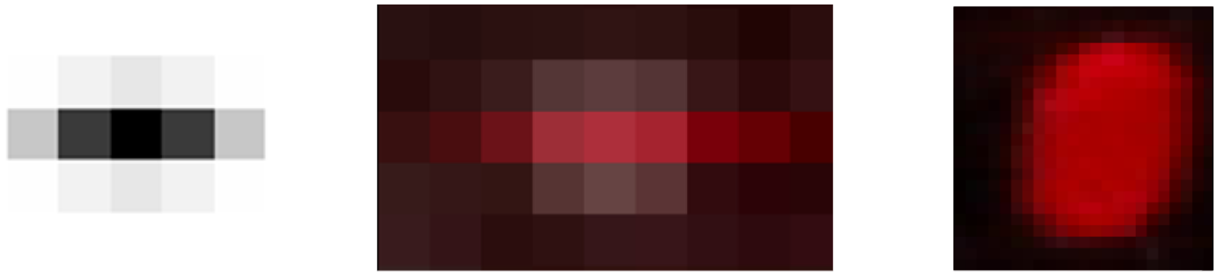

a) b) c)

Figure IV.15: Intensity distribution of the scattered laser. a) Numerical simulation of a focused particle. b) Image recorded of a focused particle. c) Image recorded of an out of focused particle that contains a lot more pixels than the previous cases.

Unfortunately this distribution can also be produced by scratches on the surface of the channel. To overcome this problem, the focus plane of the camera is moved (Fig. IV.16.a) to have the particles out of focus which produces an elongated circular intensity distribution (Fig. IV.15.c).

Another problem could be that the laser scattered from particles located close to borders of the channel could fall outside of the camera lens. The problem is resolved reducing the initial distance between the camera lens and the outlet channel from 92 mm [104] to 50 mm (Fig. IV.16.b).

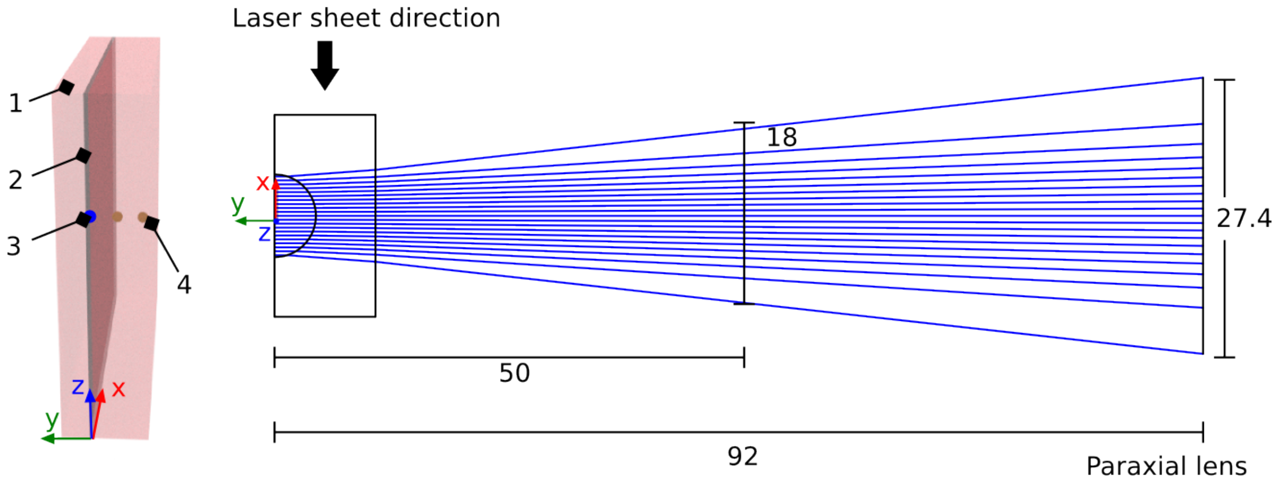

a) b)

Figure IV.16: a) Particles inside the laser sheet with 1-laser sheet, 2- focus plane, 3- particle in focus, 4- particle out of focus. b) Ray paths for different position of the point source in the x_i-axis direction inside the outlet channel.

Dynamic out of focus method

The Fig. IV.15.b shows the intensity distribution of the scattered laser due to a particle located in the focus plane of the camera (Fig. IV.16.a), but this distribution can be also produced by scratches on the surface of the outlet channel. To distinguish the intensity distribution produced by the particles from other sources (e.g. scratches), the focus plane of the camera is moved until obtaining a rounded shape. (Fig. IV.15.c).

This focus plane is recalibrated after some steps of the camera-laser system to follow the refraction of the laser sheet (Fig IV.14.a) which increases when it goes far from the center. In the case that the calibration is done only once, after some steps, the intensity distribution (Fig. IV.15.c) spreads in a bigger area until becoming completely blurred.

Determination of the particle position and number

The out of focus technique helps to distinguish the intensity distribution produced by the particles from other sources (scratches) but in order to filter sources that could have also a rounded shape due to this technique, the camera takes two pictures at each step.

In each step of 0.01 mm of the camera-laser system moved by the step motor from one corner to another of the outlet channel, the scattered laser is recorded twice with a delay of 343 ms. This results in 820 pairs of images which are used by the image processing technique to determine the tri-dimensional position of the particles. The delay is determined using the maximum and minimum speed of the particles that are found in the middle and close to the inner surface of the outlet channel respectively. Also the maximum distance traveled by the particles before overlapping another particle found in the same path line determines the delay. The idea is to take into account only the distribution that suffers a displacement in the z_i-axis direction reflecting the particle vertical flow due to the laminar regime of the fluid.

The self-developed image processing technique is written in the C++ programming language using the vision library OpenCV v.2.4 [113] and the user interface library Qt v4.7 [111]. This software analyses each pair of images simultaneously and involves the following steps:

1. First, it is selected a suitable region of interest (Fig. IV.17.a), where the quality of the image is not degraded by bigger scratches of the outlet channel, with a height of 10 mm and a width fixed by the position of the step motor (Fig. IV.13.b).
2. Then, the pair of images is transformed into a grayscale with values from 0 to 255 and subtracted one to the another to reduce the noises and to eliminate the reflection on the borders of the channel (Fig. IV.17.b).
3. After that, a threshold between 45-200 depending on the position of the camera-laser system is applied in the region of interest. The remaining noise is blurred with a Gaussian filter (low-pass filter) that spreads the intensity distribution (Fig. IV.17c).
4. Finally, a high-pass filter based on the convolution between the pair of images and a mask (matrix) is used to determine the contour of each rounded intensity distribution

(Fig. IV.17.d) with its center corresponding to the coordinates x_i and z_i of a possible particle. The coordinate y_i of the possible particle equals the position of the step motor in the y_i-axis.

5. Then, if this center truly corresponds to a particle position, it must suffer a displacement in the z_i-axis direction which is determined by a cross-correlation between both images (Fig. IV.17.e).

Following these steps for each pair of images, the particle distributions in a volume of the outlet channel are reconstructed and due to the laminar regime of the fluid, these particles flow vertically. Therefore it is possible to analyze the quality of the homogenization in a cross section plane of the outlet channel and for that purpose, the particle positions are projected in that plane (Fig. IV.17.f).

It is noticed that the image processing technique could not resolve particles close to the walls of the outlet channel because the scattering of the laser on them is distributed in almost the whole image covering the scattering from the particles. Therefore, the particle distributions in the cross section plane showed in the Fig. IV.17.f corresponds to an area of diameter 7.8 mm instead of the initial diameter of 8.2 mm.

The total number of detected particles in this set of images are of 17653 using a pull rate of 1.37 ml/min for the fluid model and of 0.01 ml/min for the suspension which contains the particles. The expected total particle numbers is of 48704 with an standard deviation of 1638. This expected number is computed with the volume occupied by the particles and the median value of mean particle size distribution $d_{50,3}$ = 1.2 μm (Fig. IV.7.b). The occupied volume is calculated multiplying the scanned volume with the volume ratio particles/suspension and the pull rate ratio suspension/fluid model (Tab. IV.10). Finally, an arbitrary number of particles is multiplied by the mean particle size distribution and changed until the sum of the multiplication match the volume occupied by the particles.

Table IV.10: Computation of the expected volume occupied by the particles

	Parameter	value
Geometrical data of the scanned volume	Height [mm]	10
	Diameter [mm]	7.8
	Volume [ml]	0.4778
Volumina	volume of the particles [ml]	0.0071
	Volume of the suspension [ml]	622.516
	Pull rate of the suspension [ml/min]	0.01
	Pull rate of the model fluid [ml/min]	1.37
Volume occupied by the particles [ml]		$3.978\text{x}10^{-8}$

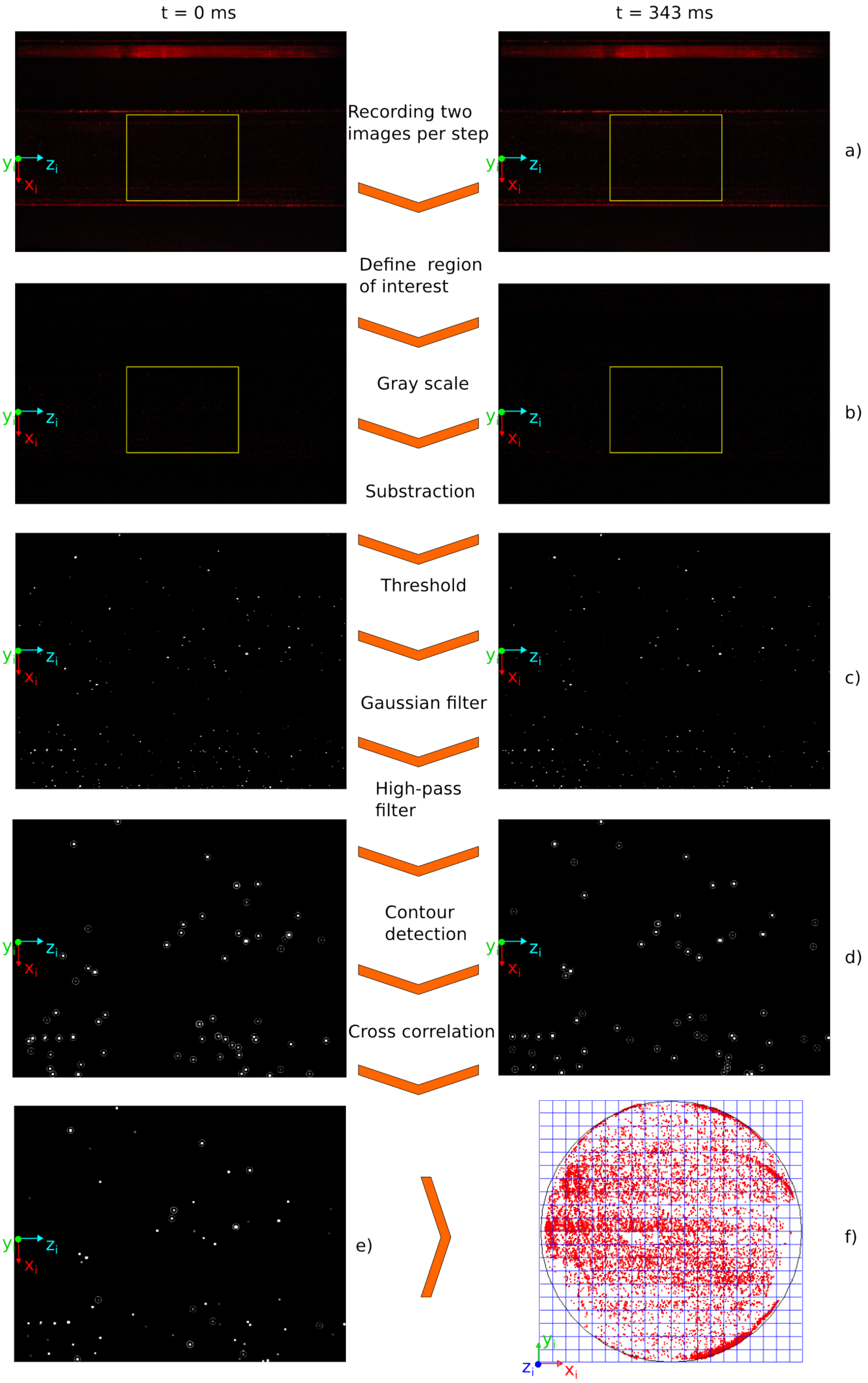

Figure IV.17: Steps involved in the image processing technique. a) Recording of two images at the time 0 ms and 343 ms and selection of the region of interest (yellow). b) Transformation to a gray scale and subtraction of one image with another. c) Threshold and Gaussian filter (low-pass filter). d) High-pass filter to determine the contour of each intensity distribution. e) Cross-correlation between the two images to determine the particle displacements. f) Particle distribution projected in a cross section plane of the outlet channel.

4.3 Conclusions and recommendations

The camera-laser system together with the image processing helped to detect 17653 particles which are 36 % of the expected number of particles. There are several factors that reduce the capabilities of this technique to detect particles such as:

- The laser scattered by the particles located close to the walls of the outlet channel overlaps the laser scattered by the scratches on the outlet channel wall, so that those particles are eliminated from the detection.
- The thickness of the laser sheet allows to have different focus planes inside of it blurring some particles. But decreasing the thickness with an smaller slit has the drawback of reducing the intensity of the scattered laser and thus the signal-to-noise ratio.
- The JPEG format of the camera reduces the quality of the pictures blurring some particles and also the color depth of the pictures of 8 bits reduces the capabilities to detect particles with weak scattering. But it has the advantage to use less storage capacity of the camera so that a quicker measurement and image processing is possible.
- The diffraction of the laser sheet (Fig. IV.14.a) forces the calibration of the threshold and the focus plane at each step. But they are calibrated each few steps and not in each 820 steps blurring at some point some particles.
- The distance between the focus plane and the laser sheet is not constant along the x_i-axis due to the refraction. Therefore, the particles located far from the calibration region (in the x_i-axis) appear more blurred reducing the possibility to detect them.

The particle positions determined by camera-laser system together with the image processing depend on the laser sheet refraction which is related with the perpendicularity between this laser sheet and the external rectangular walls of the outlet channel (Fig. IV.16). Therefore, due to its manual adjustment, it produces errors in the determination of particle positions. Also, the slit used to reduce the thickness of the laser sheet adds some distortions in the rectangular shape of it introducing errors in the particle positions.

These problems could be resolved using a rectangular channel instead of a cylindrical one, which would eliminate the refraction of the scattered laser caused by the cylindrical shape (angle of incidence) of the outlet channel. Therefore, it wouldn't be necessary to correct the position of the particles using the Snell's law neither the adjustment of the camera focus plane and the threshold each few steps.
Also, the thickness of the laser sheet can be improved printing a black region to catch the laser with a lithographic method leaving untouched the rectangular slit region with the desirable thickness. And in order to reduce the loss of energy of the laser due to the slit, the laser thickness could be reduced with an optical system before it crosses the slit. This will allow the usage of thinner slit which will improve the spatial resolution of the particles and thus the out of focus technique.

5 Validation of the numerical results

For the validation of the numerical results, the mixing grade produced by the Lorentz force is analyzed using spatial positions of silicon nitride particles of microscopic size, in the outlet channel. Then, with the described image processing technique, the stirring index is calculated with the 17 653 detected particles together with a box size of 0.2 mm obtaining a value of 0.63.

The numerical simulations performed on the physical model are made using an electric current of 1.56 A corresponding to 1.16 V (see section 3) and the stirring index is computed with 50 000 particles. Therefore, to make a proper comparison and validation of the numerical results with the experimentally determined stirring index, a simulation with an electric current of 0.78 A corresponding to 0.57 V is performed and the simulated stirring index is calculated with 10 000 particles giving a value of 0.68.

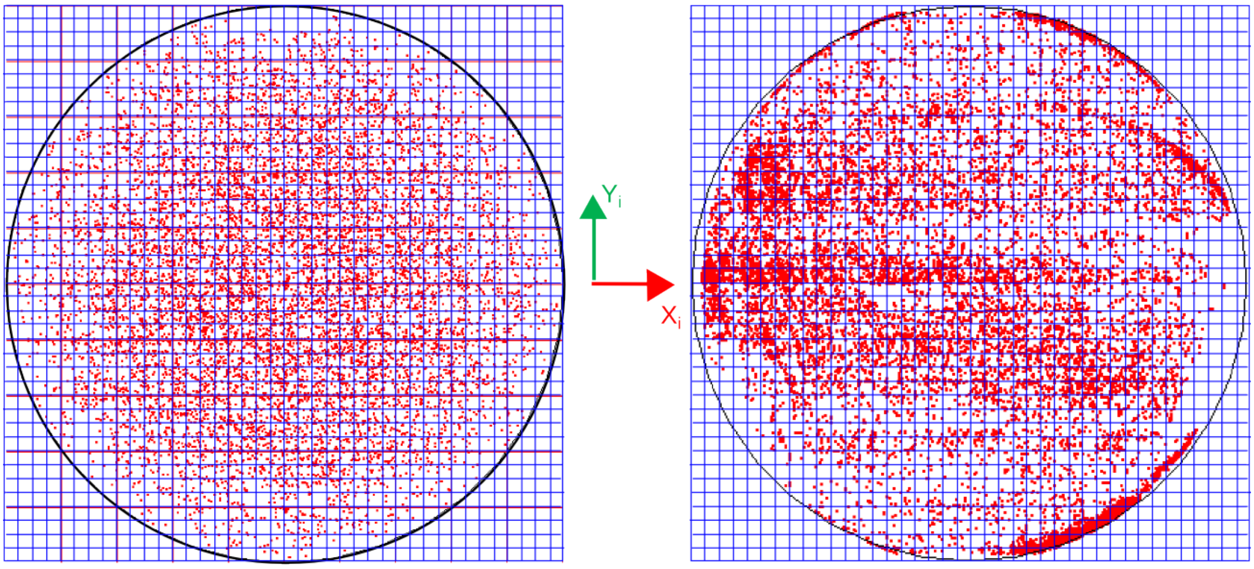

a) b)

Figure IV.18: Particle distributions in a cross section plane of the outlet channel of the physical model used to compute the stirring index in a grid of 1600 boxes of 0.2 mm. a) Numerically calculated distribution of 10 000 particles for a flow rate of 1.34 ml/min, a mean magnetic flux density of 28 mT and an electric current impressed in the model fluid of 0.78 A which gives a stirring index of 0.68. b) Experimentally determined distribution of 17 653 particles for a flow rate of 1.37 ml/min, a mean magnetic flux density of 28 mT and an electric current impressed in the model fluid of 0.78 A. which gives an stirring index of 0.63.

The figures IV.18.a and IV.18.b show in a cross section plane of the outlet channel the measured and the simulated particle distribution respectively where the experimentally determined stirring index (0.63) deviates in 7 % from the simulated stirring index (0.68). Therefore the mathematical model is able to reproduce the stirring index computed experimentally although the particle distributions are different.

This difference comes from the several limitations in the particle detection technique (see section 5), one of biggest responsible being the calibration of the camera focus. This calibration is made each few steps of the camera-laser system using a region of the recorded image, but due to the diffraction of the laser sheet caused by the cylindrical outlet channel, the camera focus plane (perpendicular to the y_i-axis) is not parallel to it. Therefore, when the selected region has the desired intensity distribution, the intensity of the regions far from this start to become blurred until mixing with the background noise.

The Fig. IV.18.b corresponding to the measured particle distribution shows that some regions in the x_i-axis direction have larger particle density than far from it.

This is consequence of wall effects. Still cannot be assumed the same particle distribution, the experiment confirms the usefulness of the mathematical model to evaluate the homogenization without considering the thermal effects.

6 Scale up to a real electromagnetic mixer

6.1 Extension of the mathematical model

With the validated mathematical model, now it is possible to analyze numerically with confidence the effect of the Lorentz force technique in a real electromagnetic mixer, with a standard soda-lime glass as well as a realistic mass flow inlet and a realistic wall temperature on the feeder.

For that, The mathematical model used in the numerical simulation of the physical model must take into account the heat transport equation as well as the dependencies on the temperature of the physical properties affecting the Lorentz force density distribution and thus the molten glass flow.

Otherwise, the numerical simulation follows the same procedure as in the simulation performed on the physical model, but with an additional boundary condition, which is a constant temperature on the external wall. The computed velocity distribution is used to calculate the trajectories of a group of particles, which are analyzed in a cross section plane of the outlet channel and characterized by the stirring index. Here, it is necessary to make a parametric analysis to find the best stirring index because the optimal parameters found by [19] are not anymore valid.

6.2 Geometrical data and physical properties

The geometrical data of the real electromagnetic mixer is based on the SCHOTT stirring cell (Fig. IV.1). The mechanical stirrer is replaced by two inner electrodes and one outer electrode keeping the diameter of 240 mm, the inlet channel diameter of 80 mm and the outlet channel diameter of 35 mm of the stirring cell. The length of the feeder is determined by the available electrode lengths needing to be as long as possible to achieve a good mixing.

In this study, the geometrical data of the electrodes as well as their physical properties are taken from Plansee SE [109]. Molybdenum electrodes are selected with a diameter of 60 mm and a length of 960 mm (the recommended length is from 12 to 16 times the electrode diameter [109]) which can support a maximum electric current density of $2\text{x}10^4$ A/m^2. Therefore, the length of the real electromagnetic mixer is 960 mm which is 4 times its diameter and not anymore 10 times its diameter as in the physical model (Fig. IV.19.b).

The separation distance between the inner electrodes follows the optimal relation found by [19] (Eq.IV.4) giving a value of 120 mm.

The physical properties of the molten glass, such as density, viscosity and electric conductivity, are taken from the DGG standard soda lime glass Ia (Tab.IV.11). The specific heat is taken from [17] and the effective thermal conductivity from the start-up project "High-performance Forehearth Coloring using Lorentz Forces" [63].

Table IV.11: Physical properties of the molten glass

Parameter	Value / Temperature dependencies in °C
Density [kg/m^3]	$\rho_{RF}(T) = 2508.43 - 0.15T$
Dynamic viscosity [Pas]	$\lg(\eta_{RF}(T)) = -3.63 + 6715.62T^{-1}$
Electric conductivity [S/m]	$\lg(\sigma_{RF}(T)) = 3.59 - 2602.20T^{-1}$
Specific heat [J/(Kg·K)]	$Cp_{RF} = 1285$
Effective thermal conductivity [W/(K·m)]	$k_{RF} = 90$

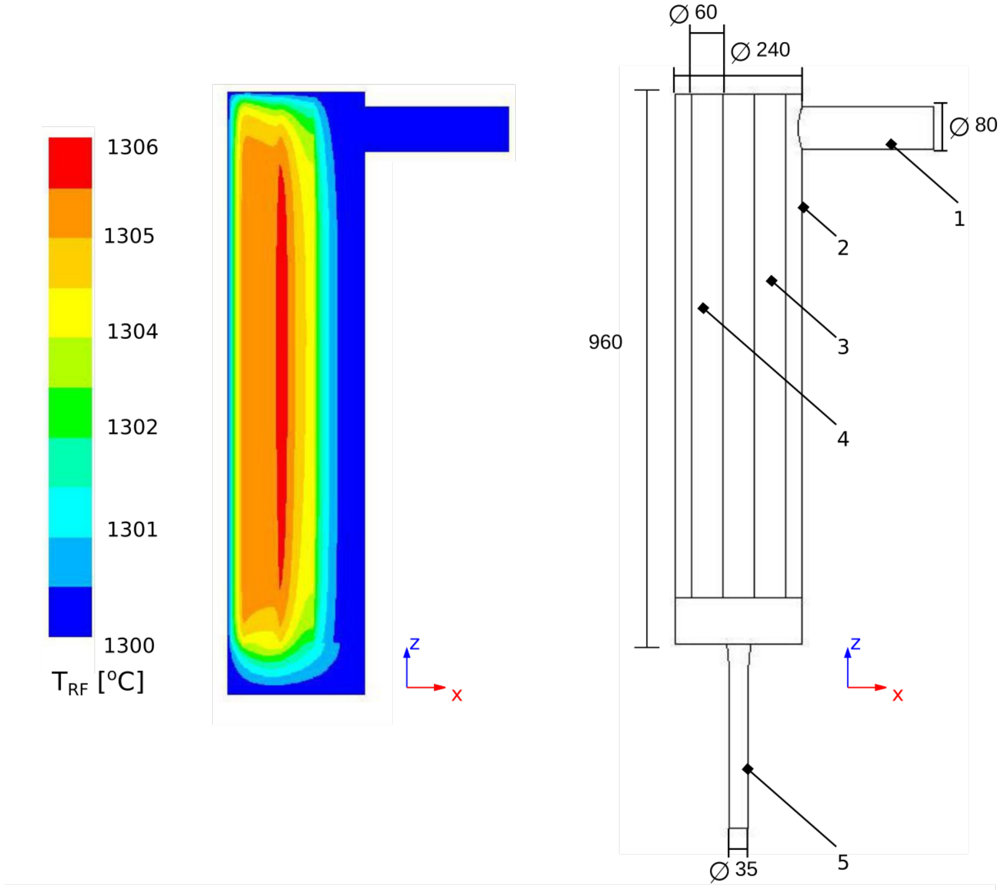

a) b)

Figure IV.19: a) Temperature distribution in a vertical plane (x, y, 0) mm of the real electromagnetic mixer with a maximal value of 1306 °C between the inner electrodes. b) Side view (orthogonal projection) of the real electromagnetic mixer. 1- inlet channel, 2- outer electrode, 3- right inner electrode, 4- left inner electrode, 5- outlet channel.

6.3 Boundary conditions

The boundary conditions applied to the geometrical model of the real electromagnetic mixer are:

- No-slip boundary condition on the electrode and channel walls (velocity vector equal to zero),
- a pressure outlet condition at the surface exit of the outlet channel (pressure equal to zero),
- a mass flow inlet condition of 1440 Kg/d with a temperature of 1300 °C at the surface entrance of the inlet channel,
- an spacial distribution of the electric potential on the inner electrodes of 0 V and 5 V,
- an electric potential of 0 V on the outer electrode and,
- a constant temperature of 1300 °C on the external walls.

6.4 Parametric analysis - Stirring index

It is necessary to carry out a parametric analysis instead of using the optimal values of the dimensionless parameters such as the square modified Hartmann number (Eq. IV.7) and the dimensionless switching frequency (Eq. IV.6) obtained by [19] because the length of the studied model is 4 times the diameter and not 10 times (Eq. IV.2). Also the temperature dependencies of the physical properties of the molten glass influence the mixing process. The numerical results show that the electric current density in the real electromagnetic mixer produce an overheating in the molten glass $<$7 K (Fig. IV.19.a).

Variation of the activation time of the inner electrodes

The activation time of the inner electrodes is varied in the range of 300 s to 800 s. The magnetic flux density is fixed to 100 mT, which gives a ”square modified Hartmann number” $\mathrm{M_{RF}}$ of 860 (Fig. IV.20.a).
The Fig. IV.20.a shows the different values of the stirring index vs the activation time reaching a maximum value of 0.69 at an activation time of 382 s which corresponds to a dimensionless switching frequency $\mathrm{N_{RF}}$ of 16. Therefore the molten glass flows around each inner electrode 8 times as it is seen in the Fig.IV.21.

Variation of the magnetic flux density magnitude $\mathbf{B_{RF}}$

With the activation time fixed at 382 s, the magnitude of the magnetic flux density B_{RF} is varied in the range of 40 mT to 140 mT. The Fig. IV.20.b shows that the stirring index starts to achieve a maximum value of 0.69 in the range of 100 mT to 120 mT after that, it decreases.

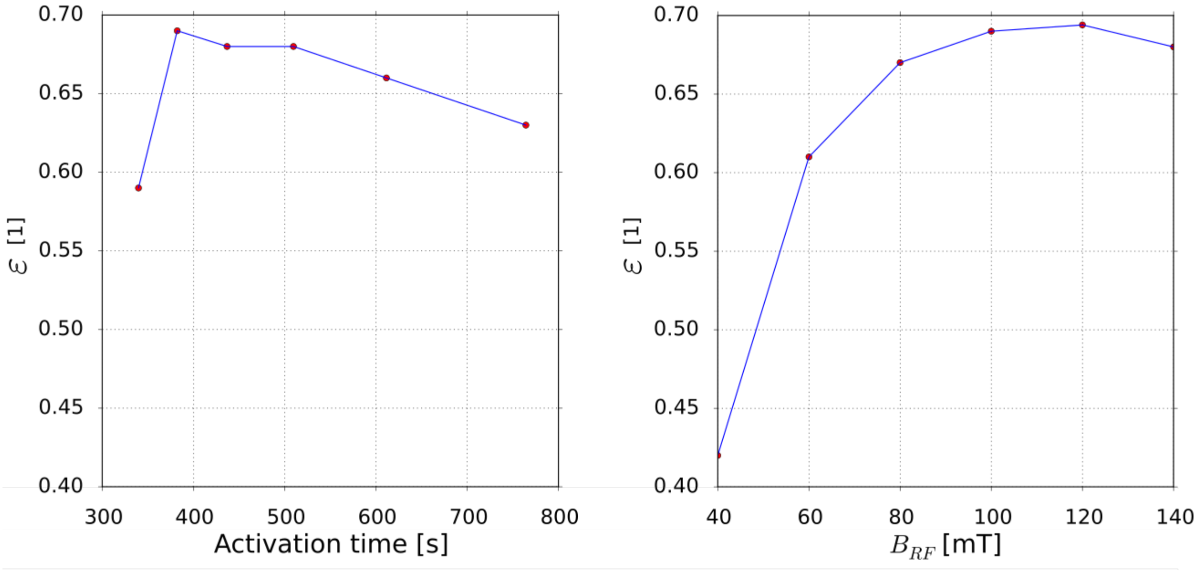

a) b)

Figure IV.20: a) Stirring index vs the activation time applied on the inner electrodes with a maximum value of 0.69 obtained at 382 s for a pull rate of 1440 Kg/d and magnetic flux density of 100 mT. b) Stirring index vs the magnitude of the magnetic flux density obtaining a maximum value of 0.69 between 100 mT and 120 mT for a pull rate of 1440 Kg/d and an activation time of 382 s.

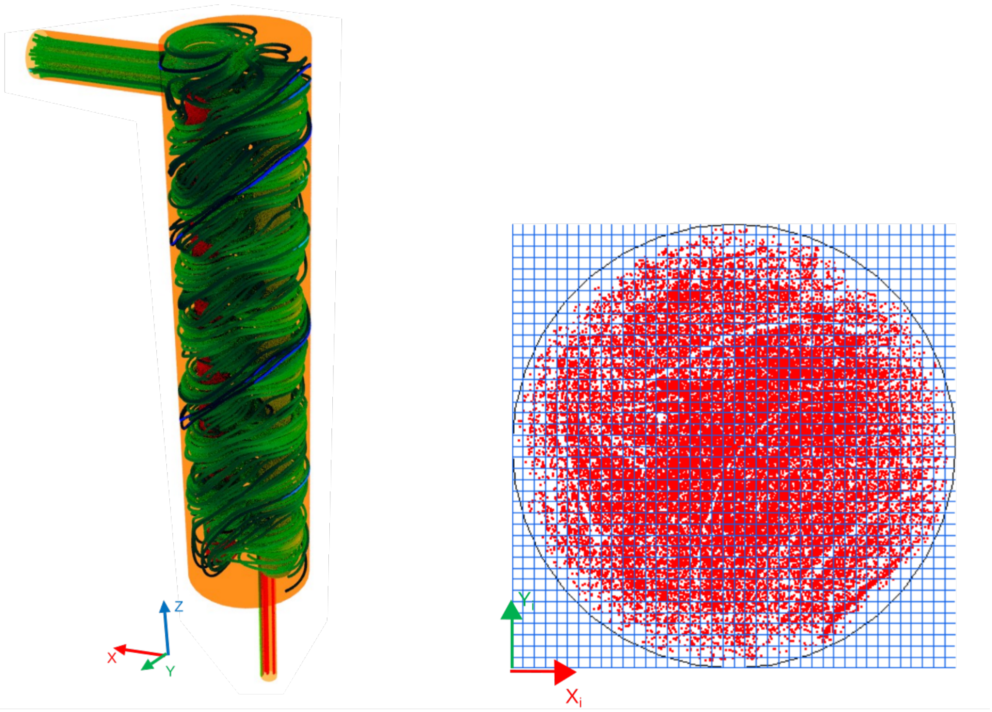

a) b)

Figure IV.21: a) Perspective view of the velocity streamlines for a pull rate of of 1440 Kg/d, a magnetic flux density of 100 mT and an activation time of 382 s. b) Distribution of 50 000 particles in a cross section plane of the outlet channel of the real electromagnetic mixer for a flow rate of 1440 Kg/d, a magnetic flux density of 100 mT and an activation time of 382 s giving an stirring index of 0.69.

7 Conclusions and outlook

7.1 Numerical simulations on the physical model

The previous study made by S. Sugilal Gopalakrisnan [19] showed that the simulation performed in steady mode gives similar results to the simulation in transient mode. Therefore, the periodic activation applied on the inner electrodes could be replaced by an spatial distribution of the electric potential along the inner electrodes.

On the base of the results of the previous study made by S. Sugilal Gopalakrisnan [19], the numerical evaluation of the electromagnetic mixer with periodically activated electrodes is performed with a spatial distribution of the electrical potential along the inner electrodes. Consequently it is possible to create the required simulations in steady mode using the geometrical data of the physical model and the physical properties of the fluid model.
The numerical results show that the electromagnetic mixer can control the laminar flow of the fluid model, turning the flow around the active inner electrode, following the direction of Lorentz force density. Therefore, the Lorentz force density is used to stretch and fold the fluid, necessary conditions to mix a laminar flow.

The mixing grade produced by the generated Lorenz force density is quantified by the stirring index which is computed with the spatial distribution of a group of particles in a cross section plane of the outlet channel. The analysis in a cross section plane is possible to accomplish because the particle trajectories go vertically in the outlet channel due to the laminar nature of the flow.

The potential of the Lorentz force technique is showed comparing its stirring index with that of a highly optimized mechanical stirrer. Despite the similar values of their stirring indexes, the electromagnetic mixer produces a better mixing. This index, being a global index, averages the difference between the number of particles in each box and the optimal number reducing its capabilities to measure local differences in the particle distribution.
The numerical simulations are made in steady mode as a simplification of the more realistic transient mode, because it gives quicker results and an steady streamline that is used later for the computation of the particle trajectories necessary to calculate the stirring index.

The possibility to use an steady mode was validated in the study made by [19] comparing the local stretch ratio parameter (Eq. III.67) of both modes. But this parameter doesn't give any insight about the spatial distribution of the particles, because even if the stirring index has similar values for two distributions, it is possible to say which mixer has better mixing by looking at them.

In further investigations, it will be necessary to do a numerical simulation in transient mode and compare the given spatial distribution of the particles with that computed in steady mode, in order to show that the steady simulation is a valid simplification or it introduces important variations in the particle distribution. Also, it will be necessary to include in the numerical simulation the distribution of the magnetic flux density produced by the coils located along the axis of the physical model to show its effect on the particle distribution.

7.2 Experimental study of the physical model

The numerical simulation must be verified with an experimental study to show that the mathematical model can describe with enough accuracy the reality.

This experimental study is made using a camera-laser system in order to record the laser scattered from the silicon nitride particles of micrometer size injected in the physical model. The laser illuminates a rectangular region of the outlet channel, then a volume region of the channel is scanned moving the camera-laser system step by step.

The intensity distribution of the scattered laser in each recorded picture is used by a self-developed image processing technique to reconstruct the spatial position of the particles. Then, these positions are projected in a cross section plane of the outlet channel and used to compute its stirring index (0.63) which has a close value to the stirring index of the numerical simulation (0.68) but with a different particle distribution.

The particle detection suffers from several limitations (see section 5) allowing to detect only 36% of the expected particles. One important limitation is the calibration of the camera lens focus which is used to obtain an out of focus particle and thus to separate more easily its intensity distribution from the background noise.

The resulting particle distribution in the cross section plane of the outlet channel shows regions with more particles than in others which is a reflect of the region used to calibrate the focus plane of the camera and therefore one of the reasons, that explains the difference between the measured and the simulated particle distribution. Another reason is thermal effects on the wall that was not considered in the simulation. However, this technique is useful to assess by experimental comparison the homogenization of laminar mixing processes.

The diffraction of the scattered laser caused by the cylindrical shape of the outlet channel can be avoided using a rectangular channel which eliminates the necessity to correct the position of the particles using the Snell's law as well as the adjustment of the camera focus plane at each few steps.

The advantage of using an square channel that eliminates the diffraction is to have a fixed focus plane with a constant distance between it and the laser sheet, which will improve the particle detection decreasing the blurring of the particles.

In the future, the intensity of the scattered laser recorded by the camera can be incremented decreasing the laser sheet thickness with an optical system in order to keep its energy. Then, the desired thickness is achieved using a slit which retains some energy. This also allows to illuminate a region with smaller thickness obtaining a better spatial resolution of the particles.

The regulation of the slit thickness can be improved printing a black region in a transparent film using a lithographic technique leaving untouched the region with the desired thickness which acts as a slit.

The methodology of the particle detection can be improved determining first the velocity distribution in the outlet channel using the particle distribution and comparing it with the analytical (pipe channel) and / or numerical results in order to have a stronger validation of the image processing technique.

7.3 Up-scalling to a real mixer

The mathematical model is validated with the stirring index predicted by the numerical simulation which is similar to the stirring index computed experimentally. Therefore, it is possible to up-scale the mathematical model to a real stirring cell using realistic mass flow inlet, wall temperature and temperature dependent physical properties.

The amount of electric current density applied on the electrodes is fixed by the maximum electric current that the electrodes can support [109]. The results show that the maximal possible electric current density in the mixer doesn't produce large overheating in the molten glass ($<$7 K), reducing the impact in the conditioning temperature.

The group of coils used to create the magnetic flux density is located in the insulation region of the mixer in order to avoid perturbations in the refractory material. Also, there is no electromagnetic risk for the surrounding equipment due to the relative low current density and frequency used by the electrodes and coils.

The optimal relation found by [19] between the diameter and length of the electromagnetic mixer is not used because the length was fixed by the maximal length of the currently commercially available electrodes and the diameter by the diameter of a real stirring cell. Therefore, it is performed a new parametric analysis to find the optimal electrode activation and magnetic flux density that give the highest stirring index.

The stirring index corresponding to the real mixer has a lower value than that of the physical model but still competitive with that of the mechanical stirrer. The physical model produces better mixing because it is longer in length than the real mixer promoting a more homogeneous distribution.

CHAPTER V

Project II: High performance forehearth

1 Introduction

In this project is investigated the usability of Lorentz forces in a coloring forehearth of molten glass tanks to improve its performance (see chapter I, section 3.3).

Currently, during the coloring process of the molten glass in the melt zone of the forehearth, it is observed that the minerals (frits) used for the coloring have the tendency to sink contaminating the glass when they sediment. Also, the glass coloring is degraded because the battery of stirrers needs a certain frits level to do a good homogenization.

Lorentz forces can be used to create a push up effect and thus, to prevent the sinking process of the frits as well as to enhance the input flow conditions of the stirring battery, improving the performance of the forehearth.

The results are prepared in the frame of a collaboration between the Technische Universität Ilmenau and FERRO GmbH in Frankfurt.

An start-up project is developed together with FERRO's partner Iittala Glass Factory / Fiskars Corp. Finland on a numerical model to simulate the influence of the Lorentz force in the molten glass flow ($\approx$ 2 t/d) [63]. Then, a second project focused on a larger forehearth ($\approx$ 80 t/d) is developed between the Technische Universität Ilmenau, Ferro France S.A.R.L. and O-I GLASSPACK GmbH & Co. KG Rinteln [64].

This thesis presents only important results from the second project which is focused on the scale-up of the numerical model developed in the first project to study the push up effect created by the Lorentz force.

The first task of the second project is the definition of the geometrical data, the physical properties and the operating parameters of the forehearth as well as the definition of the physical properties of the molten glass used by O-I GLASSPACK. The collected data is used to create the 3D numerical model which is validated with in-situ temperature measurements in the molten glass and on the surface of the forehearth.

The second task is focused on the computation of the electric current density in the molten glass impressed by the electrodes, the magnetic flux density created by the coil system and the resulting Lorentz force density aligned opposite to the molten glass flow (see Fig. V.4).

The electrode and coil arrangements are located in the melt zone where the sinking process of the frits happen. Then, several configurations are analyzed until obtain a push up effect created by the Lorentz force that can overcome the additional negative velocities created by the Joule heating. Depending of the heat transfer within the molten glass, the temperature gradient created by the joule heating can produce strong or weak additional negative velocities.

The third and final task is to make a proposal for the design of the electrode configuration and magnetic system qualified for forehearths with a large width and pull rates. This device and also the method are patented for electromagnetically operated coloration of molten glass in feeder of glass melting plants [66].

2 Description of the forehearth

The O-I forehearth (Fig. V.1) connects the furnace, where the glass is melted, with the forming process, where the glass takes the gob shape. The forehearth is divided in three main zones, the melt zone (Fig. V.1.a), the stirring zone (Fig. V.1.a) and the conditioning zone (Fig. V.1.b). The molten white glass is colored in the melt zone of the forehearth by means of color concentrates (frits). Other possibilities of glass coloring are described in the state of the art (see chapter II, section 2.4).

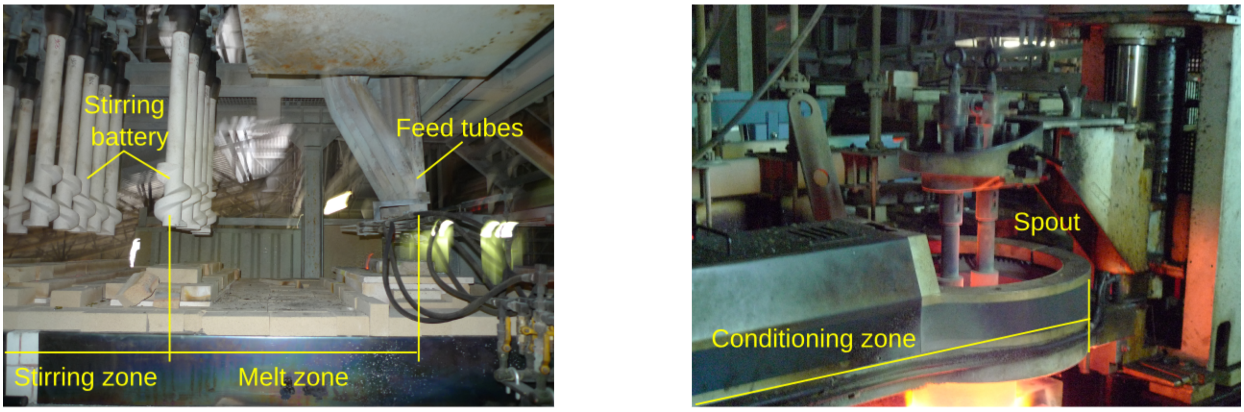

a) b)

Figure V.1: O-I forehearth photos, a) melt zone of the forehearth is defined between the feed tubes and the stirring battery (here: both are lifted out in non-operating state), b) conditioning zone with spout.

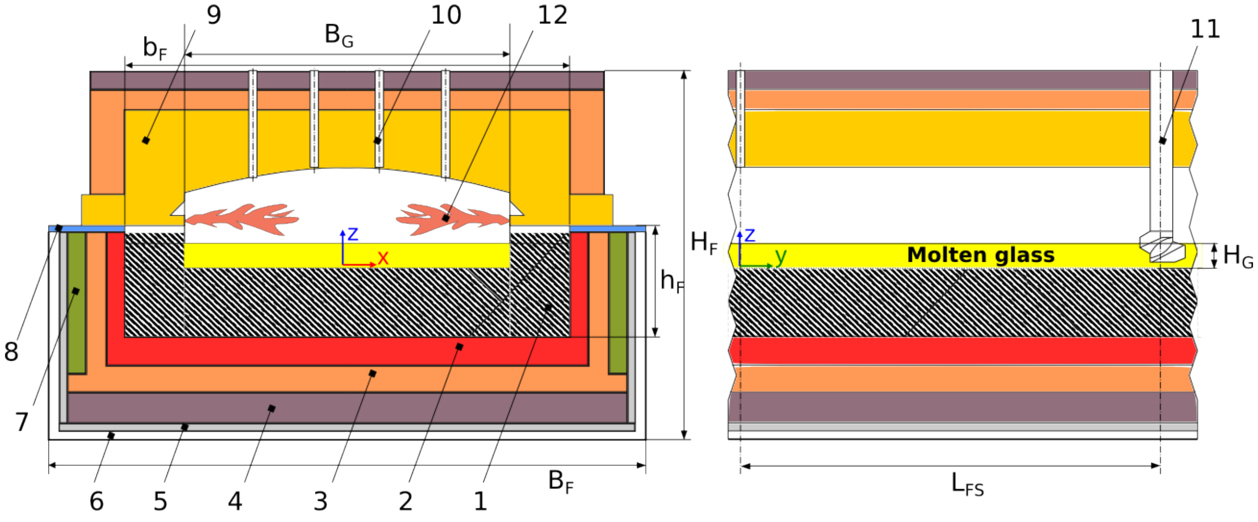

a) b)

Figure V.2: Schematics of the melt zone of the forehearth with the applied materials, a) cross section, b) length section. 1- refractory material type ER1711 RT, 2- insulating material type ZR 55 HA, 3- insulating material type SC 47 LA, 4- insulating material type ISOREF J125 , 5- insulating material type CASI 11, 6- insulating material type Microtherm 260 Kg/m^3, 7- insulating material type RL20-115, 8- insulating material type SC 45 HA, 9- insulating material type ZM 20 AB, 10- four feed tubes, 11 - stirring battery, 12 - flames.

These frits are added to the molten glass through the feed tubes, melting and diffusing progressively, but this diffusion is not enough to homogenize the color, therefore a battery of stirrers (Fig V.1 and Fig. V.2, No. 11) is located at the end of the melt zone.

2.1 Geometrical data and physical properties

The Fig. V.2 shows the schematics of the forehearth melt zone describing the different layers that compose it, with their physical properties showed in the Tab. V.1 and V.2 as well as some important geometrical data showed in the Tab. V.3.

The low value elected for the emissivity of the refractory material (type ER1711 RT, Fig. V.2) takes into account its deterioration (corrosion, mechanical failures) which increases the pore sizes and cracks, whereby heat transfer by radiation can occur, reducing its emission capacity [116].

The heat transfer coefficient of the surrounding atmosphere is adjusted until obtaining predictions on the temperature distributions in the range of the measurement errors (section 3.2).

Table V.1: Physical properties of the used insulating and refractory materials in the forehearth

Parameter	ER 1711 RT	ZR 55 HA	SC 47 LA	ISOREF J125
Bulk density [Kg/dm^3]	4	3.2	0.55	1.23
Specific heat [J/(Kg·K)]	713*	1152*	1152*	1152*
Thermal conductivity [W/(m·K)]	4	0.72* 1000 °C	0.45 1000 °C	0.70 1000 °C
Emissivity [1]	0.2***	-	-	-
Heat transfer coefficient [W/(m^{2}K)]	-	-	20****	20****

* Data from the start-up project [63], ** same as SC 47 LA, *** see [116],**** see section 3.2

2.2 Physical properties of the white glass

The thermal conductivity [17], [117], the specific heat [17], [117], the emissivity [118], and the refraction index [119] are taken from the literature and later tuned with the temperature measurements on the forehearth. The density, viscosity and electrical conductivity of the molten glass are considered dependent on the temperature. The dependency of the density is equal to the DGG standard soda lime glass Ia, the dependency of the viscosity is self-measured with a rotational viscometer VIS 403/ NETZSCH at the TU Ilmenau and the dependency of the electrical conductivity was measured by JSJ Jodeit GmbH in Jena-Maua. The measured temperature dependencies are approximated on the basis of the known physical behavior (see Tab. V.4).

Table V.2: Physical properties of the used insulating materials in the forehearth

Parameter	CASI 11	Micro therm	RL 20 115	SC 45 HA	ZM 20 AB
Bulk density [Kg/dm^3]	2.5	0.26	0.55**	2	2.95
Specific heat [J/(Kg·K)]	1152*	1152*	1152*	1152*	713*
Thermal conductivity [W/(m·K)]	0.11 400 °C	0.029 400 °C	0.45**	0.45*	2.04 1000 °C
Emissivity [1]	-	-	-	-	-
Heat transfer coefficient [W/(m^{2}K)]	-	20****	-	20****	20****

* Data from the start-up project [63], ** same as SC 47 LA, *** see [116], **** see section 3.1

Table V.3: Geometrical data of the O-I forehearth

Parameter	Value
Glass melt level H_G [mm]	165
Glass melt width B_G [mm]	1092
Distance between the feed tube and the stirring battery L_{FS} [mm]	1549
Refractory width b_F [mm]	1492
Refractory height h_F [mm]	378
Forehearth width B_F [mm]	2000
Forehearth height H_F [mm]	1324
Feed tube diameter [mm]	45-50
Feed tube separation distance [mm]	200

Table V.4: Physical properties of the molten glass

Parameter	Value / temperature dependencies in °C
Density [kg/m^3]	$\rho_G(T_G) = 2508.43 - 0.15T$
Dynamic viscosity [Pas]	$\lg(\eta_G(T_G)) = -4.10 + 7213.38T^{-1}$
Electric conductivity [S/m]	$\lg(\sigma_G(T_G)) = 3.55 - 2863.26T^{-1}$
Specific heat [J/(Kg·K)]	$Cp_G = 1285$
Thermal conductivity [W/(K·m)]	$\lambda_G = 0.1\text{-}2$
Emissivity [1]	$\varepsilon_G = 0.8$
Refraction index [1]	$n_G = 1.2\text{-}2.2$

2.3 Temperature measurements

The temperatures in the molten glass are measured with a platinum rhodium thermocouple sensor which is introduced into a quartz glass tube to protect it from the contact with the molten glass which is around 1200 °C. The signal is acquired by the meter VOLTCRAFT ® 306 data logger thermometer with an estimated global measurement error of ± 5 °C.

The measurements are made in two positions of the molten glass and on the surface of the forehearth (Fig. V.1.a). First under the feed tubes and the second under the stirring battery where it is only possible to open the top surface of the forehearth removing few bricks (Fig. V.1.a).

However, the temperature measurements in the molten glass could only be realized when the feed tubes as well as the stirring battery are not in operating state (Fig. V.1.a) and green glass is running in the melt zone of the forehearth.

The Fig. V.3.a shows the measured temperatures in the molten glass in the middle (0, 0, z) mm and side (420, 0, z) mm of the feed tube position (Fig. V.2.a) called the inlet, as well as in the middle (0, 1549, z) mm and side (420, 1549, z) mm of the first line of the stirring battery (Fig. V.2.b) called the outlet. Unfortunately, the measurement in the middle of the outlet is corrupted (burning of the cable isolation due to the contact with the hot surface of the forehearth). The Fig. V.3.b shows the linear interpolation of the measured temperatures on the inlet that is used as boundary condition of the 3D numerical model.

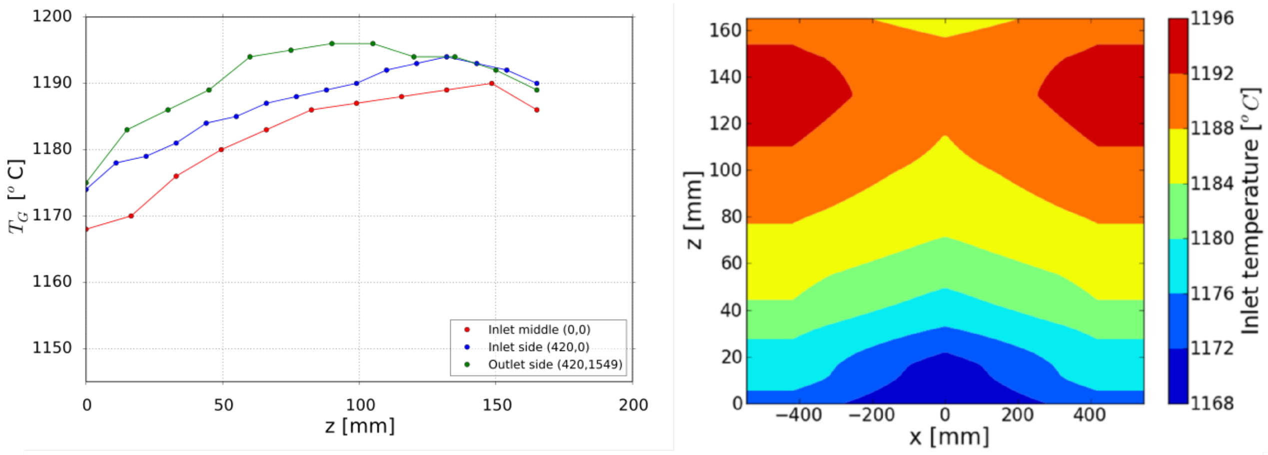

a) b)

Figure V.3: Measured temperatures on the inlet (red and blue dots) and outlet (green and black dots) of the molten green glass in the non-operating state of the feed tubes and the stirring battery. b) Linear interpolation of the measured temperature distribution on the surface of the inlet of the molten green glass.

2.4 Operating parameters

The operating parameters used in the study are those obtained when the temperature measurements were performed (Tab. V.5). The natural gas flow rate goes through 16 burners in each side of the forehearth but only 12 are in the melt zone, therefore this number is used to compute the total thermal power (Tab. V.6).

The total thermal power P_G,

$$P_G = \dot{m}_G C p_G T_G = 1.35\,MW \tag{V.1}$$

introduced in the forehearth is about 1.35 MW computed with the specific heat Cp_G of the molten glass (Tab. V.4), its pull rate $\dot{m}_G$ (V.5) and a mean typical inlet temperature T_G = 1200 °C. A part of this power is loss through:

- the molten glass surface mainly by radiation,
- the walls of the refractory material by conduction and radiation,
- insulation materials by conduction and
- through the forehearth surface by convention.

Therefore the forehearth has a burner system which produces a power P_B about 38 KW to compensate these losses (Tab. V.6),

$$P_B = \varphi_{NG} \gamma_{NG} \dot{m}_{NG} N_B = 38\,kW \tag{V.2}$$

where φ_{NG} is the energy density of natural gas, γ_{NG} is the thermal efficiency, $\dot{m}_{NG}$ is the natural gas flow and N_B is the number of burners.

Table V.5: Operating parameters at the moment of the temperature measurements

Glass pull rate $\dot{m}_G$ [t/d]	Mean velocity U_G [mm/s]	Glass type	Glass level H_G [mm]	Gas flow rate [Nm^3/h]
78.7	1.5	Green glass	165	7.4

Table V.6: Operation parameters of the burners

Energy density of natural gas φ_{NG} [MJ/Nm^3]	Thermal efficiency γ_{NG} [1]	Gas flow $\dot{m}_{NG}$ [Nm^3/h]	Burner numbers N_B [1]	Power P_B [kW]
35.6	0.7*	7.4	24	38

* See [115]

3 Numerical Simulations

The numerical simulations are performed with the commercial computational fluid dynamics software ANSYS/ FLUENT v.13 using a non-conformal mesh, elaborated with the commercial software Gambit v.2.4. This type of mesh, where the grid nodes don't match along the interfaces, is used to isolate the different requirements of mesh resolution; more in the molten glass and in the atmosphere and less in the refractory and in the insulating materials (Fig. V.4.b). The geometrical model is made of an hexahedral mesh because it has better orthogonality respect to the walls and to the direction of the flow giving more accurate results than, e.g. a tetrahedral mesh. The resulting mesh gives 1 398 275 cells.

Initially, the numerical simulations of the velocity and temperature distributions are made without the electrodes, in order to validate the model with the temperature measurements. The heat transfer by radiation (Eq. III.31) between the crown (walls surrounding the atmosphere), the flames and the molten glass surface as well as the radiation inside the molten glass is made with the discrete ordinates radiation model [122] whose heat flux is included into the energy equation (Eq. III.32). Then, the distribution of the electric current density, the magnetic flux density and the Lorentz force density are computed using the user define functions (UDF) of Fluent and then loaded dynamically by this solver (see chapter III, section 4.1).

After obtaining a steady and well converged simulation, the selected frits trajectories in the molten glass flow are modeled with the trajectories of passive particles computed with the discrete phase model using the Runge-Kutta method [2].

Two types of electrode and coil configurations are analyzed numerically to obtain a large push up effect created by the Lorentz force density, although additional negative vertical velocities happened due to the Joule heating [64]. One of the configuration is made of two electrodes and one coil and the other configuration of three electrodes and two coils energizing them with single-phase alternating current (50 Hz). The last configuration is retained (Fig. V.4.a) because the former didn't produce enough push up effect close to the center of the molten glass channel.

3.1 Boundary conditions

The boundary conditions applied to the geometrical model are:

- No-slip condition on the electrodes and channel walls (velocity vector equal to zero).
- A pressure outlet on the surface of the outlet channel (pressure equal to zero).
- A fixed temperature inlet distribution equal to the temperature measurements (Fig. V.3)
- A mass flow inlet of 78.7 t/d on the surface entrance of the inlet channel.
- An electric potential of 0 V on the middle electrode and of 20 V on the side electrodes.

- A convective heat flux on the forehearth surface with a variable heat transfer coefficient.

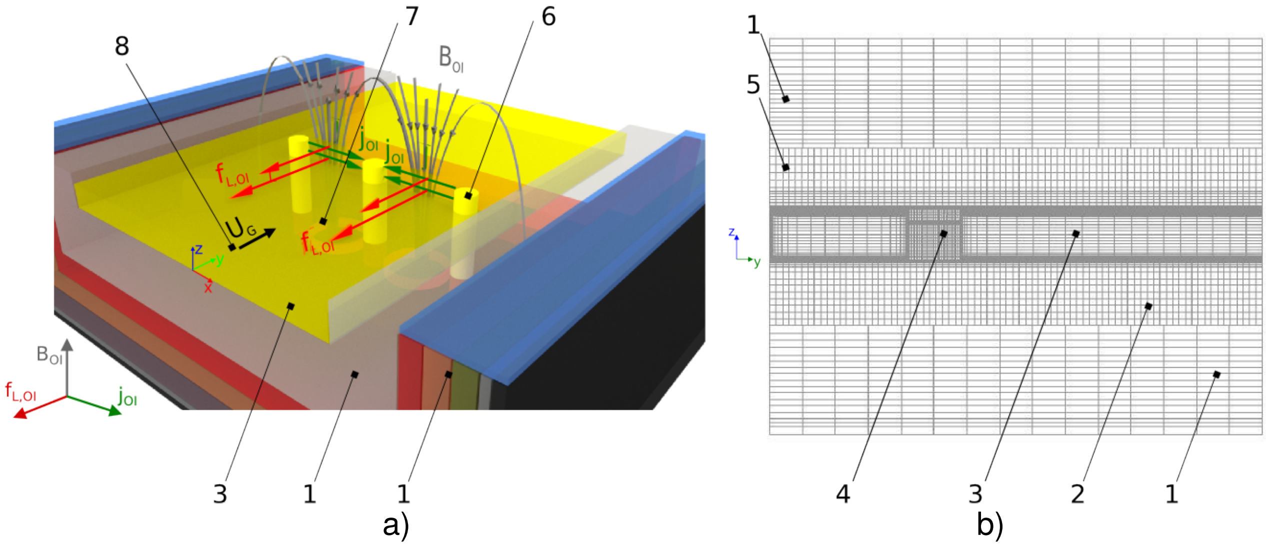

Figure V.4: a) Schematic of the melt zone of the forehearth containing the electrode and coil arrangements used to generate the Lorentz force density. b) Length section of the non-conformal hexahedral mesh containing 1 398 275 cells. 1- insulation material zone, 2- the refractory material zone, 3- molten glass zone, 4- the electrode zones, 5- the atmosphere zone, 6- electrodes, 7- coils located in the insulating material, 8- direction of the molten glass flow.

The velocity distributions of the molten glass flow in the forehearth are well developed, but the truncation of the geometry to make the numerical analysis in the melt zone requires the definition of inlet and outlet boundary conditions. The boundary condition for the velocity which is equal to the mass flow of the molten glass (Tab. V.5) gives a velocity distribution with only one component parallel to the y-axis and to the direction of the molten glass flow. Therefore, the velocity distribution at the outlet is used as a boundary condition of the inlet several times, until obtaining an stable distribution along the forehearth.

3.2 Temperature distributions and validations with measurements

In order to have a realistic representation of the push up effect created by the Lorentz force, it is necessary to compute with enough accuracy the temperature distribution in the molten glass and forehearth as well as the velocity distribution of the molten glass flow.

The numerical model predicts total heat loss of 37.5 KW, which is the heat transfer rate difference between the outlet and the inlet of the molten glass channel (see Eq. V.1). The loss is compensated by the burner flames included into the model as a normal temperature distribution which is tuned to obtain a stable distribution of the temperature along the forehearth.

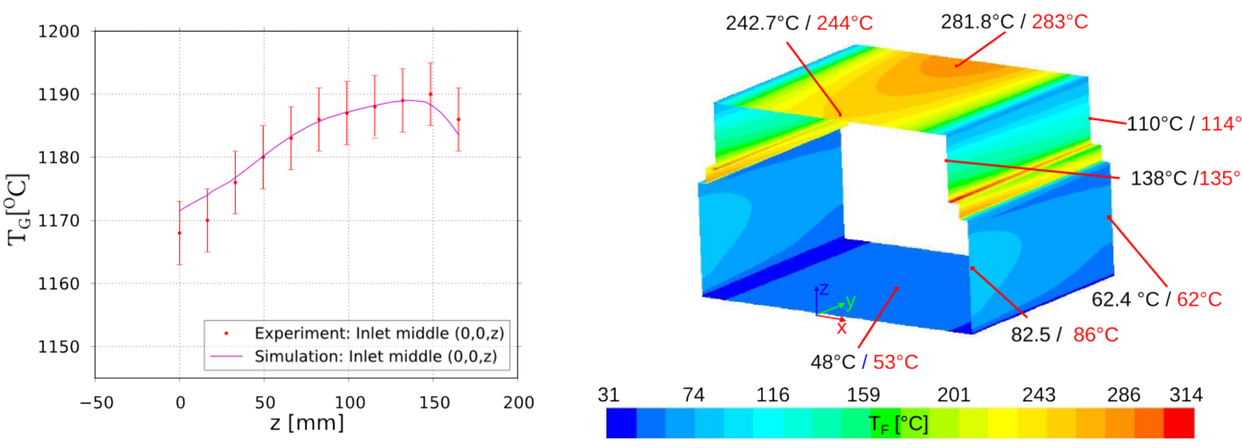

a) b)

Figure V.5: a) Measured (dots with the error range of ± 5 °C) and simulated (line) temperature distribution inside the molten glass along the z-axis of the forehearth at the middle of the inlet (0, 0, z) mm. b) Computation of the temperature in each face of the forehearth surface (red color) and temperature measurements in each face (black color).

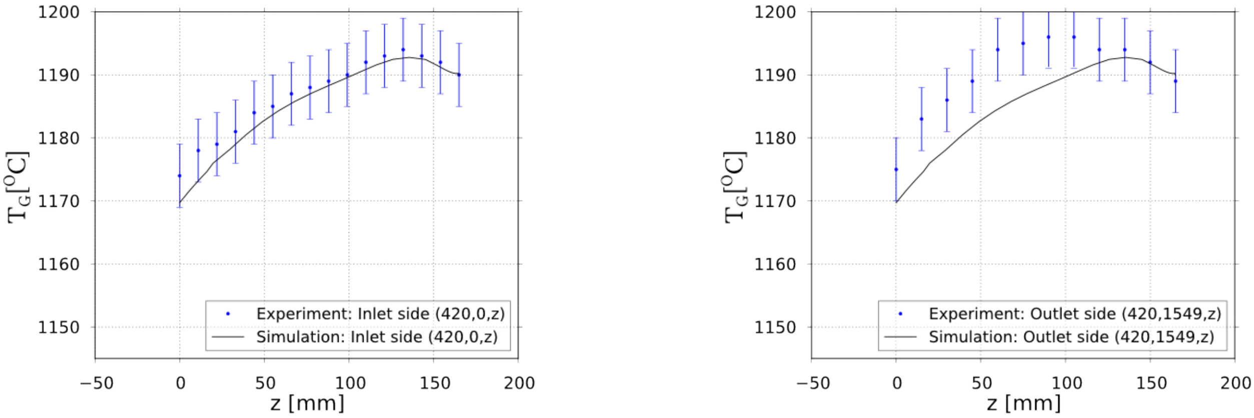

a) b)

Figure V.6: Measured (dots with the error range of ± 5 °C) and simulated (line) temperature distribution inside the molten glass along the z-axis of the forehearth a) at the inlet side (420, 0, z) mm and b) at the outlet side (420, 1549, z) mm.

The comparison of the simulated temperature distributions on the forehearth surface as well as in the molten glass with the measured temperatures are shown in the Fig. V.5 and Fig. V.6. The deviations are less than ± 5 °C which are in the range of the measurement error. Only the simulated temperature distribution in the molten glass on the middle region of the outlet is underestimated (approx. 10 K) (Fig. V.6.b). To tune the measured surface temperatures on the forehearth with the calculated temperatures, the heat transfer coefficient has a linear variation over it with a mean value of 20 W/(m^2K).

3.3 Coil and electrode arrangements

After the sufficient validation of the temperature distribution predicted by the 3D numerical model with in-situ temperature measurements (O-I GLASSPACK GmbH & Co. KG), it is possible to evaluate different electrode and coil configurations. This evaluation is carried out to obtain the desirable push up effect created by the Lorentz force in the molten glass in order to prevent the sinking process of the frits, although additional negative vertical velocities took place due to the Joule heating [64].

O-I GLASSPACK uses 4 feed tubes (Fig. V.1.a and V.2.a) with an ending diameter between 45-50 mm and with a distance between them of 200 mm. Therefore the electrode arrangements must cover a total width of 700 mm using a height $h_{\mathrm{OI,\,E}}$ equal to 3/4 of the molten glass height H_G = 124 mm (Fig. V.2.a).

First, it is studied an arrangement of two molybdenum electrodes and one water cooled coil producing a Lorentz force density with a magnitude of 7 N/m^3 in the middle of the molten glass channel and 17 N/m^3 near the electrodes [64]. But, the Joule heating created by the impressed electric current density in the molten glass is more important than the push up effect made by the Lorentz force density. As a result, negative velocities are developed in the middle of the channel obtaining a final frits level lower than configuration without electrodes. To overcome this problem, a third electrode is added in the middle of the channel to cover the width of the forehearth and the coil is replaced by two smaller coils.

In this configuration, the middle electrode has bigger diameter $D_{\mathrm{OI,\,E}}$ = 80 mm than the side electrodes $D_{\mathrm{OI,\,E}}$ = 60 mm in order to limit the electric current density on its surface under the maximum admissible value of 2 A/cm^2 [48]. Also, the Joule heating density around the middle electrode is reduced and thus the temperature gradients (Fig. V.8.c) which are responsible of the additional negative velocities (Fig. V.8.b).

Table V.7: Physical properties of the molybdenum electrodes [48]

Density [Kg/m^3]	Thermal conductivity [W/(m·K)]	Heat capacity [J/(Kg·K)]	Electrical conductivity [S/m]	Emissivity [1]
10220	113 (1000 °C)	303 (1000 °C)	3.17×10^6	0.16 (1000 °C)

For such electrode system, two water cooled copper coils with an external diameter $D_{\mathrm{OI,\,C}}$ = 200 mm, an internal diameter $d_{\mathrm{OI,\,C}}$ = 140 mm, a height $h_{\mathrm{OI,\,C}}$ = 40 mm and a winding $w_{\mathrm{OI,\,C}}$ = 20 turns is selected (Fig. V.9).

The coil arrangements is located in the insulating material 200 mm from the bottom of the molten glass to avoid perturbations in the refractory material (Fig. V.9). But, in this study the effects of the coil temperature in the insulating material is not taken into account.

In order to obtain the Lorentz force density $\mathbf{f_{L,OI}}$ aligned opposite to the molten glass flow over the total cross section (Fig. V.7.c and V.7.d), the electric current on the electrodes flows from the left and from the right electrode to the middle electrode. The amount of the total electric current is $I_{OI,E}$ = 217 A (Fig. V.7.a) using a voltage of $V_{OI,E}$ = 20 V. The electric current on each coil is $I_{OI,C}$ = 1500 A, flowing in clockwise direction in the right coil and in opposite direction in the left coil to obtain a magnetic flux density $\mathbf{B_{OI}}$ that circulates around the middle electrode (Fig. V.7.b). In the real situation in which AC currents are used, this is possible by phase inversion.

The magnetic flux density $\mathbf{B_{OI}}$ has a maximum value of $\approx$ 20 mT close to the bottom of the molten glass channel (Fig. V.7.b). Between the electrodes, the electric current density $\mathbf{J_{OI}}$ has a mean value of 600 A/m^2, which increases up to $\approx$ 4000 A/m^2 near the electrodes (Fig. V.7.a). The resulting $\mathbf{f_{L,OI}}$ has values between 7 and 13 N/m^3 between the electrodes, which increases up to $\approx$ 50 N/m^3 near the bottom of the electrodes (Fig. V.7.c and V.7.d).

Near the side electrodes, the temperature is about 1187 °C, but near the middle electrode, it increases up to 10 K. The electric current density in the surface of the middle electrode is about 4000 A/m^2, but only the part of surface of the side electrodes opposite to the middle electrode has a value about 4000 A/m^2 the rest has a value about 2000 A/m^2. Moreover, the side electrodes are close to the wall of the channel where the heat transfer is more intense.

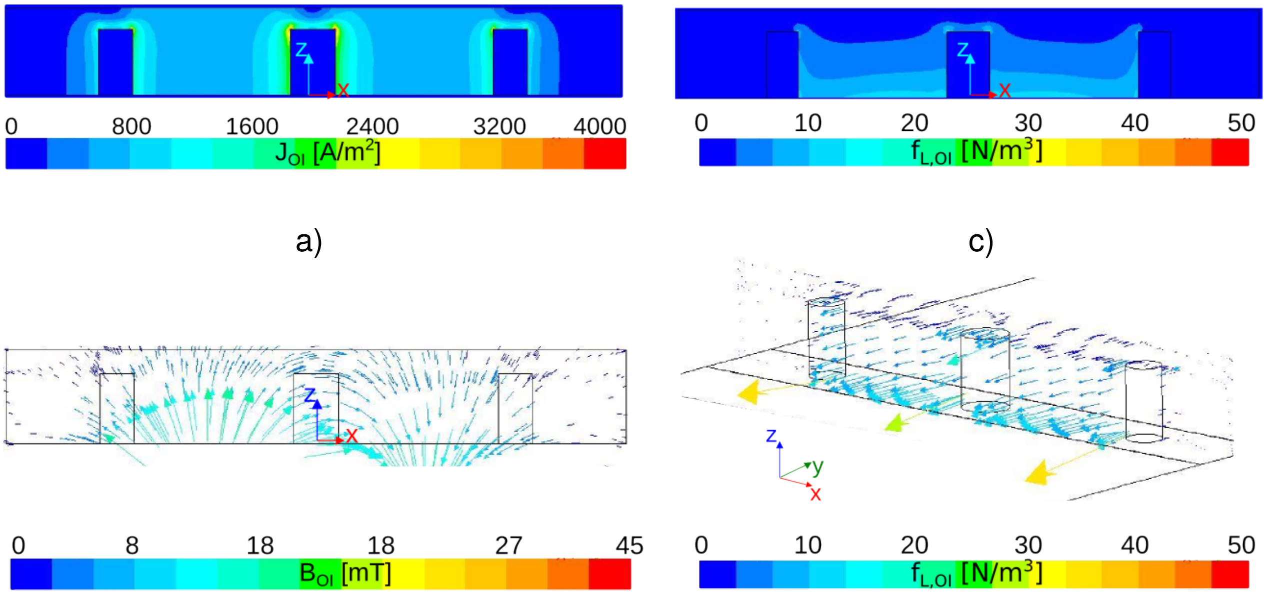

a) c)

b) d)

Figure V.7: Electric current density, magnetic flux density and Lorentz force density distribution in a cross section plane (x, 775, z) mm. a) Distribution of the electric current density magnitude J_{OI}. b) Vector field of the magnetic flux density $\mathbf{B_{OI}}$ colored by its magnitude. c) Distribution of the Lorentz force density magnitude $f_{L,OI}$. d) Vector field of the Lorentz force density $\mathbf{f_{L,OI}}$ colored by its magnitude.

Without electrodes, exist already negative velocities located close to the sides of the molten glass channel. This happens because, the heat transfer by radiation is more intense close to the sides due to the location of the burners. Therefore, the temperature at the surface of the molten glass is higher on the sides than on the center, but the temperature in the middle of the molten glass is higher than at the top center (Fig. V.8.c). These gradients of temperature are the responsible of the convection cells close to the sides, but their velocities are several times lower than the pull rate (0.03 mm/s $<<$ 1.5 mm).

Then, when the electrodes are added and are in operation mode, additional negative velocities (convection cells) appear near the middle electrode due to the additional temperature gradients and the venturi effect.

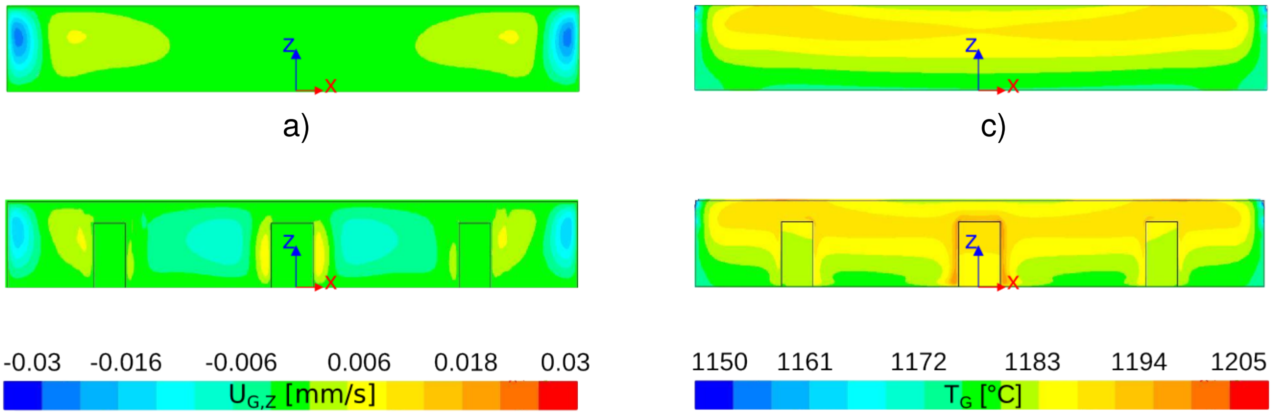

a) c)

b) d)

Figure V.8: Temperature and velocity distribution in a cross section plane (x, 775, z) mm. a) Distribution of the velocity component $U_{G,Z}$ without the electrodes. b) Distribution of the velocity component $U_{G,Z}$ with the electrodes. c) Distribution of the temperature T_G without the electrodes. d) Distribution of the temperature T_G with the electrodes.

3.4 Push up effect

The trajectories of the frits in the molten glass are modeled with passive particles with initial positions equal to the positions of the right feed tubes, due to the symmetry of the forehearth. Therefore, the initial positions of the particles in the molten glass are (100, 0, 82) mm and (300, 0, 82) mm (Fig. V.2).

The Fig. V.10.a shows that the trajectory with initial position at (300, 0, 82) mm close to the side electrode has a final level (y = 1500 mm, corresponding with the end of the melt zone / with the input range of the stirring battery) higher than the configuration without electrodes approx. 1 mm. Close to this electrode, positive vertical velocities are developed (Fig. V.8.b) due to the push up made by the Lorentz force density (Fig. V.7.d). But the trajectory with initial position at (100,0,82), close to the middle electrode, has a final level lower than the configuration without electrodes almost 3 mm. The molten glass temperature close to this electrode is higher than the side electrodes , negatives velocities are developed (Fig. V.8.b) due to the Joule heating, which is more important around the middle electrode than the push up made by the Lorentz force density.

To overcome this problem, the feed tubes located at x = -100 mm and x = 100 mm are replaced by one feed tube located at x = 0 mm (Fig. V.9.a) because in the region close to the middle electrode the positive vertical velocities are stronger (Fig. V.8.b).

In this case, the trajectories with initial position at (0, 0, 82) mm, (40, 0, 82) mm and (300, 0, 82) mm have a final level higher than the configuration without electrodes almost 20 mm, 2 mm and 1 mm respectively (Fig. V.10.b) when the electrodes and coils are located in the middle of the melt zone, $L_{OI,E} = L_{OI,C} = 775$ mm.

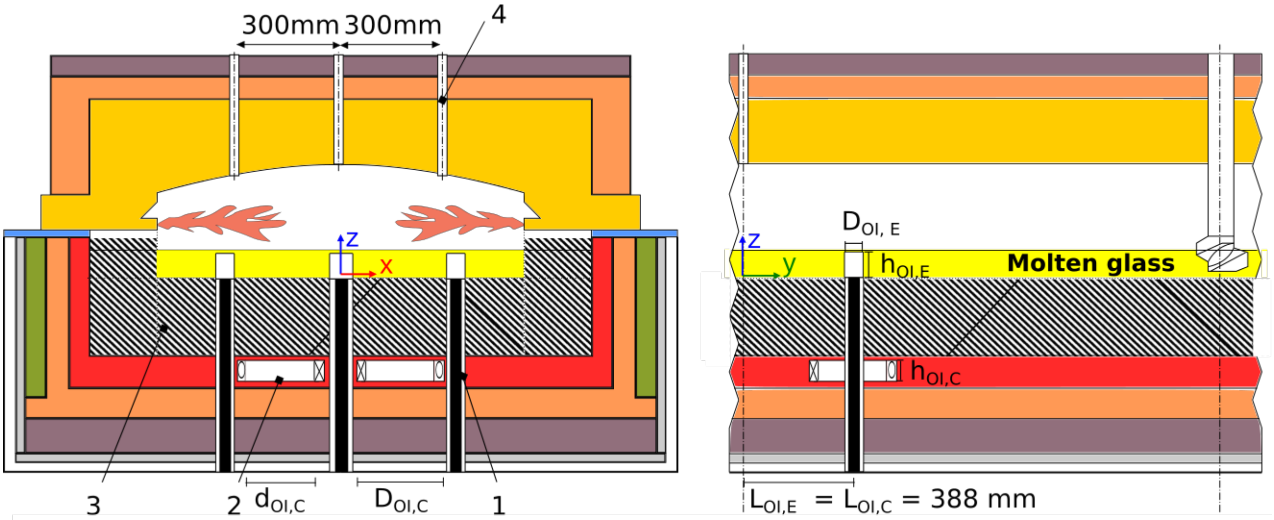

a) b)

Figure V.9: Schematics of the melt zone of the forehearth with the new distribution of the feed tubes and the electrode and coil arrangements. a) Cross section. b) length section. 1- arrangement of three molybdenum electrodes, 2- arrangement of two water cooled copper coils, 3- refractory material, 4- feed tubes.

Due to the positive slope of the trajectories (Fig. V.10), it is possible to increase their final levels locating the electrodes and coils closer to the feed tube ($L_{OI,E} = L_{OI,C} = 388$ mm, Fig. V.9.b). It is found that the final levels are increased up to 25 mm, 3 mm and 2 mm from the initial positions of (0,0,82) mm, (40, 0, 82) mm and (300, 0, 82) mm respectively (Fig. V.11.a and V.11.b).

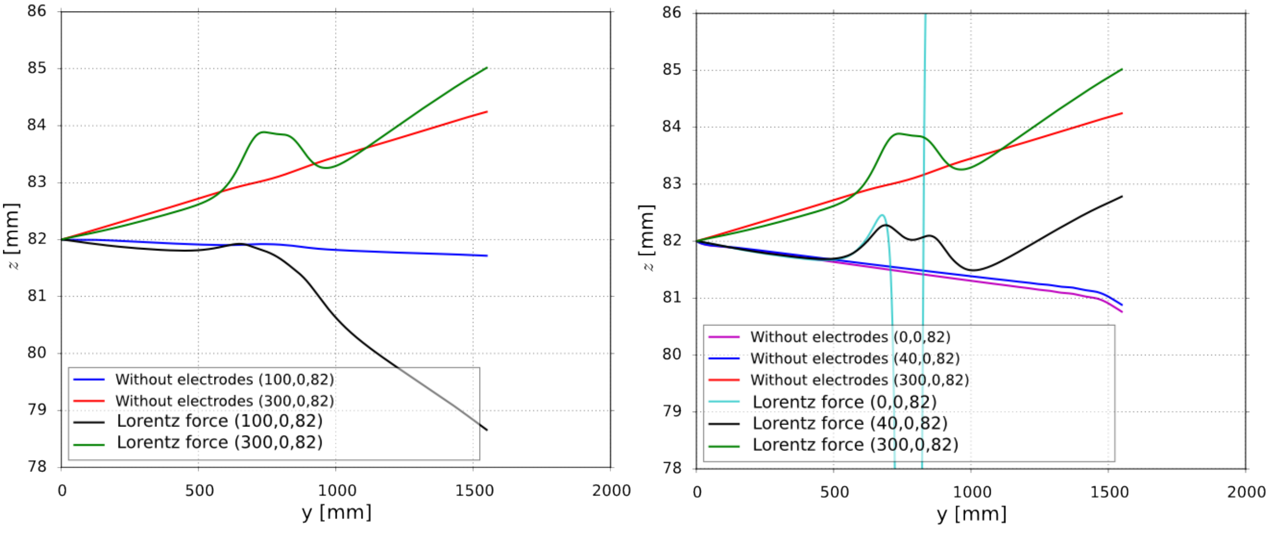

a) b)

Figure V.10: Particle trajectories with $I_{OI,\,E}$ = 217 A, $I_{OI,\,C}$ = 1500 A and with the electrode and coil arrangements located at y = 775 mm ($L_{OI,\,E}$ = $L_{OI,\,C}$ = 775 mm). a) Trajectories with initial positions located at (100,0,82) mm and (300,0,82) mm. b) Trajectories with initial positions located at (0, 0, 82) mm, (40, 0, 82) mm and (300, 0, 82) mm.

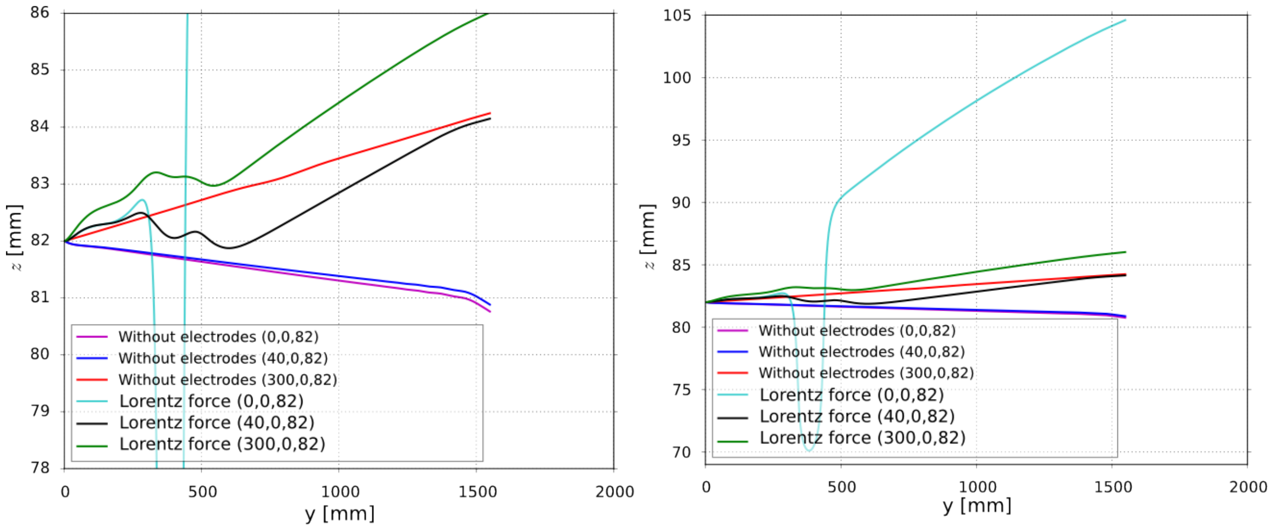

a) b)

Figure V.11: Trajectories with initial positions located at (0,0,82) mm, (40,0,82) mm and (300,0,82) mm using $I_{OI,\,E}$ = 217 A and $I_{OI,\,C}$ = 1500 A as well as with the electrode and coil arrangements located at y = 388 mm ($L_{OI,\,E}$ = $L_{OI,\,C}$ = 388 mm). a) Plot of the trajectories in a range of 78 - 86 mm for the z-axis. b) Plot of the trajectories in a range of 70 - 105 mm for the z-axis to show the final level of the trajectory with initial position at (0,0,82) mm.

4 Conclusions

The investigations show that on the basis of a verified numerical 3D model which includes the boundary conditions, process parameters and temperature dependent material properties, it is possible to obtain a sufficiently accurate temperature distribution within the errors of ± 5 K on the surface of the forehearth as well as in the molten glass. Only the calculated temperatures on the side of the outlet are in the range of ± 10 K due to the simplification made on the optical properties of the molten glass, considered independent of temperature and wavelength.

The molten glass must be considered as semi-transparent with its optical properties depending on the temperature. However, the temperature dependent absorption and emission coefficients were not known.

In order to cover the large width of the O-I forehearth, it is necessary to implement an arrangement of three electrodes and two opposite connected coils to obtain enough push up effect over the total cross section. But, the heat transfer in the green glass together with the large dimensions of the O-I forehearth and the Joule heating increase the convection in the molten glass, and thereby generates additional negative vertical velocities reducing the push up effect created by the Lorentz forces.

The effect of the Lorentz force density on the molten glass flow is increased by using an electrode with a larger diameter in the middle, than in the sides. Then, to use the regions where the push up effect created by the Lorentz force density is more important than the Joule heating, avoiding the additional negative velocities, the two inner feed tubes are replaced by one feed tube located in the middle of the forehearth. As a result, the corresponding trajectories go closer to the middle electrode than before, resulting in a higher final level of them at the outlet of the molten glass.

The trajectories of passive particles with initial positions at (0, 0, 82) mm, (40, 0, 82) mm and (300,0,82) mm have final levels higher than the configuration without electrodes almost 25 mm, 3 mm and 2 mm respectively.

It is expected that the push up effect in white glass will be stronger than in green glass using the same electric currents I_E and I_C because:

- The Joule heating will have a lower impact in white glass than in green glass due to the better internal heat transfer.
- Consequently, the bottom temperature of white glass will be several degrees higher than green glass reducing the temperature gradient from $\approx$ 20 K (Fig. V.5.a and V.6) to 10 K (data provided by O-I GLASSPACK GmbH & Co. KG). Also the mean working

temperature will increase from 1183 °C (Fig. V.5.a and V.6) to 1219 °C (data provided by O-I GLASSPACK GmbH & Co. KG).

- Therefore, assuming that the physical properties of white glass follow the same behavior of the green glass (Tab. V.4), its density and viscosity are respectively 0.2 % and 31% lower than green glass, and its electrical conductivity 16 % higher than green glass for the temperature mentioned above.
- With these values the Lorentz force density will be higher than 20 N/m^3 (Fig. V.7.c) with an enhanced push up effect close to the bottom of the white glass.

The push up effect generated by the Lorentz force density in white glass must be evaluated with a numerical study due to the strong non-linear coupling between the hydrodynamic, heat transport and electromagnetic fields. Also, it must evaluate the appropriate configuration of the electrode arrangements and magnetic system. This numerical study has to be based on a verified model.

5 Outlook

In a further study, the influence of the temperature dependent optical properties of the molten glass must be included into the mathematical model to analyze its influence in the heat transfer and thus in the temperature distribution within the molten glass.
Also, the burner flames must be modeled to evaluate its impact on the heat transfer. Therefore, when the electrodes are in active mode, the thermal power added by Joule heating can be compensated regulating the gas flow of the burners (Tab. V.6).

The frits, modeled in this study as passive particles, follow the streamlines of the molten glass flow, but cannot model the sinking process due to the gravity. In order to take into account this process, the frits could be modeled as a fluid (second continuous phase), with an initial higher density than the molten glass (main continuous phase) due to its initial lower temperature. Also, this multiphase flow accounts for the diffusion of the secondary phase within the main phase. Additionally, the diffusion of ions in the molten glass due to the melting and dissolution of the frits during its residence in the molten glass must be considered.
The push up effect generated by the Lorentz force density not only prevent the sinking of the frits, but also can be used to give the necessary level that the battery of stirrers needs to produce a good homogenization of the molten frits within the molten glass.

The evaluation of the homogenization quality related to different final levels of the frits at the end of the melt zone, needs to include the battery of stirrers into the geometrical model. The motion of the stirrers can be modeled with the multiple reference frame model or the sliding mesh model [2]. Later, the Lorentz force density can be evaluated as a replacement of the stirring battery in the same spirit as in the study of the Electromagnetic mixer (see chapter IV).

CHAPTER VI

Project III: Electromagnetic crystallizer

1 Introduction

This project is focused on the study of a new technique, the Lorentz force technique, as replacement of the mechanical stirrer used currently in the chemical industry for the mixing of inorganic solutions during the crystallization process (see chapter I section 3.4). The current technique has some limitations such as:

- the flow is generated by means of shear stresses around the stirrer impellers, limiting the mixing in the whole volume of the crystallizer,
- increasing the power could help the mixing but also may break the crystals reducing its size,
- the wear of the stirrer can contaminate the solution and the reaction products.

Electromagnetic forces called Lorentz forces can be used to overcome these limitations exploiting the electrical conductivity of the solutions due to its electrolytic nature.

The Lorentz force is created with an arrangement of two electrodes impressing an electric current density in the fluid and an external arrangement of three coils, with its magnetic field penetrating the solution.

Unlike the shear stresses produced by the mechanical stirrer, the Lorentz force spreads in the whole volume having a better impact on the homogenization, but also it is not exempt of limitations. The impressed electric current density is limited by the water content on the chemical solution, because the redox reaction of water must be avoided. Also, the magnetic field must be created with a simple arrangement of coils, limiting the magnitude of this field. Additionally, the electric current density causes a heating of the solution which can influence the crystallization.

The first task of this study is the analysis and validation of the velocity distribution by means of numerical simulations performed with the commercial software ANSYS / Fluent v. 13. The fluid flow is analyzed in laminar and turbulent regime which is determined by the magnitude of the Lorentz force.

In laminar regime, the numerical results are validated with an analytical solution. In turbulent regime, the RANS turbulence models chosen to study the mean velocity distribution are validated with the more accurate Large Eddy Simulation (LES).

The second task is to select from the RANS models the one that shows the best agreement with the LES results. The velocity distributions predicted by the selected RANS model is used to compute the trajectories of passive particles and thus to quantify the mixing capabilities of the Lorentz force.

The third and final task of the study is the design of the physical model to validate in a further study the numerical results.

2 Description of the crystallizer physical model

The physical model of the crystallizer has an annular shape and it is made of an outer and inner metallic cylinder acting as electrodes. Also, it has two circular insulators made of plexiglas (PMMA-Polymethyl methacrylate) located on the top and bottom, and an external coil system which creates an axial homogeneous magnetic field in the whole crystallizer.

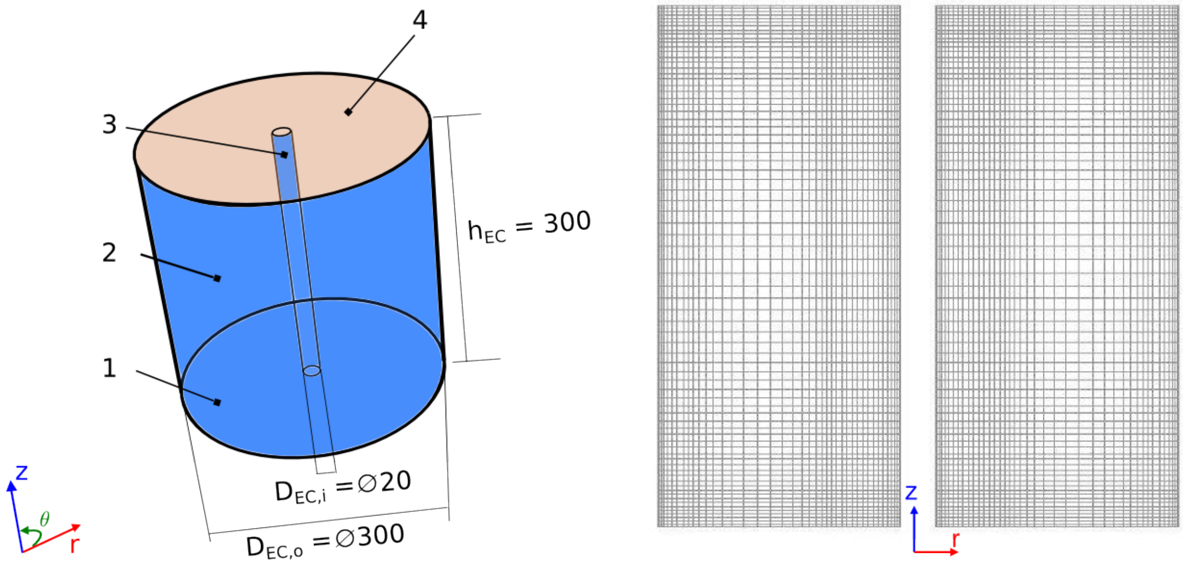

a)

b)

Figure VI.1: a) Schematics of the physical model including the geometric data in mm. 1- bottom insulator, 2- outer electrode, 3- inner electrode, 4- top insulator. b) Mesh representation in a vertical plane containing 333600 cells used in the computation of the flow in laminar and turbulent regime by the RANS turbulence models.

2.1 Geometrical data and properties

The selected geometry has a diameter of 300 mm and a height of 300 mm corresponding to a volume of 21 l or 0.021 m^3, same as the one of the pilot vessel used by K-UTEC AG Salt Technologies ([131]). Therefore the outer cylindrical electrode has this same geometrical data and the top and bottom insulator the same diameter.

A diameter of 20 mm is selected for the inner electrode to maximize the amount of usable volume and to keep low, possible overheating of the solution due to the Joule effect. Smaller values increases the electric current density, incrementing the temperature of the solution. Also, the electric current density must be lower than 2 A/cm^2 [48] to prevent the corrosion of the electrodes.

2.2 Physical properties of the fluid model

The physical model is filled with a fluid model made of sodium chlorate dissolved in water up to the saturation point [123]. The temperature dependencies of the physical properties such as density and viscosity, are assumed same as the water with an electrical conductivity of 34.2 S/m assumed constant and thermal conductivity of 0.561 W/(K·m) (Tab. VI.1).

Table VI.1: Physical properties of the fluid model [123]

Parameter	Value / temperature dependencies in °C
Density [kg/m^3]	$\rho_{EC}(T_{EC})$ = 1209.4 - 0.42T_{EC}
Dynamic viscosity [Pas]	$\eta_{EC}(T_{EC})$ = 0.00247 - 3 x 10$^{-5}T_{EC}$ + 2 x 10$^{-7}T_{EC}^2$
Electrical conductivity [S/m]	σ_{EC} = 34.2
Specific heat [J/(Kg·K)]	Cp_{EC} = 4183
Thermal conductivity [W/(K·m)]	λ_{EC} = 0.561

2.3 Operating parameters

The water content in the chemical solution imposes a limitation in the electric potential difference applied between the electrodes which equals to the standard potential of the water electrolysis of 1.229 V at 25 °C [90]. Therefore a RMS value of 0.8 V is selected to avoid the electrolysis and to restrict the electric current density in the solution and thus the heating.

An homogeneous magnetic flux density parallel to the z-axis is imposed in the whole geometry of the physical model. An RMS value of 10 mT is selected because it can be created with a simple arrangement of coils.

3 Numerical simulation

The numerical simulations are performed with the commercial computational fluid dynamics software ANSYS/ FLUENT v.13 using an hexahedral mesh generated by the commercial software Gambit v.2.4.

The unsteady RANS simulations are made with several mesh densities until obtaining mesh independent results with a time step of 0.005 s, keeping the CFL condition lower than 1 ($\frac{U\delta t}{\delta x} < 1$). A good compromise is obtained with a mesh containing 333 600 cells (Fig. VI.1.b). On the other hand, the numerical results of the LES made with a time step of 0.0005 s, keeping the CFL condition lower than 1, always depends on the mesh density, because it resolves the turbulent scales until the smallest cell. Therefore a good compromise between the grid size requirements and the computational resources with a mesh containing 4 474 740 cells is found [138].

Due to the axial symmetry of the geometry, the cylindrical coordinate system with coordinates (r, θ, z) is used in this study. The electric current density $\mathbf{J}_{EC}$ impressed in the fluid has only a radial component depending on the radial position r. The interaction of $\mathbf{J}_{EC}$ with the externally created magnetic flux density $\mathbf{B}_{EC}$ oriented axially produces a Lorentz force density $\mathbf{f_{L,EC}}$ having only an azimuthal component that depends on the radial position r (Fig. VI.2.b).

The fluid flow is initially studied analytically and numerically at a constant temperature of 20 °C without including the effects of the Joule heating (Eq. III.32). The initial value of the electric potential difference between the inner and outer electrode electrode is 0.0001 V giving a laminar flow. This value is increased until its maximum value of 0.8 V whereby a growing Lorentz force density is generated changing the flow towards the turbulent regime.

Currently, there are several RANS turbulence models based on the Boussinesq hypothesis to resolve the Reynolds stress tensor by means of a turbulent viscosity [126]. The turbulence models based on two scalar transport equations that can resolve rotating flow offered by the Fluent software [2], such as the $k-\varepsilon$ RNG model, the $k-\varepsilon$ Realizable model and the $k-\omega$ SST model are analyzed in this study.

Due to the convex profile of the flow field [136, 137], a curvature correction is necessary in the RANS models that modifies the production term (energy extraction from the mean flow to the large turbulent scales) of the transport equation for the turbulence kinetic energy k, the specific dissipation rate ω and the turbulent rate ε. The $k-\varepsilon$ models have already their own terms to take into account rotating flow, therefore this curvature correction could produce unexpected results. This correction is necessary because these models are insensitive to curvatures by default (see chapter III, section 4.2).

After validating the suitable RANS turbulence models with the LES results, a simulation with the temperature dependence of the physical properties of the fluid, including the effects of the Joule heating is performed in order to show their possible influences in the fluid flow. Then, the mean velocity distributions predicted by the selected model are required to compute the trajectories of passive particles with the discrete phase model. The particle positions are used to quantify the mixing grade by means of the stirring index (Eq. III.68).

3.1 Boundary conditions

The boundary conditions (fig. VI.1.a) applied to the geometrical model are:

- No-slip condition on the electrodes and insulators (velocity vector equal to zero).
- A convective heat flux on the surface of the outer electrode and insulators with a heat transfer coefficient of 10 W/(m^{2}K) and a surrounding temperature of 20 °C.
- An electric potential $\varphi_{EC,o}$ = 0 V applied on the outer electrode, a maximum $\varphi_{EC,i}$ = 0.8 V applied on the inner electrode and an electric potential gradient equal to zero applied on the top and bottom insulators.

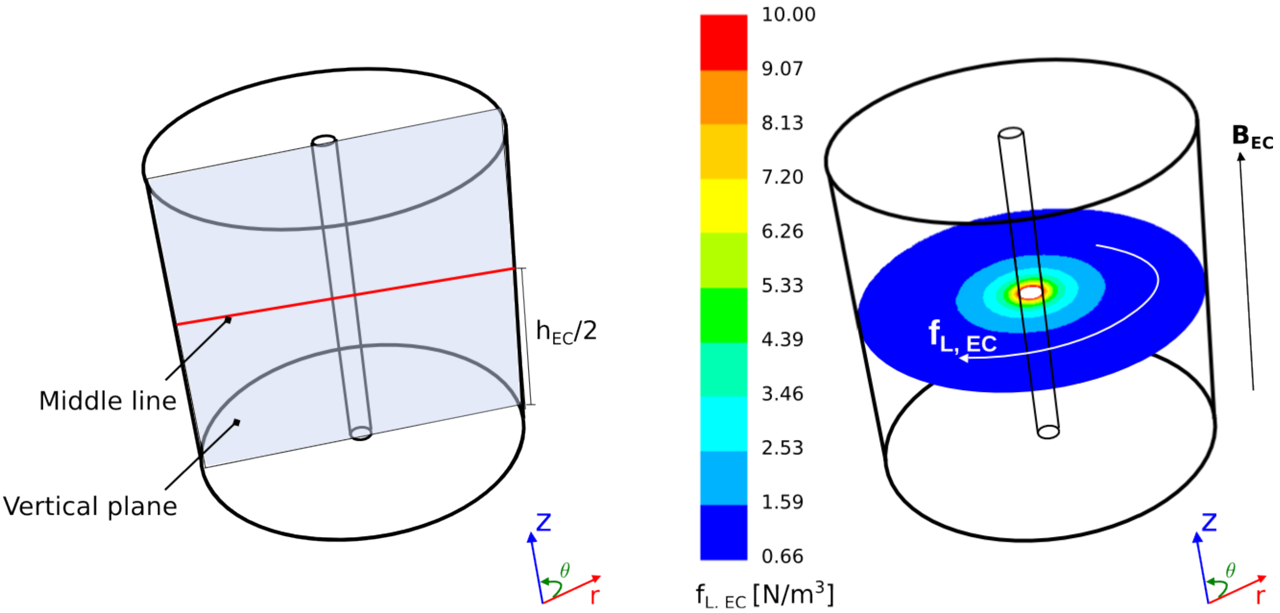

a) b)

Figure VI.2: a) Schematic of the middle line and vertical plane used to present the numerical results. b) Distribution of the Lorentz force density magnitude $f_{L,EC}$ in a cross section plane located in the middle of the physical model (z = 150 mm).

3.2 Laminar regime

The laminar regime of the fluid flow is obtained numerically when the modified Hartmann number M_{EC} (Eq. III.21) is lower than 93 and the Reynolds number Re_{EC} (Eq. III.19) is lower than 104. For bigger values, the flow develops radial velocities close to the outer electrode (Fig. VI.5.b). Therefore, the flow computation needs to take into account the contribution of the Reynolds stress tensor which is resolved with a turbulence model.

The computation of the fluid flow in laminar regime is made at a constant temperature of 20 °C and validated with an analytical analysis of the Navier-Stokes equations.

Analytical solution

Assuming the physical model is an infinitely long cylinder ($h_{EC} \to \infty$), the Lorentz force density $\mathbf{f_{L,EC}}$ is described with Eq. VI.1:

$$\mathbf{f_{L,EC}} = -\frac{1}{r}\frac{\sigma_{EC}\varphi_{EC,i}B_{EC}}{ln\left(\frac{D_{EC,i}}{D_{EC,o}}\right)}\hat{e}_\theta \tag{VI.1}$$

The flow driving by the Lorentz force density $\mathbf{f_{L,EC}}$ can be described by cylindrical coordinates r, θ and z as $U_{EC,r}$, $U_{EC,\theta}$ and $U_{EC,z}$ corresponding respectively to the radial, azimuthal and axial component of the velocity (see appendix A).

Furthermore, assuming the flow fully developed ($\partial U_{EC,\theta}/\partial\theta = 0$) and under isothermal conditions (ΔT_{EC} = 0) only the azimuthal component of the velocity $U_{EC,\theta}$ which value depends on the position r is obtained. With these conditions, the general Navier-Stokes equations for incompressible flows (Eq. A.1, A.2, A.3 and A.4) are simplified to the Eq. VI.2 and VI.3.

$$\rho_{EC}\left(\frac{U_{EC,\theta}^2}{r}\right) = \frac{\partial p_{EC}}{\partial r} \tag{VI.2}$$

$$0 = \eta_{EC}\left(\frac{1}{r}\frac{\partial}{\partial r}\left(r\frac{\partial U_{EC,\theta}}{\partial r}\right) - \frac{U_{EC,\theta}^2}{r}\right) - \frac{1}{r}\frac{\sigma_{EC}\varphi_{EC,i}B_{EC}}{ln\left(\frac{D_{EC,i}}{D_{EC,o}}\right)} \tag{VI.3}$$

The azimuthal velocity $U_{EC,\theta}$ has negative values due to the clockwise direction of the Lorentz force density (Eq. VI.1), but to better illustrate its distribution, its absolute value $|U_{EC,\theta}|$ is diagrammed. The Fig. VI.3.a and VI.3.b shows the distribution of $|U_{EC,\theta}|$ along the r-axis for Re_{EC} = 21 and M_{EC} = 47 corresponding to an electric potential $\varphi_{EC,i} = 0.0001V$. This velocity has a radial distribution independent on z (Fig. VI.3.b), but as expected depended on r with a distinct maximum value closer to the inner electrode according to the distribution of the Lorentz force density (Fig. VI.2).

In order to model numerically an infinity geometry along the z-axis, a null shear stress is applied on the top and bottom insulators. The simulated azimuthal velocity distribution $U_{EC,\theta}$ has a mean velocity magnitude of 0.01 cm/s corresponding to a Reynolds number $\mathrm{Re_{EC}}$ = 17 and a modified Hartmann number $\mathrm{M_{EC}}$ = 55 with a relative error of 0.8% respect to the analytical result (Fig.VI.3.a and VI.3.b).

Then the non-slip condition on the insulators is restored, giving an expected lower magnitude of the azimuthal velocity (Fig.VI.3.a and VI.3.c) due to the shear stresses applied by the insulators on the flow.

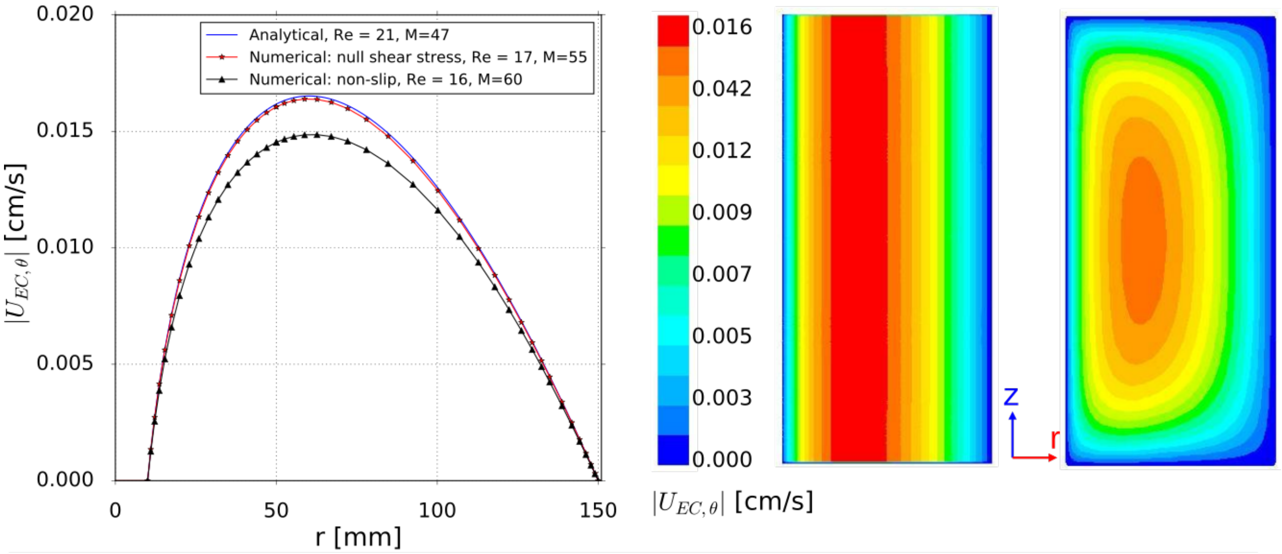

a) b) c)

Figure VI.3: Distribution of the absolute value of the azimuthal velocity $|U_{EC,\theta}|$. a) Analytical result in blue color, numerical simulation with a null shear stress condition in red color and in green color with the non-slip condition plotted in a middle line. b) Numerical result in a vertical plane with a null shear stress condition. c) Numerical result in a vertical plane with a non-slip condition.

Near the insulators, viscous forces in the boundary layer are important, generating a local imbalance between the pressure and the Lorentz force (Eq. VI.2). This reduces the azimuthal velocity $U_{EC,\theta}$ and the flow spiral radially inward, in the direction of low pressure (Fig. VI.4.a, No. 1). The velocity magnitude U_{EC} increases as the flow approach the inner electrode due to the mass conservation (Eq. III.16). Then, near the inner electrode an axial flow $U_{EC,z}$ is created forming two secondary flows, from the middle to the bottom and to the top, in the r-z plane ((Fig. VI.4, No. 2, 3, 4)).

This secondary flow is called the Ekman pumping superimposing to the primary swirling flow created by the Lorentz force. The boundary layer, where the local imbalance happen, is called the Ekman layer [89, 127].

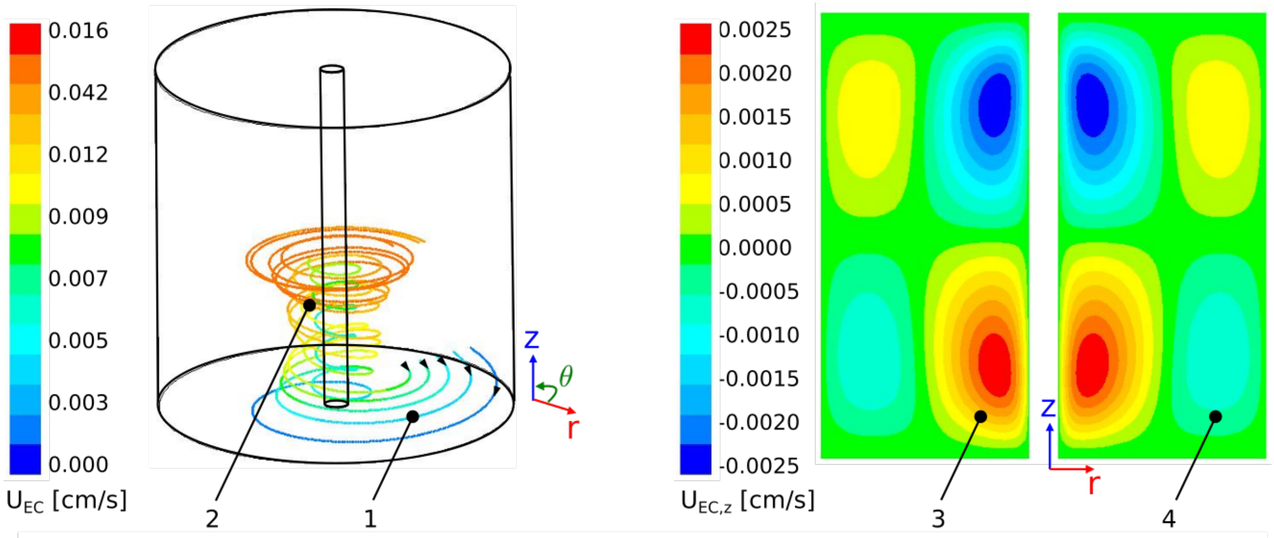

a) b)

Figure VI.4: a) Streamlines of 5 points with initial positions at (0, y = 70-140, z= 20) mm colored by the velocity magnitude. b) Distribution of the axial velocity $U_{EC,z}$ in a vertical plane. 1- spiral flow near the bottom insulator, 2- axial flow forming a secondary flow, 3- positive axial velocity forming the secondary flow, 4- negative axial velocity forming the secondary flow.

3.3 Instabilities

With the validated numerical model in laminar regime, the electric potential applied on the inner electrode is increased up to 0.01 V (up to $\mathrm{Re_{EC}}$=576 and $\mathrm{M_{EC}}$=168). At this electric potential level, the fluid flow starts to develop negative radial velocities close to the outer electrode (Fig VI.5.b).

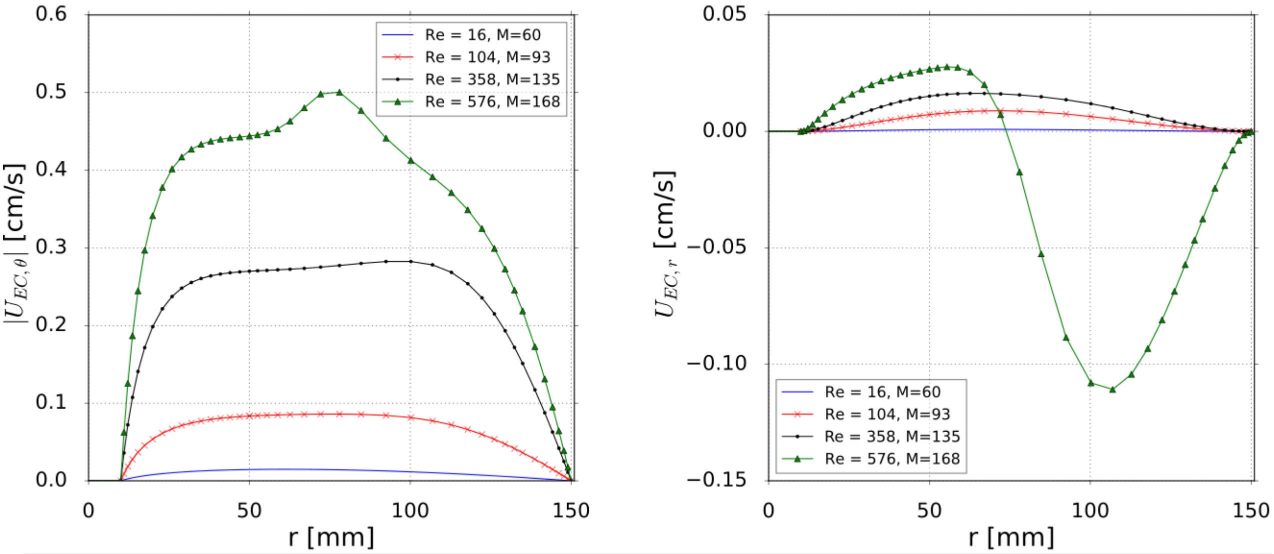

a) b)

Figure VI.5: Velocity distributions in a middle line for $\mathrm{M_{EC}}$= 60, 93, 135, 168 and $\mathrm{Re_{EC}}$ = 16, 104, 358, 576. a) Distribution of the absolute value of the azimuthal velocity $|U_{EC,\theta}|$. b) Distribution of the radial velocity $U_{EC,r}$.

These radial velocities form a primary jet (Fig. VI.6.a) that can be considered as a primary instability in the same way as the three-dimensional Taylor-Couette system [124], [125], affecting the velocity distribution (Fig VI.5.a and VI.6.b).

This first instability appears in the form of counter-rotating toroidal vortices called Taylor vortices that is a tertiary flow superposed to the primary and secondary flow. Then, while the Lorentz force density is increased due to the increasing of the electric potential, more jets are developed along the z-axis and close to the outer electrode changing their positions over time, breaking the symmetry of the system. Therefore, the fluid flow now is irregular and transient characterizing a turbulent regime (see chapter III) [129].

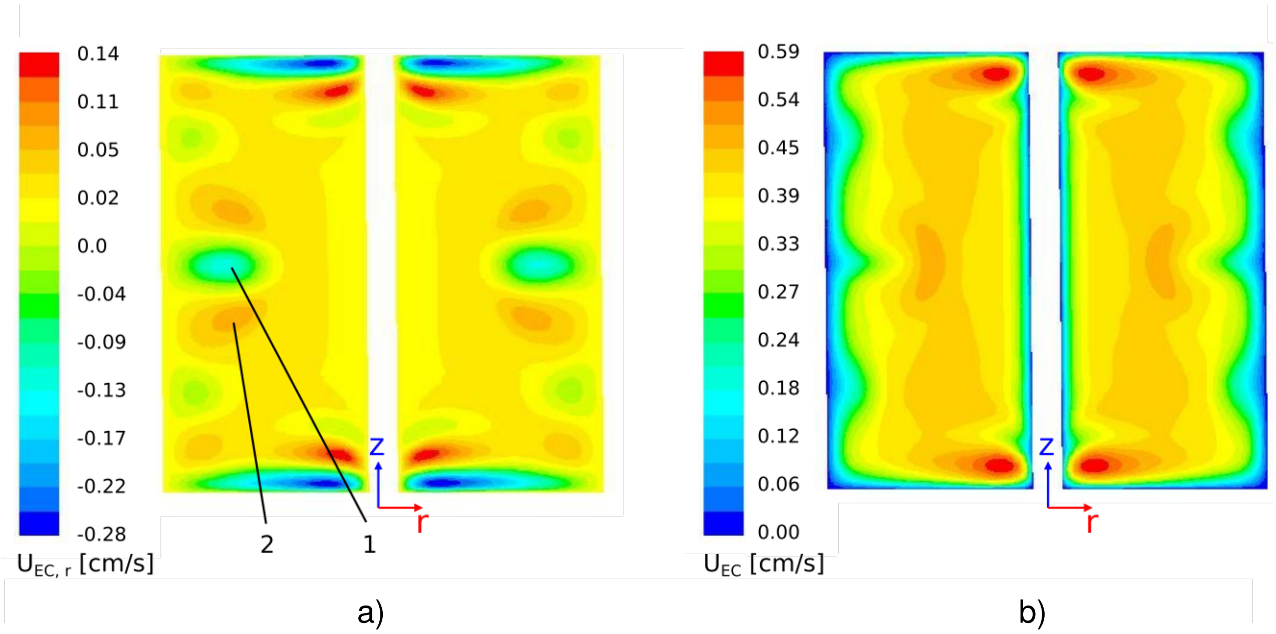

Figure VI.6: Distribution of the velocity in a vertical plane using different scales to show better their characteristics. a) Radial velocity $U_{EC,r}$ responsible of the jets development in the middle and close to each cover. b) Velocity magnitude U_{EC}. 1- positive radial velocity forming the tertiary flow, 2- negative radial velocity forming the tertiary flow.

3.4 Turbulent flow

When the modified Hartmann number M_{EC} is higher than 93 and the Reynolds number Re_{EC} is higher than 104, the flow becomes turbulent and the jets developed during the transition to turbulence loose their regularity.

The computation of the fluid flow in turbulent regime is made with the RNG $k-\varepsilon$, the Realizable $k-\varepsilon$ and the SST $k-\omega$ turbulence models. In order to resolve the boundary layer, wall functions are needed between the wall and the first computational node which in this case is located at $y^+ \approx 4$ laying in the viscous sublayer (chapter III, section 4.3).

The $k-\varepsilon$ models use an enhanced wall treatment which specifies the velocity, the dissipation rate ε and the turbulent viscosity with one equation model near the walls for $y^+<11.2$, instead of the standard wall function that specifies only the velocity and ε respecting the calculated y^+. According to [2], the enhanced wall treatment describes better the effects of pressure gradients and the high three-dimensionality of the flow near the wall region, than the standard wall function.

The SST $k-\omega$ model uses by default an enhanced wall function that specifies the velocity and the specific dissipation ω near the walls [2].

The numerical predictions made by the different turbulence models are evaluated with the mean velocity magnitude distribution in a middle line of the physical model.

The Fig. VI.7.a shows the mean velocity magnitude distribution without using the curvature correction with its maximum value located close to the outer electrode. The mismatch of the velocity distribution around r $\approx$ 15 mm predicted by the $k-\varepsilon$ models, comes from the enhanced wall treatment which computes the turbulent viscosity with one equation model for $y^+<11.2$ (r $\approx$ 15 mm). Due to the mismatch, another simulation is performed with the $k-\varepsilon$ models using the standard wall function, giving better results (Fig. VI.8.a).

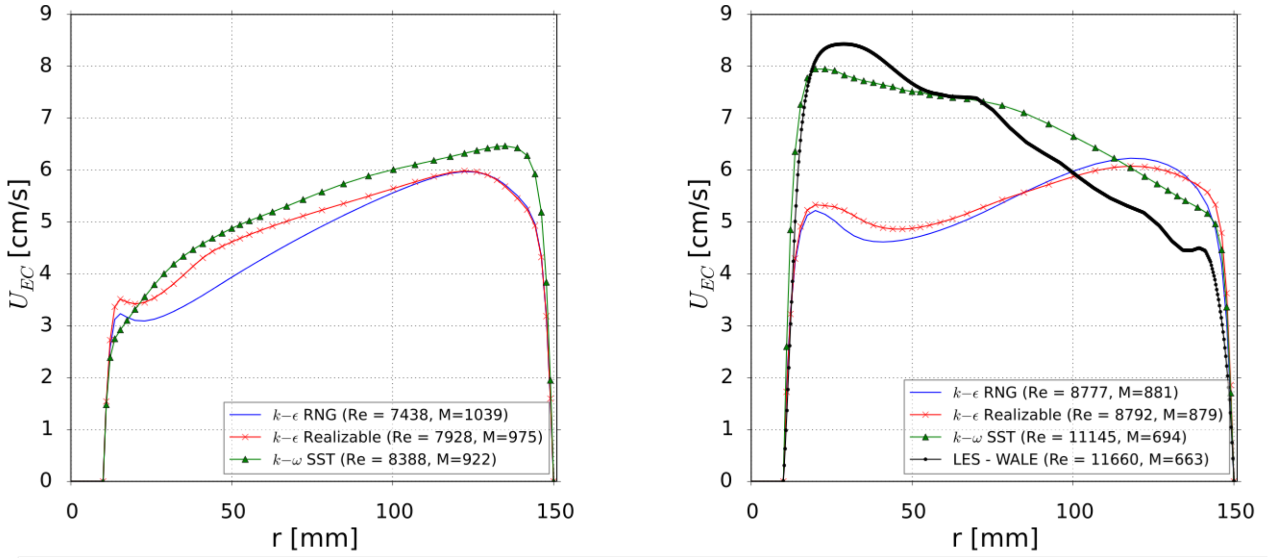

a) b)

Figure VI.7: Mean velocity magnitude distribution in a middle line. a) RANS models without the curvature correction using an enhanced wall treatment for the $k-\varepsilon$ models. b) RANS models with the curvature correction using an enhanced wall treatment for the $k-\varepsilon$ models and LES with the WALE sub-grid model.

The Fig. VI.7.b shows the mean velocity magnitude distribution using the curvature correction with its maximum value located close to the inner electrode. Here also, the turbulent viscosity computed by the enhanced wall treatment used in the $k-\varepsilon$ models, creates a mismatch on the velocity around r = 15 mm propagating in the whole domain giving inconsistent results. Therefore, another simulation with the $k-\varepsilon$ models using the standard wall function is performed obtaining consistent results (VI.8.b).

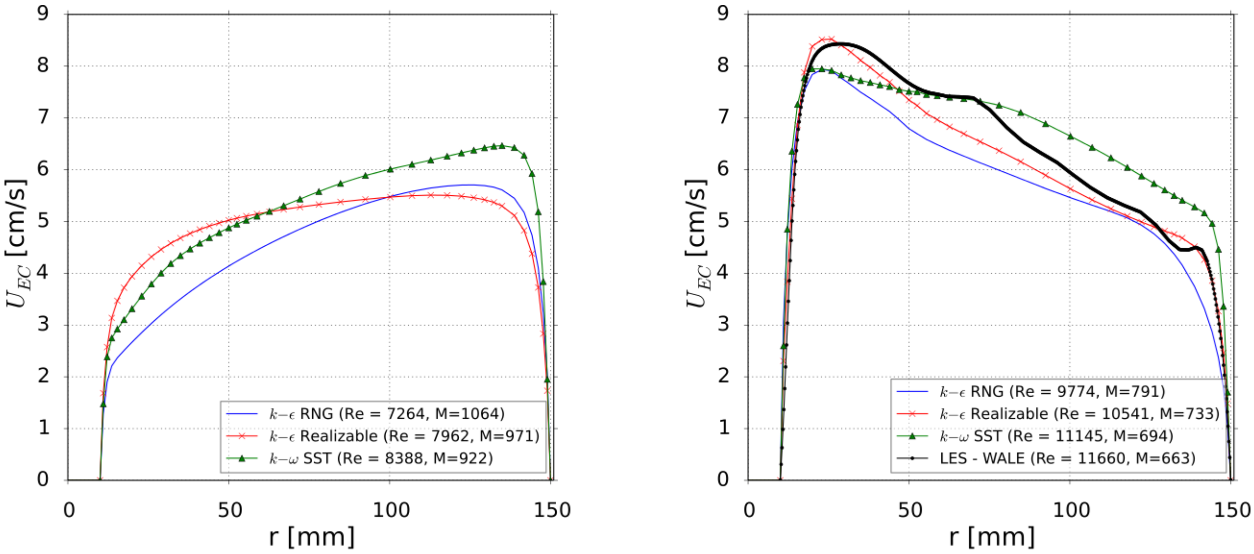

a)

b)

Figure VI.8: Mean velocity magnitude distribution in a middle line. a) RANS models without the curvature correction using the standard wall function for the $k-\varepsilon$ models. b) RANS models with the curvature correction using the standard wall function for the $k-\varepsilon$ models and LES with the WALE sub-grid model.

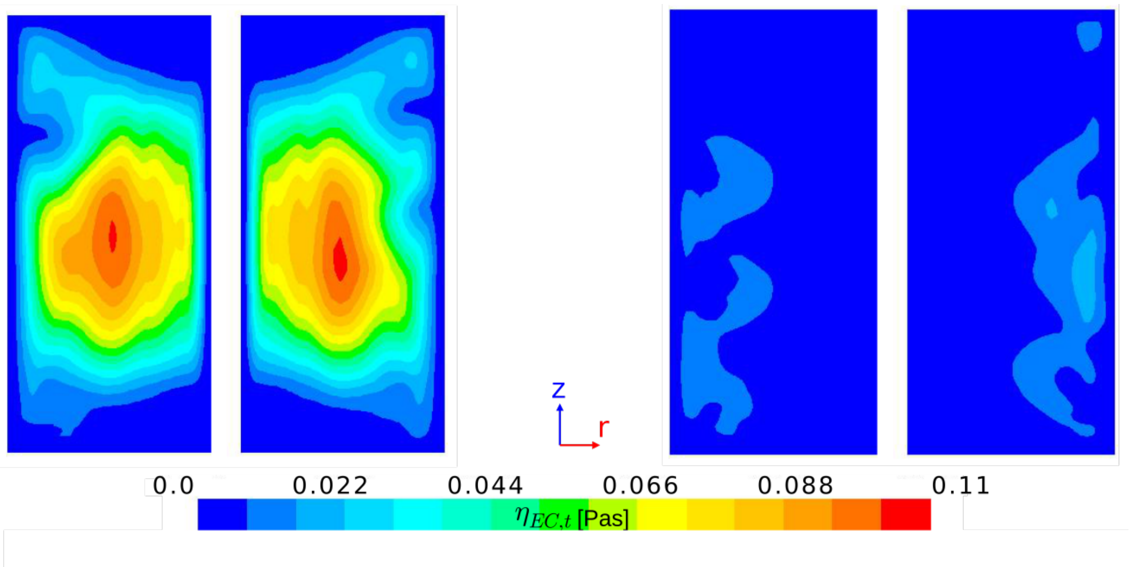

a)

b)

Figure VI.9: Distribution of the turbulent viscosity $\eta_{EC,\tau}$ in a vertical plane computed with the $k-\omega$ SST model. a) Without the curvature correction. b) With the curvature correction.

The differences between the computation of the mean velocity magnitude distribution using and not using the curvature correction come from the production term in the transport equation of these models. The production is over predicted affecting the turbulent viscosity (Fig. VI.9) and giving a maximum velocity close to the outer electrode. This affirmation is based on the LES results because it can resolve the large turbulent scales of the flow, which are susceptible to the shape of the geometry, and models the scales smaller than the computational cell [136, 137].

The size of the resolved turbulent scales (vortices) depends on the mesh which now has 4.5 million of cells giving an $y^+ \approx 1$. Then, the scales smaller than the mesh cells are filtered producing a sub-grid stress tensor (chapter III, section 4.2). This tensor is computed with the Boussinesq hypothesis and its turbulent viscosity is modeled with the WALE sub-grid-scale turbulence model (see chapter III, section 4.2).

The statistical averaging velocity magnitude distribution computed with LES is compared with the RANS results in the Fig. VI.8.b. The RNG $k-\varepsilon$, Realizable $k-\varepsilon$ and SST $k-\omega$ models using the curvature correction give equivalent results with a mean difference respect to the LES of 12.3 %, 5.9 % and 11.8 % respectively.

Also it is performed an LES with the Smagorinsky-Lilly model, which gives similar statistical velocity distribution to the computed by the LES with the WALE model. Therefore, the modeled small scales play a negligible role in the mean velocity distribution.

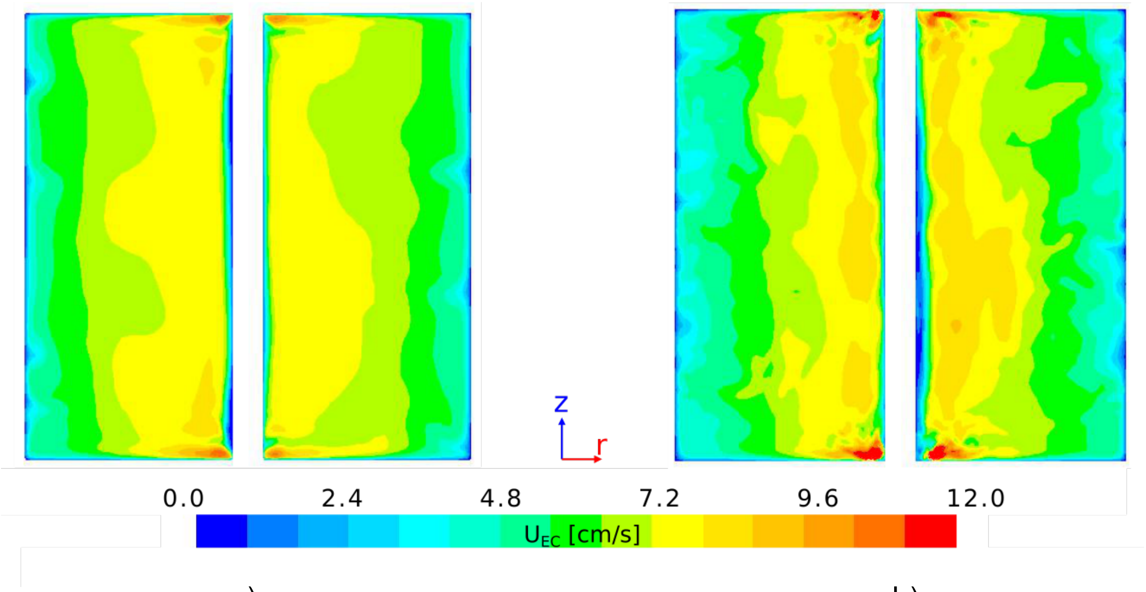

a) b)

Figure VI.10: Mean velocity magnitude distribution in a vertical plane. a) Computed with the $k-\omega$ SST model including the curvature correction. b) Computed with the LES using the WALE sub-grid model.

The SST $k-\omega$ model is selected for the subsequent validation despite its error, higher than the Realizable $k-\varepsilon$, and because it is a more robust model than the $k-\varepsilon$ models for this type of flow, due to the fact that it is designed for the near wall region where as the $k-\varepsilon$ not [2]. The Fig. VI.10 shows the mean velocity magnitude distribution computed by the SST $k-\omega$, which has a mean flow distribution similar to the one predicted by the LES.

Until this point, all simulations are performed at a constant temperature of 20 °C. If the temperature dependencies of the physical properties are considered (Tab VI.1), as well as the Joule heating that introduces a thermal power of 15 W, then the temperature of the fluid rises up to 0.4 K close to the inner electrode from an starting temperature of 20 °C.

This increase on the temperature doesn't modify significantly the physical properties of the fluid and thus the convection currents due to buoyancy are very small compared with the main flow. Therefore the mean velocity distribution at constant temperature of 20 °C has the same tendency as in the temperature dependent case with a relative error of 2% (Fig. VI.11).

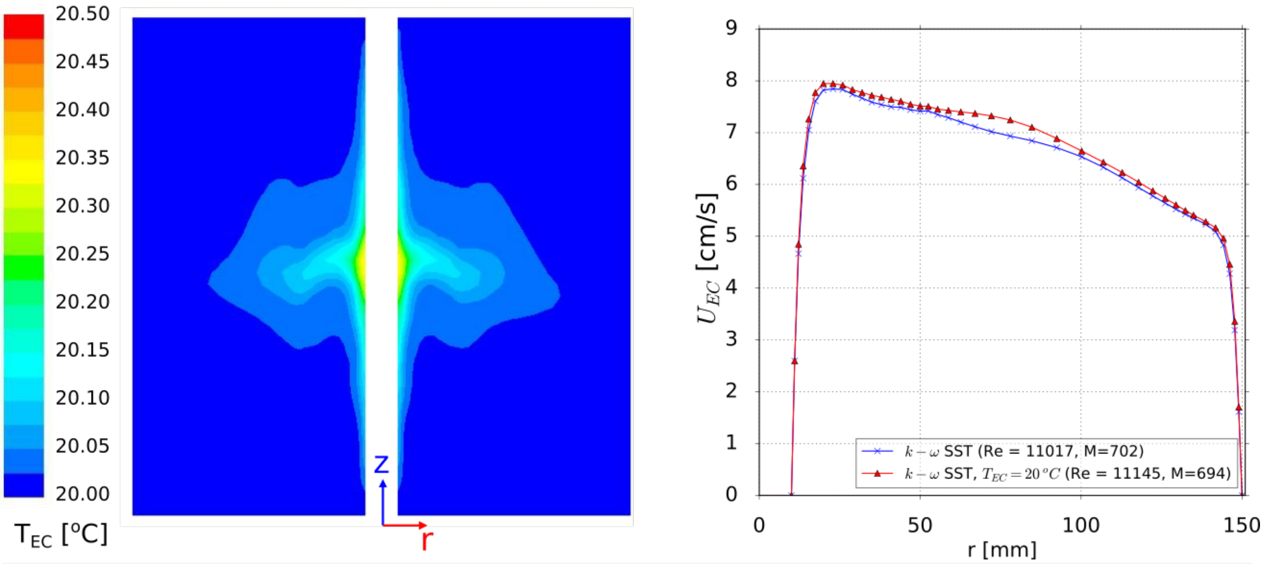

a) b)

Figure VI.11: Numerical simulation performed with the $k-\omega$ SST model including the curvature correction a) Temperature distribution in a vertical plane. b) Mean velocity magnitude distribution along the radial position in a middle line. In red color - Numerical simulation using a constant temperature of 20 °C without taking into account the effects of the Joule heating. In blue color - Numerical simulation using the temperature dependence of the physical properties of the fluid model including the effects of the Joule heating.

3.5 Particle distributions

The mean velocity distribution computed with the $k-\omega$ SST model at a constant temperature of 20 °C is used to compute the mixing capabilities of the Lorentz force by means of the spatial distribution of a group of passive particles. It is selected a starting number of 10 000 particles, but it is introduced effectively into the model 9088 because some of them lie on the top surface of the inner electrode.

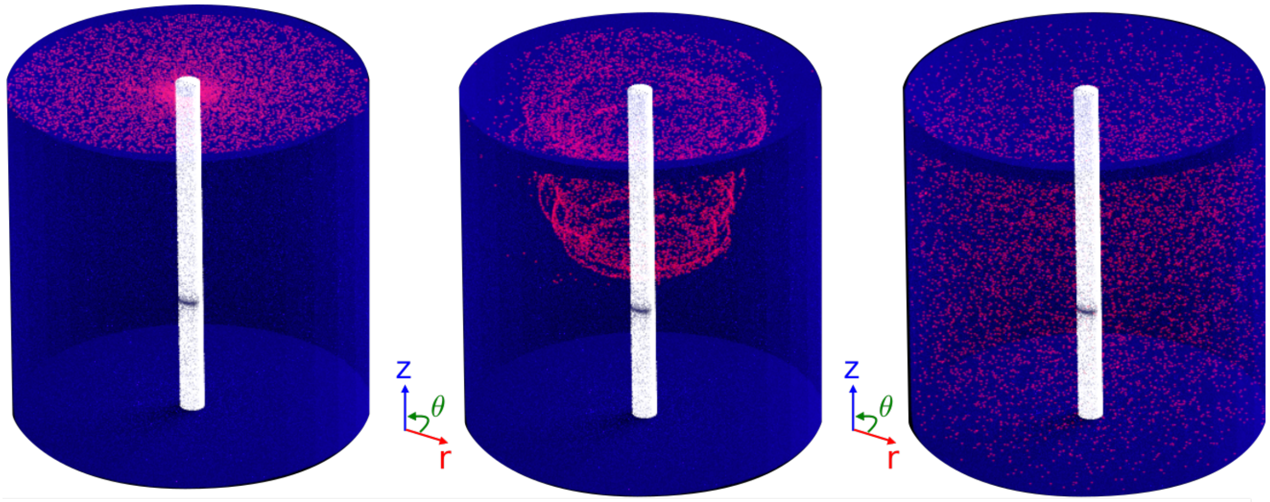

a) b) c)

Figure VI.12: a) Initial random particle distribution on a horizontal plane (r, θ, z = 149) mm at $t_{EC,p}$ = 0 s. b) Particle distribution at $t_{EC,p}$ = 50 s c) Particle distribution at $t_{EC,p}$ = 500 s.

The Lorentz force density creates several fluid flow configurations, but the study of the mixing process is made in turbulent regime achieved with the maximum electric potential of 0.8 V applied on the inner electrode, and a magnetic flux density of 10 mT giving a $\mathrm{Re}_{\mathrm{EC}}$ = 11145 and M_{EC} = 694. As a result, the turbulent properties of the fluid flow such as irregularity used to mix the solution, don't allow to compute the particle trajectories considering a particular fluid flow configuration at a given time. Therefore, the computation of the particle positions is made at the end of each time step of the fluid flow computation (unsteady particle tracking).

The passive particles are located at the top of the physical model after the fluid flow is developed completely (Fig. VI.12.a) corresponding to a particle time computation of $t_{EC,p} = 0\,s$. These particles cover the whole surface with a random distribution (Fig. VI.12.a) because in order to produce a good mixing, the fluid flow must be capable to carry in the whole volume particles located at different positions on the top surface.

The Fig. VI.12.b shows the particle distribution at $t_{EC,p}$ = 50 s where the fluid flow starts to carry the particles in the volume. The Fig. VI.12.c shows the particle distribution at $t_{EC,p}$ = 500 s where the particles start to spread in the whole volume with a random distribution.

3.6 Stirring index ε_{EC}

The quantification of the mixing grade is made by the stirring index ε_{EC} (Eq. III.68) using the three dimensional position of 9088 particles. For that purpose, the physical model is covered with 8000 hexahedral boxes with a size of 15 mm, from which only the boxes inside the physical model are used. Then the number of particles is increased until obtaining a constant value for the index.

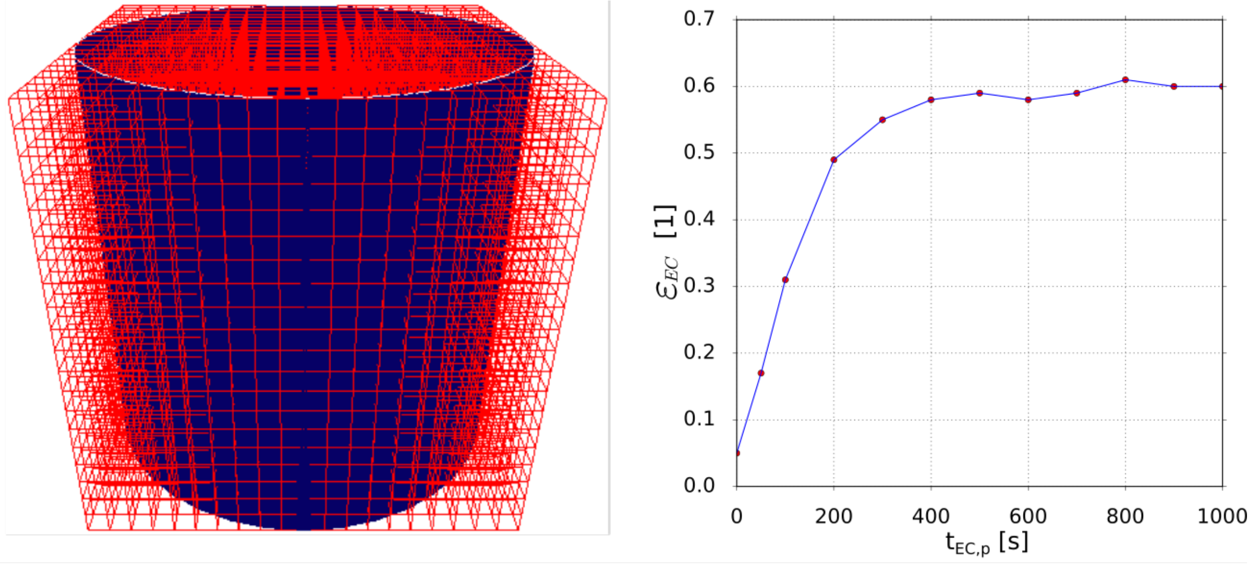

a) b)

Figure VI.13: a) 8000 hexahedral boxes with a size of 15 mm covering the whole volume of the physical model. b) Evolution of the stirring index ε_{EC} computed with 9088 particles.

The Fig VI.13.b shows the evolution in time of the stirring index achieving its maximum value of 0.6 when the time is higher than 400 s. Then, using the same box size of 15 mm as well as 39 596 particles and 79 059 particles, a stirring index of 0.71 and of 0.78 is respectively obtained. But, when the box size is reduced up to 10 mm, a stirring index of 0.61 is obtained for 39 596 particles. When the box size is reduced up to 7.5 mm, a stirring index of 0.60 is obtained for 79 059 particles.

In case the flow is in laminar regime, the azimuthal primary flow makes circulate the particles around the inner electrode, and the secondary flows created by the Ekman pumping makes circulate the particles in a close loop. The secondary flows create two well defined zone, from the top to the middle and from the bottom to the middle, that don't exchange momentum confining the particles. When the laminar flow develops the first instability, a tertiary flow is created in the middle of the physical model driving the particles in a torodial vortex but still the particles circulate in a close plath. When the torodial vortices start to change their positions over time, the necessary conditions of good mixing start to appear such as separate initially close part and bring together initially distant parts (chapter III, section 5). Therefore, the turbulence properties of the flow enhance significantly the mixing process started by the the primary azimuthal flow, created by the Lorentz force density.

4 Experimental design

The experimental validation of the mean velocity distribution computed with the RANS $k-\omega$ SST turbulent model and with the LES using the subgrid-scale WALE turbulent model, needs the design of a magnetic system able to produce up to 10 mT. The design of the electrode arrangements is already defined in the description of the physical model. Therefore, it is necessary only to take into consideration the selection of the material of the electrodes that must hold the corrosion produced by the dissolved salt [134].

Initially, the physical model is scaled down, but to achieve the same Reynolds number as in the turbulent case (Re $\approx$ 11000), it is necessary to increase the mean flow velocity by increasing the Lorentz force density. But the amount of the Lorentz force density that can be produced is limited by the maximum electric potential that can be used without producing the water redox, and the maximum magnetic flux density that can be created by a simple arrangement of coils as seen in the project I (see chapter IV, section 2.4). Therefore, the design of the coil system is made using the unchanged geometrical dimensions of the crystallizer physical model (Fig. VI.1.a).

The magnetic system is made with an arrangement of coils made of copper wire that can produce an homogeneous field in the volume of the physical model. For that purpose, three different coil configurations are studied; the Helmholtz coil, an improvement of the Helmholtz coil and a Maxwell coil. In each of them, a parametric analysis is performed with the finite element software FEMM v.4.2 [130].

The voltage and thus the electric current $\mathrm{I_{EC,C}}$ used to energize the coils are sinusoidal with a frequency $\mathrm{f_{EC}}$ of 50 Hz. Therefore, the variation of the magnetic flux ϕ_{EC} associated to this current induces a voltage $\mathrm{U_{EC,L}}$ in the coil described by the Faraday's law:

$$U_{EC,L} = \frac{-d\phi_{EC}}{dt} = -L_{EC}\frac{dI_{EC,C}}{dt} \tag{VI.4}$$

where $\mathrm{L_{EC}}$ is the inductance of the coil configuration at a permeability $\mu = \mu_O$. Numerically, the magnetic flux density $\mathbf{B_{EC}}$ is computed with the vector potential $\mathbf{A_{EC}}$ approach (See chapter III, section 4). Then, the magnitude of the total voltage drop $\mathrm{U_{EC,T}}$ which includes the drop due to the electrical resistance $\mathrm{R_{EC}}$ ($U_{EC} = I_{EC,C}R_{EC}$) as well as the total power $\mathrm{P_{EC,T}}$ and Ohmic losses $\mathrm{P_{EC,R}}$ in the coil system can be calculated with:

$$U_{EC,T} = I_{EC,C}\sqrt{R_{EC}^2 + (2\pi f_{EC}L_{EC})^2} \tag{VI.5}$$

$$P_{EC,T} = U_{EC,T}I_{EC,C} \tag{VI.6}$$

$$P_{EC,R} = R_{EC}I_{EC,C}^2 \tag{VI.7}$$

The parametric analysis starts with a coil arrangements that has only one turn, then progressively more turns are added in the radial r and axial z direction until obtaining the best configuration, with the lowest voltage drop and the magnetic flux density of 8 mT. Finally the temperature of the coils cooled down by natural convection with a heat transfer coefficient of 10 W/(m^{2}K) and a surrounding temperature of 25 °C is computed with the appendant total power and Ohmic losses.

4.1 Physical properties and geometrical data of the coil

The coils are made of copper wire (Tab. VI.2) with a diameter of 1.18 mm and of 1.70 mm including the insulation, which gives a cross section area of 2.26 mm^2 with a winding filling factor of 0.8. To avoid the use of a cooling system, the electric current density is limited to 2 A/mm^2 to keep the temperature of the coils low enough [106].

Table VI.2: Physical properties of the copper wire

Density [Kg/m^3]	8978
Specific heat [J/(Kg·K)]	381
Thermal conductivity [W/(m·K)]	387.6
Electric conductivity (130 °C) [MS/m]	36.5*

* Data from the project [106]

4.2 Validation of the finite element software FEMM

The FEMM software is validated with measurements of the axial magnetic flux density $B_{EC,z}$ performed at the TU Ilmenau [139]. For that, an arrangement of three coils with a winding number w_{EC} = 442 operating with an RMS value of the electric current $I_{EC,C}$ = 4 A (Fig. VI.14) is used. Also, the Biot-Savart equation implemented in a C++ code is used to validate the FEMM software.

The Fig. VI.15.a and Fig. VI.15.b show the measurements made by [139] of the axial magnetic flux density $B_{EC,z}$ along the z-axis (r = 0,z) mm and along the r-axis (r,z = 0) mm respectively as well as the numerical computation performed with the FEMM software and the Biot-Savart equation.

The distribution of the axial component of the magnetic flux density $B_{EC,z}$ along the z-axis and along the r-axis computed with FEMM software deviates respectively 1.1 % and 0.9 % from the experimental measurements (no experimental errors on the measurement system and position system were provided by [139]). Whereas the calculation with the Biot-Savart equation deviates respectively 0.9 % and 1.1 %.

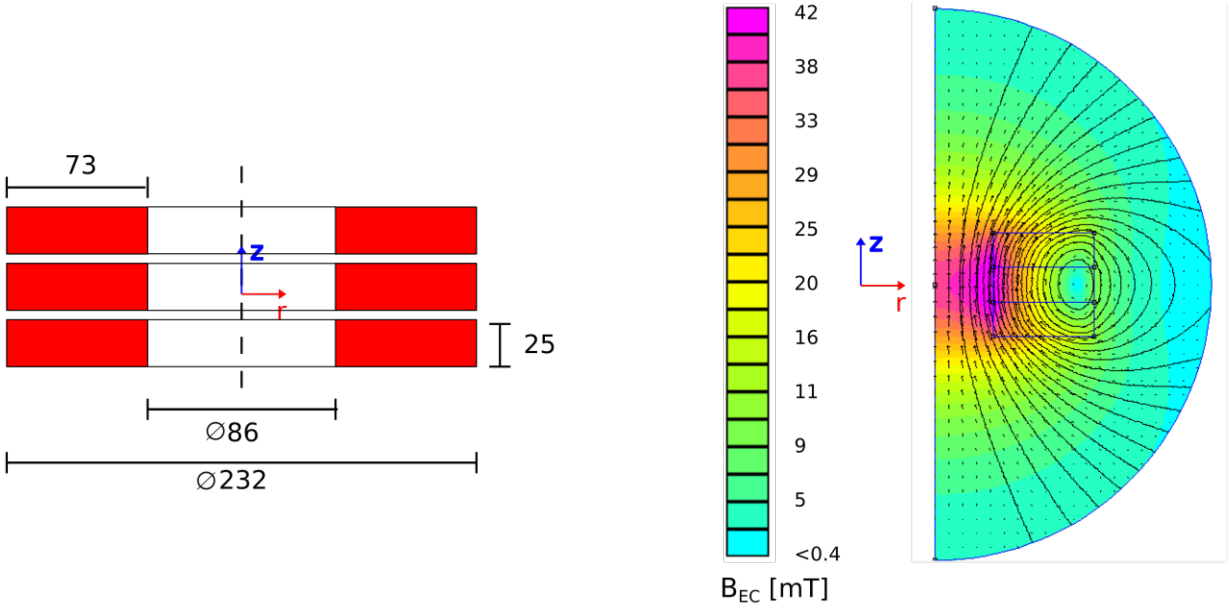

a) b)

Figure VI.14: a) Schematics of the three coil arrangements with the geometrical data in mm. b) Computation of the magnetic flux density magnitude B_{EC} with the FEMM software in 2D axisymmetric mode, using an RMS electric current $I_{EC,C}$ = 4 A.

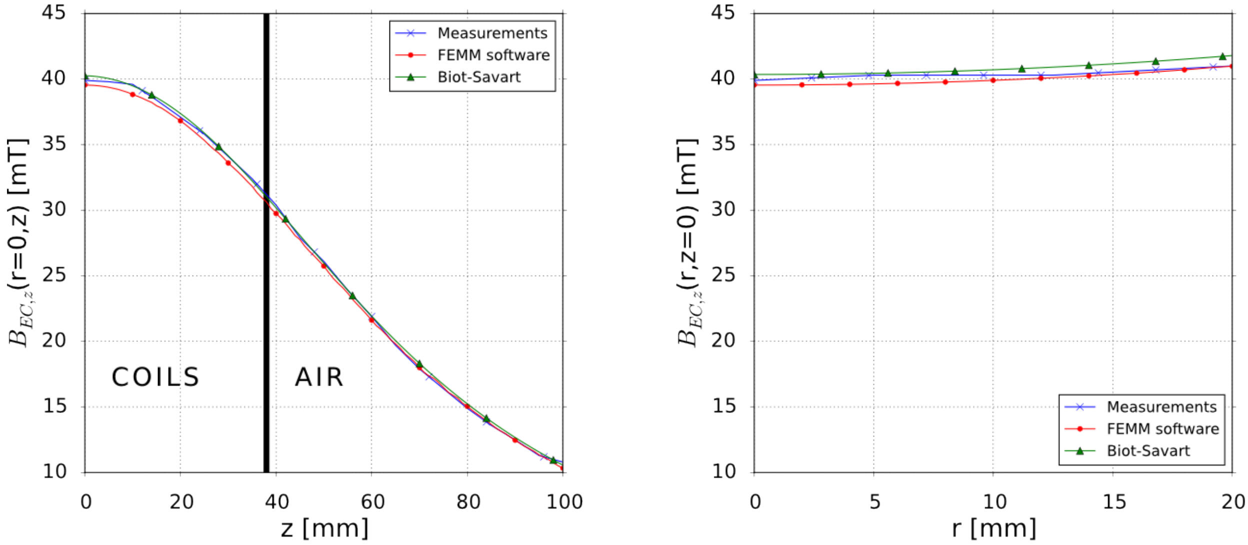

a) b)

Figure VI.15: Distribution of the axial component of the magnetic flux density $B_{EC,z}(r,z)$ where the experimental data [139] is in blue color, the FEMM results in red color and the Biot-Savart results in green color. a) Distribution of $B_{EC,z}(r=0, z)$ along the z-axis. b) Distribution of $B_{EC,z}(r, z = 0)$ along the r-axis.

4.3 Helmholtz coil

The Helmholtz coil is made of two coils where the distance between these two have to be equal to their radius r_{EC}. They are set apart each other 300 mm to cover the physical model volume (Fig. VI.16).

The parametric analysis performed with the FEMM software, uses a maximum electric current density of 2 A/mm^2 defining the electric parameters (Tab. VI.3) and the geometrical configuration (Fig. VI.16) of the Helmholtz coil keeping low the temperature.

Table VI.3: Electrical parameters of the Helmholtz coil arrangement

Coils	w_{EC} [1]	$I_{EC,C}$ [A]	R_{EC} [Ω]	$P_{EC,R}$ [W]	L_{EC} [mH]	B_{EC} [mT]	$U_{EC,T}$ [V]	$P_{EC,T}$ [W]
Top	266	4.52	6.08	124.2	60	5.14	89.8	405.8
Bottom	266	4.52	6.08	124.2	60	5.14	89.8	405.8

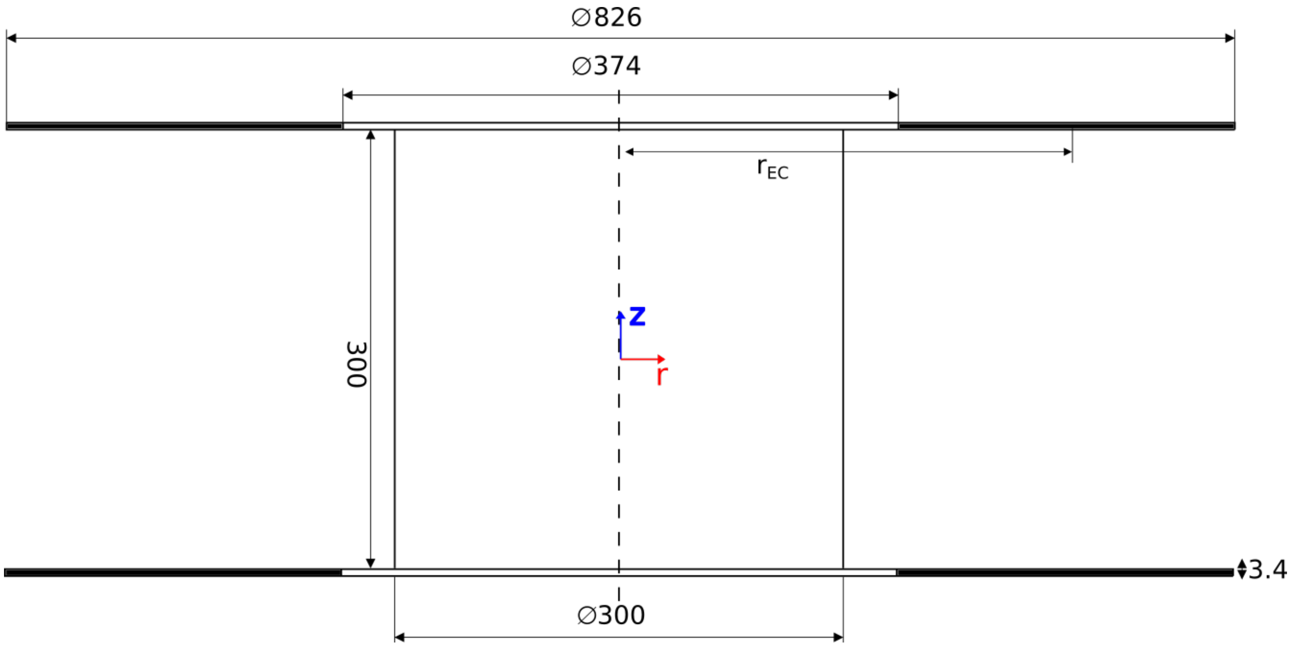

Figure VI.16: Schematic of the Helmholtz coil.

The Fig. VI.17.a shows that is possible to achieve only a mean axial magnetic flux density of 5 mT with a total power of 812 W. The total power increments the mean stationary coil temperature up to 67 °C. Also, the homogeneity of the magnetic flux density is only kept in half of the physical model region, then for larger values ($r > 70$ mm) the magnetic flux density diverges from the mean value up to 1 mT (Fig. VI.17.a).

As a result, the capabilities of an improvement of this configuration proposed by [133] is explored.

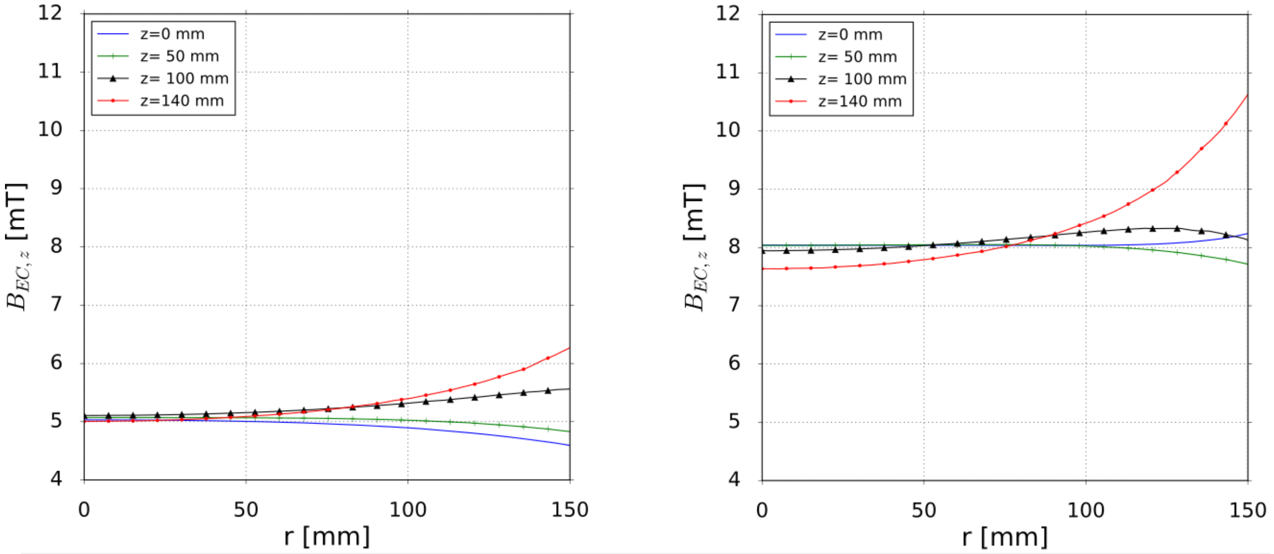

a) b)

Figure VI.17: Distribution of the axial component $B_{EC,z}$(r,z) of the magnetic flux density along the r-axis for different axial positions, z=0 mm, z=50 mm, z=100 mm and z=140 mm. a) Produced by the Helmholtz coil with the optimal design according to Tab. VI.3 and Fig. VI.16. b) Produced by the improved Helmholtz coil with the optimal design according to Tab. VI.4 and Fig. VI.18.

4.4 Improvement of the Helmholtz coil

The magnetic flux density $\mathbf{B_{EC}}$ can be increased and homogenized along the r-axis using a third coil in the middle of the physical model [133] (Fig. VI.18). The winding number $w_{EC,m}$ of the additional coil is determined by the winding number w_{EC} of the coils located at the ends of the geometry (Eq. VI.8). The distance $h_{EC,m}$ from the middle coil to the external coils is determined by the radius r_{EC} of the external coils (Eq. VI.8). But, in order to match the geometry of the crystallizer physical model, the relation for h_{EC} has to be broken.

$$w_{EC,m} = 0.531 w_{EC} \qquad h_{EC,m} = 0.7601 r_{EC} \tag{VI.8}$$

The parametric analysis performed with the FEMM software, uses a maximum electric current density of 2 A/mm^2 defining the electric parameters (Tab. VI.4) and the geometrical configuration (Fig. VI.18) of the improved Helmholtz coil keeping low the temperature.

Table VI.4: Electrical parameters of the improved Helmholtz coil arrangement

Coils	w_{EC} [1]	$I_{EC,C}$ [A]	R_{EC} [Ω]	$P_{EC,R}$ [W]	L_{EC} [mH]	B_{EC} [mT]	$U_{EC,T}$ [V]	$P_{EC,T}$ [W]
Top	282	4.5	5.14	105	62	8	91	411
Middle	147	4.5	2.7	54.8	33	8	50	219
Bottom	282	4.5	5.14	105	62	8	91	411

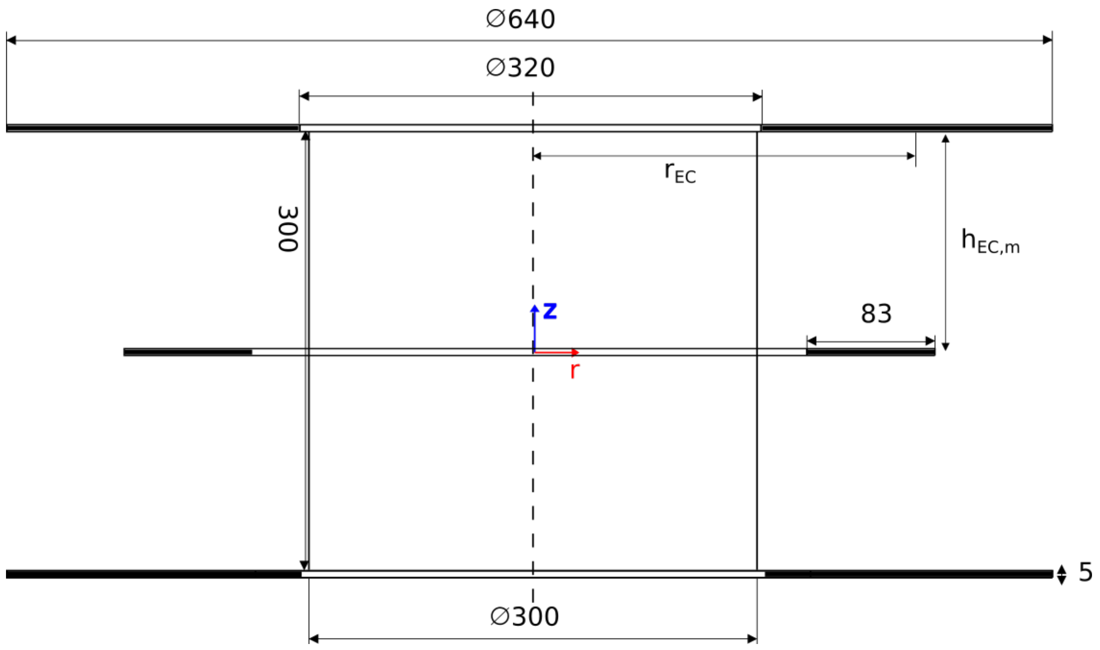

Figure VI.18: Schematic of the improved Helmholtz coil configuration.

This configuration achieves a mean axial magnetic flux density of 8 mT in the range of r = ± 100 mm and z = ± 50 mm with a total power of 1041 W (Tab. VI.4) and with a coil temperature of 108 °C.

The homogeneity of the magnetic flux density is improved, been stable along the r-axis up to z = ±100 mm. Close to the top and bottom insulators (z = ±140 mm) the magnetic flux density diverges from the mean value up to 3 mT for a radial distance $r > 100$ mm (Fig. VI.17.b).

In order to reach 10 mT, it would be necessary to increment the electric current. To stabilize the temperature of the coils, an additional cooling by artificial ventilation is required.

4.5 Maxwell coil

The study made by [133] proposed an alternative configuration with three coils called Maxwell coil (Fig. VI.19). The winding number $w_{EC,m}$ of the coil located in the middle is determined by the winding number w_{EC} of the coils located at the ends of the geometry (Eq. VI.9). The distance $h_{EC,m}$ from the middle coil to the external coils is determined by the position $r_{EC,m}$ in the r-axis of the center of the middle coil (Eq. VI.9).

But, in order to match the geometry of the reactor, the relation for h_{EC} has to be broken.

$$w_{EC} = \frac{49}{64} w_{EC,m} \qquad r_{EC} = \sqrt{\frac{4}{7}} r_{EC,m} \qquad h_{EC,m} = \sqrt{\frac{3}{7}} r_{EC,m} \tag{VI.9}$$

The parametric analysis performed with the FEMM software, uses a maximum electric current density of 2 A/mm^2 defining the electric parameters (Tab. VI.5) and the geometrical configuration (Fig. VI.19.a) of the Maxwell coil keeping low the temperature.

Table VI.5: Electrical parameters of the Maxwell coil

Coils	w_{EC} [1]	$I_{EC,C}$ [A]	R_{EC} [Ω]	$P_{EC,R}$ [W]	L_{EC} [mH]	B_{EC} [mT]	$U_{EC,T}$ [V]	$P_{EC,T}$ [W]
Top	250	4.5	3.2	64.9	44	10	64.1	289.7
Middle	325	4.5	5.5	111.5	99	10	142.7	645.1
Bottom	250	4.5	3.2	64.9	44	10	64.1	289.7

This configuration achieves the desired mean axial magnetic flux density of 10 mT with a total power of 1225 W (Tab. VI.5). But, the homogeneity of the magnetic flux density distribution is lower than the improved Helmholtz coil configuration, beginning to diverge from the mean value up to 3 mT for a distance r $>$ 50 mm (Fig. VI.19.b).

Therefore, from the three analyzed coil configurations, the best results related to the field homogeneity are identified at the specified geometry of the physical model with the improved Helmholtz coil (Chapter VI, section 4.4).

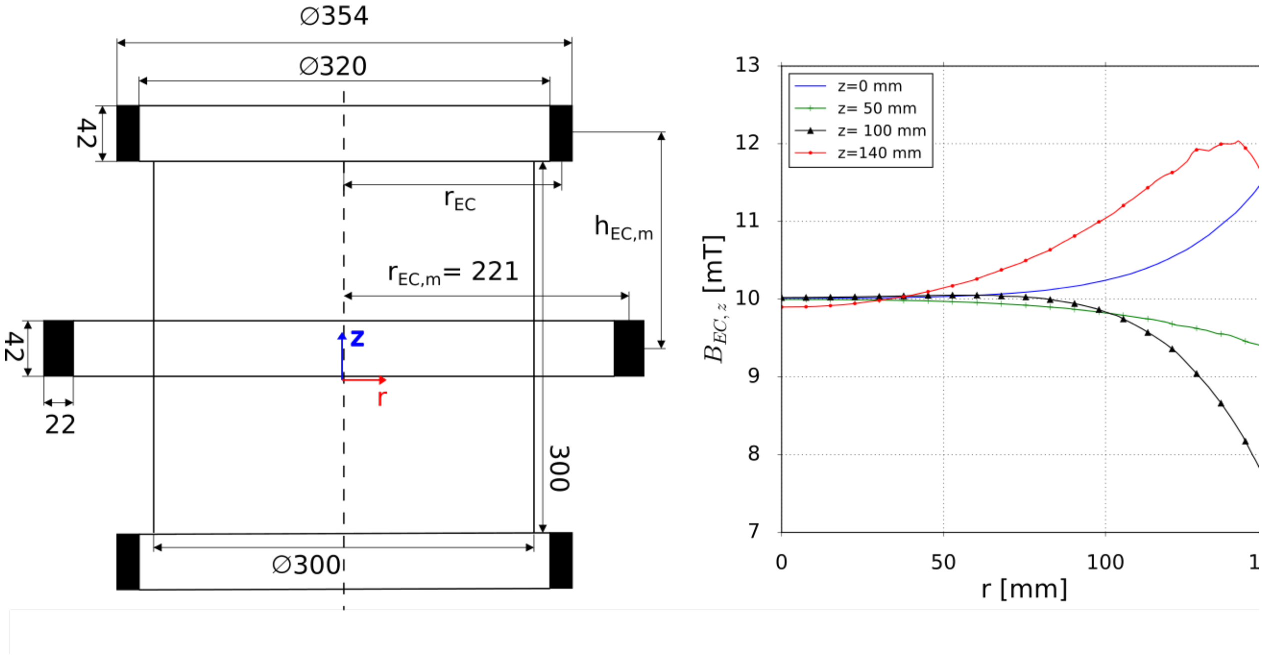

Figure VI.19: a) Schematic of the Maxwell coil configuration. b) Distributions of the axial component $B_{EC,z}$(r,z) of the magnetic flux density along the r-axis for different axial positions, z=0 mm, z=50 mm, z=100 mm and z=140 mm produced by the Maxwell coil with the optimal design according to Tab. VI.5 and Fig. VI.19.a

4.6 Particle Image Velocimetry - PIV

The measurement of the fluid flow field generated by the Lorentz force can be made with several well established non-intrusive techniques such as, the Laser Doppler Anemometry (LDA) also known also Laser Dopper Velocimetry (LDV) [140] and the Particle Image Velocimetry (PIV) [141]. The LDA measures a small region of the space ”single point” at a time with traditionally higher temporal resolution than the PIV. On the other hand, the PIV has higher spatial resolution measuring several points at a time and with the current development, it could match the temporal resolution of the LDA [142]. Therefore the PIV is selected to measure the velocity distribution of the flow field.

The PIV is composed of a camera, a laser and tracer particles in the range of micrometers ($\approx 1 \mu m$) to follow the stream of the flow without inertia. The laser emits two laser beam pulses within a short time interval, which are modified by an optical system to a laser sheet and thus to illuminate a two dimensional plane (r-θ) of the flow. The particles located in the illuminated plane scatter the laser which is recorded by the camera in two images. Then by means of a commercial image processing technique, a cross correlation is computed using these two images to determine a two dimensional displacement vector and thus together with the time delay of the laser beam, the velocity vector field can be reconstructed [141].

The Fig. VI.20 shows the proposed arrangement of the PIV system together with the improved Helmholtz coil arrangement and the electrodes of the crystallizer physical model. In order to illuminate a region of the fluid flow, an aperture has to be made on the outer electrode and thus, the laser sheet can go through the fluid.

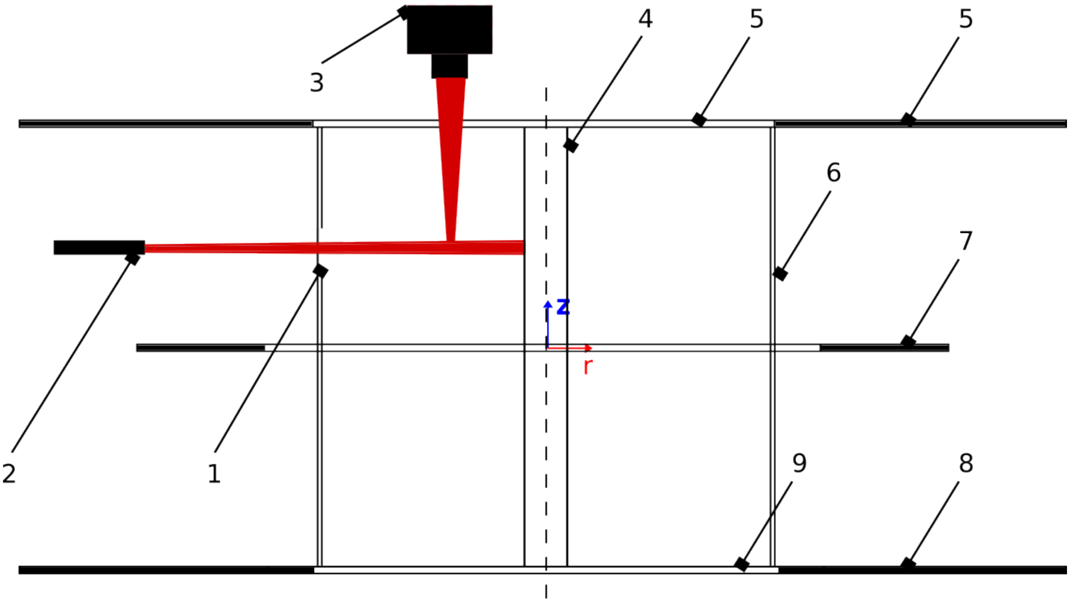

Figure VI.20: Schematic of the improved Helmholtz coil including the PIV system. 1- Aperture in the outer electrode, 2- laser, 3- camera, 4- inner electrode, 5- top cover made of PMMA, 6- outer wall made of PMMA, 7- middle coil, 8- bottom coil, 9- bottom cover made of PMMA.

5 Conclusions

A systematic study of the velocity distribution of an inorganic solution in a crystallizer of annular geometry from the laminar to turbulent regime shows that the RANS models based on the Boussinesq hypothesis need a curvature correction.

The curvature correction modifies the transport equations of the turbulence kinetic energy k, the turbulent rate ε of the $k-\varepsilon$ RNG and $k-\varepsilon$ Realizable models, and the specific dissipation rate ω of the $k-\omega$ SST model. This is necessary because these models don't take into account the disturbances made by the curvatures of the geometry on the turbulent viscosity.

Also, despite the fact that the $k-\varepsilon$ RNG and $k-\varepsilon$ Realizable models contain already corrections to take into account rotating flow, they give similar velocity distribution to the one computed by $k-\omega$ SST model without using the curvature correction in all the models.

When using the curvature correction, the $k-\varepsilon$ RNG, the $k-\varepsilon$ Realizable and the $k-\omega$ SST models resolve properly the velocity distribution with a similar profile to the one computed by the LES with a mean difference of 15 %, 9 % and 9 % respectively. The numerical results of the LES with the WALE subgrid-scale model is used to validate the RANS results because it resolves all the turbulent scales up to the smallest cell of the mesh and models the smaller scales. Therefore, the LES is susceptible to the curvatures of the geometry.

From the three RANS turbulence models, the the RANS $k-\omega$ SST model is submitted to compute the mixing capabilities of the turbulent regime started by the Lorenz force. For this purpose, the trajectories of a group of passive particles are computed, and their positions are used to quantify the mixing grade by means of the stirring index. The stirring index is computed with different number of particles using approx. the maximum box size for each of them, obtaining the same maximum stirring index ≈ 0.60 after 400 seconds.

For the validation of the numerical results, the design of an experimental setup with a special attention on the coil arrangement needing to produce a homogeneous magnetic flux density in the volume of the physical model is required as well as the selection of a measurement system. From three feasible different coil arrangements, the improved Helmholtz coil configuration is chosen because with it, the best homogeneity of the magnetic field along the radial and axial position at a mean magnetic flux density of 8 mT is realizable. Furthermore, the magnetic flux density can be increased up to 10 mT by increasing the electric current on the coils but at the same time using a cooling system (e.g. air blower) to keep the temperature lower than the maximum operation value of the selected copper wire (130 °C).

The PIV is proposed as the measurement system for the velocity distribution because it is a well established non intrusive technique that gives a good spatial and temporal resolution [142].

6 Outlook

The project is focused in the use of the turbulent properties of the fluid flow to enhance the mixing process already started by the azimuthal primary flow created by the Lorentz force density.

Therefore, a further investigation could be made on the different flow structures during the transition to turbulence which could be a new approach to investigate Taylor-Couette flow as well as on the influence of the fluid flow on the ion concentration which in turns affects the local electric conductivity and thus the Lorentz force density.

The particle trajectories computed with the mean part of the flow velocities (chapter III, section 4) by the discrete phase model doesn't include the effects of the fluctuating part of the flow velocities on the dispersion of the particles. This dispersion can be computed with the stochastic tracking model or the particle cloud model (see [2]) and it could play an important role in the mixing process reducing the necessary time to achieve a good homogenization quality (Fig. VI.13).

Another point to investigate is the influence of the fluid flow on the crystallization process which can be made with the population balance model that computes the crystal size distribution, as well as the influence of an open crystallizer (without the top insulator) on the flow structures which can be analyzed as a multiphase flow with the volume of fluid (VOF) model.

CHAPTER VII

General Conclusions and Outlook

During the development of the three projects along this thesis, it is showed that the Lorentz force technique can be used efficiently to influence the flow motion of electrolytes such as molten glasses and inorganic chemical solutions.

The non-negligible electrical conductivity of these fluids allows to impress in them enough electric current density by means of an arrangement of electrodes. Then, by the interaction of this current with an externally generated magnetic flux density is produced a Lorentz force density that can influence significantly the fluid flow. It is showed that the magnetic flux density can be generated with a simple arrangement of coils in all the analyzed cases.

When the fluid is in laminar regime such as the molten glass flow, the Lorentz force density is used to control flow, for the mixing process stretching and folding the fluid flow and to create a push up effect preventing the sinking of minerals used for the coloring of glasses.

When the fluid is in turbulent regime such as the flow of a sodium chloride aqueous solution, the Lorentz force density is used to create a primary flow that starts the mixing process, which is enhanced by the turbulent properties of the flow.

The following sections present a summary of the conclusions and outlooks related to the three different projects.

1 Project I: Electromagnetic mixer

This project is focused on the study of the Lorentz force technique as replacement of the mechanical stirrer used currently in the glass industry, e.g. for the production of optical glass.

The physical model of the electromagnetic mixer is composed of two inner electrodes, one outer electrode and an arrangement of coils located along its axis, and a fluid model. The numerical simulation shows that it is possible to influence the laminar fluid flow, turning the flow around the active inner electrode, following the direction of the Lorentz force density. Therefore, the Lorentz force density is used to stretch and to fold the fluid, necessary conditions to mix a laminar flow because it brings distant parts together and separates close parts.

The mixing capabilities of the electromagnetic mixer is quantified with the stirring index that uses the spatial distribution of passive particles. This stirring index is compared with the stirring index of a highly optimized mechanical stirrer used by SCHOTT AG. Despite the similar values of their stirring indexes, the electromagnetic mixer produces a better homogenization quality of the particle distributions, showing that the electromagnetic mixer could be a better alternative than the mechanical stirrer to mix molten glasses.

In order to validate the numerical results, an experimental study of the physical model using a model fluid is performed. It employs a camera-laser system to record the intensity distribution of the laser scattered from micrometer silicon nitride particles injected in the physical model. The obtained images is used by a self-developed image processing technique to reconstruct the spatial position of the particles for the computation of the experimental stirring index.

Although the experimental stirring index has a close value to the simulated stirring index, the particle distributions are different. This difference comes from the out of focus technique that needs to be recalibrated during the measurements as well as from the thermal effects on the walls of the physical model that is not considered in the simulation. However, this technique is useful to assess by comparison the homogenization obtained by a laminar mixing processes.

The particle detection can be improved using a rectangular outlet channel, eliminating the necessity to correct the position of the particles using the Snell's law as well as by adjustment of the camera focus plane every few steps decreasing the blurring of the particles. Also, the intensity of the scattered laser recorded by the camera can be incremented, decreasing the thickness of the laser sheet using a lithographic technique.

Another point to investigate is the validity of the assumption based on the results of Sugilal Gopalakrisnan [19] that a numerical simulation made in steady mode produces similar results as in transient mode. Also, the validity to use a constant magnetic flux density instead of its distribution along the axis of the physical model must be proved.

The validated numerical model is scaled-up to a real stirring cell using realistic mass flow inlet, wall temperature and temperature-dependent physical properties of molten glass.

The numerical results show that the electrodes in the mixer don't produce large overheating in the molten glass (< 7 K), reducing the impact in the conditioning temperature. Also, the coils are located in the insulation region of the mixer in order to avoid perturbations in the refractory material. And finally, there is no electromagnetic risk for the surrounding equipment due to the relatively low current density and frequency used by the electrodes and coils.

The optimal geometric and electric relations found by Sugilal Gopalakrisnan [19] is not used in the scale-up model because its length is fixed by the length of the electrodes and the diameter by the diameter of the real stirring cell. Therefore, a new parametric analysis to obtain the highest stirring index is performed.

The stirring index of the real stirring cell has a lower value than the stirring index of the physical model, but still competitive with that of the mechanical stirrer. The physical model produces better mixing because it is longer than the real mixer, promoting a more homogeneous distribution.

Along the development of this project several conferences were performed [67, 68, 69].

2 Project II: High performance forehearth

This project is focused on the evaluation of the Lorentz force technique to create a push up effect, preventing the sinking process of the minerals (frits) used to color the molten glass.

The start-up of this project is developed between the TU Ilmenau, FERRO GmbH and Iittala Glass Factory / Fiskars Corp and the second phase of this project is developed between the TU Ilmenau, FERRO GmbH and O-I GLASSPACK GmbH & Co. KG. O-I provided the geometrical data and physical properties of its forehearth as well as the operating parameters and glass samples allowing to build successfully a numerical model of the molten glass flow in a forehearth. Also, the validation of the numerical model with in-situ temperature measurements in the molten glass as well as on the surface of the forehearth, is possible due to this collaboration.

The numerical model predicts with sufficient accuracy the temperature distribution on the surface of the forehearth as well as in the molten glass within the errors of ± 5 K. But, due to the simplification made on the optical properties of the molten glass, the calculated temperatures on the side of the outlet are in the range of ± 10 K.

In a further study, the molten glass must be considered semi-transparent with its optical properties depending on the temperature, to analyze its influence in the heat transfer and thus in the temperature distribution within the molten glass.

The minerals (frits) used to color the molten glass is modeled as passive particles, following the streamlines of the molten glass flow, but they cannot model the sinking process due to the gravity. In order to take into account this process, the molten glass and the frits could be modeled as a multiphase flow that accounts for the diffusion of the frits in the molten glass.

The Lorentz force density is used to create a push up effect to prevent the sinking process of the frits and to improve the input flow conditions of the stirring battery. It is generated with an arrangement of three electrodes and two opposite connected coils to obtain enough push up effect over the total cross section of the O-I forehearth. But, the heat transfer in green glass and the Joule heating created by the impressed electric current density increases the convection in the molten glass, and thereby generates additional negative vertical velocities reducing the push up effect.

The joule heating is decreased having the middle electrode with a larger diameter than in the sides. In order to use the regions where the push effect is more important, the feed tube numbers and positions are changed avoiding regions with additional negative velocities. As a result, the trajectories of the passive particles have final levels higher than the configuration without electrodes at the outlet of the molten glass.

It is expected that the push up effect in white glass will be stronger than in green glass using the same electric currents on the electrodes and coils due to its better internal heat transfer, reducing the temperature gradient, and due to its higher working temperature. Therefore, it will have lower viscosity and higher electric conductivity than green glass obtaining a more intense Lorentz force density and thus a better push up effect.

The push up effect in white glass must be evaluated with a verified numerical model as well as with an appropriate configuration of the electrode and coil arrangements.

Along the development of this project a patent [66], a paper [65] and several conferences [72, 73, 74] were performed.

3 Project III: Electromagnetic crystallizer

This project is focused on the study of the Lorentz force technique as a replacement of the mechanical stirrer used currently in the chemical industry for the mixing of inorganic solutions during the crystallization process.

The physical model of the electromagnetic crystallizer is composed of one inner electrode, one outer electrode and an arrangement of three coils located along its axis, using a fluid model.

The Lorentz force density is used to create a primary flow launching the mixing process, enhanced by the turbulent properties of the fluid flow. A further investigation could be focused on the different flow structures developed during the transition to turbulence which could be a new approach to investigate Taylor-Couette flow. Also, an investigation of the influence of the fluid flow on the ion concentration which in turn affects the Lorentz force density could be made.

The numerical simulation of the fluid flow is made with several RANS turbulence models such as the RNG $k-\varepsilon$, the Realizable $k-\varepsilon$ and the SST $k-\omega$ models. These models need a curvature correction to resolve properly the velocity distribution because they don't take into account the disturbances created by the curvatures of the geometry on the flow.

The mean velocity distribution computed by the RANS turbulence models is validated with the results of a Large Eddy Simulation (LES) using the WALE subgrid-scale model because it resolves the turbulent scales up to the smallest cell of the mesh, which are susceptible to the curvatures of the geometry.

The three RANS turbulence models predict a similar velocity profile to the one obtained by LES, but the SST $k-\omega$ model is chosen to compute mixing capabilities of the turbulent regime because it is a model that suites better this type of flow than the $k-\varepsilon$ models. For this purpose, the discrete phase model is used to compute the trajectories of a group of passive particles, and their positions are used to quantify the mixing grade by means of the stirring index, achieving its maximum value of 0.71 after 400 seconds.

The discrete phase model uses the mean velocity distribution to compute the particle trajectories, but in order to take into account the dispersion of the particles generated by the fluctuating part of the flow velocities, the stochastic tracking model or the particle cloud model could be used. It is important to evaluate this dispersion because it could play an important role in the mixing process, reducing the necessary time to achieve a good homogenization quality.

Also, another point to investigate is the influence of the fluid flow on the crystallization process, which can be made with the population balance model that computes the crystal size distribution. The influence of an open crystallizer (without the top insulator) on the flow structures, which can be analyzed as a multiphase flow with the volume of fluid (VOF) model is yet to be investigated as well.

The validation of the numerical results require an experimental study, but a design of an experimental setup and the measurement system is only proposed. The key part of the experimental design is the selection of the coil arrangements, needing to produce a homogeneous magnetic flux density in the volume of the physical model.

From three feasible different coil arrangements, the improved Helmholtz coil configuration gives the best homogeneity of the magnetic field along the radial and axial position at a mean magnetic flux density of 8 mT. Furthermore, the magnetic flux density can be increased up to 10 mT by increasing the electric current on the coils, but at the same time using a cooling system (e.g. air blower) to control the increase of the temperature.

The PIV is proposed as the measurement system for the velocity distribution because it is a well established non intrusive technique that gives a good spatial and temporal resolution.

Along the development of this project several conferences were performed [71, 70].

APPENDIX A

Navier-Stokes Equation in cylindrical coordinates

The Navier-Stokes equations expressed in vector form can be written in several coordinate systems. The coordinates systems that suite the best to the type type of geometries analyzed along this thesis are the cartesian and cylindrical. Here is only presented the Navier-Stokes equations in cylindrical coordinates because they are used in the analytical analysis of the flow made in the Project II (chapter VI).

In cylindrical coordinates, with the components of the velocity vector $\mathbf{U_{EC}} = (U_{EC,r}, U_{EC,\theta}, U_{EC,z})$, the Navier-Stokes equations (Eq. III.15 and Eq. III.16) take the form:

$$\begin{aligned}\rho_{EC}\left(\frac{\partial U_{EC,r}}{\partial t} + U_{EC,r}\frac{\partial U_{EC,r}}{\partial r} + \frac{U_{EC,\theta}}{r}\frac{\partial U_{EC,r}}{\partial \theta} + U_{EC,z}\frac{\partial U_{EC,r}}{\partial z} - \frac{U_{EC,\theta}^2}{r}\right) = \\ -\frac{\partial p_{EC}}{\partial r} + \eta_{EC}\left(\frac{1}{r}\frac{\partial}{\partial r}\left(r\frac{\partial U_{EC,r}}{\partial r}\right) + \frac{1}{r^2}\frac{\partial^2 U_{EC,r}}{\partial \theta^2} + \frac{\partial^2 U_{EC,r}}{\partial z^2} - \frac{U_{EC,r}}{r^2} - \frac{2}{r^2}\frac{\partial U_{EC,\theta}}{\partial \theta}\right)\end{aligned} \tag{A.1}$$

$$\begin{aligned}\rho_{EC}\left(\frac{\partial U_{EC,\theta}}{\partial t} + U_{EC,r}\frac{\partial U_{EC,\theta}}{\partial r} + \frac{U_{EC,\theta}}{r}\frac{\partial U_{EC,\theta}}{\partial \theta} + U_{EC,z}\frac{\partial U_{EC,\theta}}{\partial z} + \frac{U_{EC,\theta}U_{EC,r}}{r}\right) = -\frac{1}{r}\frac{\partial p_{EC}}{\partial \theta} \\ + \eta_{EC}\left(\frac{1}{r}\frac{\partial}{\partial r}\left(r\frac{\partial U_{EC,\theta}}{\partial r}\right) + \frac{1}{r^2}\frac{\partial^2 U_{EC,\theta}}{\partial \theta^2} + \frac{\partial^2 U_{EC,\theta}}{\partial z^2} - \frac{U_{EC,\theta}}{r^2} + \frac{2}{r^2}\frac{\partial U_{EC,r}}{\partial \theta}\right) - \frac{1}{r}\frac{\sigma_{EC}\varphi_{EC,i}B_{EC}}{ln\left(\frac{D_{EC,i}}{D_{EC,o}}\right)}\end{aligned} \tag{A.2}$$

$$\begin{aligned}\rho_{EC}\left(\frac{\partial U_{EC,z}}{\partial t} + U_{EC,r}\frac{\partial U_{EC,z}}{\partial r} + \frac{U_{EC,\theta}}{r}\frac{\partial U_{EC,z}}{\partial \theta} + U_{EC,z}\frac{\partial U_{EC,z}}{\partial z}\right) = -\frac{1}{r}\frac{\partial p_{EC}}{\partial z} \\ + \eta_{EC}\left(\frac{1}{r}\frac{\partial}{\partial r}\left(r\frac{\partial U_{EC,z}}{\partial r}\right) + \frac{1}{r^2}\frac{\partial^2 U_{EC,z}}{\partial \theta^2} + \frac{\partial^2 U_{EC,z}}{\partial z^2}\right)\end{aligned} \tag{A.3}$$

$$\frac{1}{r}\frac{\partial (rU_{EC,r})}{\partial r} + \frac{1}{r}\frac{\partial U_{EC,\theta}}{\partial \theta} + \frac{1}{r}\frac{\partial U_{EC,z}}{\partial z} = 0 \tag{A.4}$$

References

[1] http://www.schott.com/german/legal2.html. 2015.

[2] http://www.ansys.com. 2015.

[3] http://www.openfoam.com. 2015.

[4] C. Heinicke. Local Lorentz Force Velocimetry for liquid metal duct flows. Ph.D. thesis, Technische Universität Ilmenau, 2012.

[5] D. Cepite, A. Jakovics, B. Halbedel, U. Krieger. Modelling of EM glass convection. COMPEL 27, 387-398, 2008.

[6] D. Hülsenberg, B. Halbedel, G. Conrad, A. Thess. Electromagnetic stirring of glass melts using Lorentz forces - experimental results. Glass Sci. Technol. 77, 186-193, 2004.

[7] U. Krieger, B. Halbedel, D. Hülsenberg, A. Thess. Electromagnetic effects on glass melt flow in crucible. Glass Technol.: Eur. J. Glass Sci. Technol. A 49, 33-40, 2007.

[8] C. Giessler, U. Lange, A. Thess. Non-linear laminar pipe flow of fluids with strongly temperature-dependent material properties. Physics of Fluids 19, 043601, 2007.

[9] C. Giessler, A. Thess, Numerical simulation of electromagnetically controlled thermal convection of glass melt in a crucible. Int. J. Heat Mass Transfer 52, 3373-3389, 2009.

[10] D. Krause, H. Loch. Mathematical simulation in glass technology. Springer, 2002.

[11] C. Giessler. Theoretical investigations of electromagnetic control of glass melt flow. Ph.D. thesis, Technische Universität Ilmenau, 2008.

[12] U. Krieger. Einfluss elektromagnetisch generierter Kraftwirkungen auf die Strömung in Glasschmelzen. PhD thesis, Technische Universität Ilmenau, 2007.

[13] B. Halbedel, U. Krieger, M. Werner, J.O. Torres, U. Schadewald, P. Quiroz. Electromagnetic Processing of Materials at the Department Inorganic-Nonmetallic Materials. Journal of Iron and Steel Research International 19 1/2, 135-140, 2012.

[14] U. Faber, M. Grapentin, K. Wettingfeld. Prüfung elektrischer Anlagen und Betriebsmittel - Grundlagen und Methoden. VDE Verlag, 2012.

[15] C. Kunert, A. Langsdorf, F Lentes, K. Duch, A. Thess, Y. Kolesnikow. Verfahren und Anordnung zur Zufuhr einer Glasschmelze zu einem Verarbeitungsprozess. DE 102004015055 A1, 2004.

[16] B. Halbedel, B, D. Hülsenberg, U. Krieger,U. Lüdtke, G. Carl, H.J. Linz. Verfahren und vorrichtung zur elektromagnetischen beeinflussung der strömungsverhältnisse in gering elektrisch leitfähigen und hochviskosen fluiden. WO 2007065937 A1, 2007.

[17] S. Gopalakrishnan, A. Thess, G. Weidmann, U. Lange. Chaotic mixing in a Joule-heated glass melt. Physics of Fluids 22, 013101, 2010.

[18] S. Gopalakrishnan, A. Thess, Chaotic mixing in electromagnetically controlled thermal convection of glass melt. Chemical Engineering Science 65, 5309-5319, 2010.

[19] S. Gopalakrishnan, A. Thess, Electromagnetically induced chaotic mixing in a pipe mixer. Chemical Engineering Science 65, 6282-6291, 2010.

[20] S. Lim and B. Choi. A study on the MHD (magnetohydrodynamic) micropump with side-walled electrodes. Journal of Mechanical Science and Technology 23, 739-749, 2009.

[21] H. S. Kabbani, A. Wang, X. Luo, S. Qian. Modeling RedOx-based magnetohydrodynamics in three-dimensional microfluidic channels. Physics of Fluids 19,083604, 2007.

[22] Z. P. Aguilara, P. Arumugamb, I. Fritschc. Study of magnetohydrodynamic driven flow through LTCC channel with self-contained electrodes. Journal of Electroanalytical Chemistry 591/2, 201–209, 2006.

[23] A. V. Lemoff, A. P. Lee. An AC magnetohydrodynamic micropump. Sensors and Actuators B 63, 178–185, 2000.

[24] H.H. Bau, J. Zhong, M. Yi. A Minute Magneto Hydro Dynamic (MHD) Mixer. Sensors and Actuators B 79/2-3, 205-213, 2001.

[25] M. Yi, S. Qian, H.H. Bau. A magnetohydrodynamic chaotic stirrer. Journal of Fluid Mechanics 468, 153–177, 2002.

[26] John C. Mauro Edgar D. Zanotto. Two Centuries of Glass Research: Historical Trends,Current Status, and Grand Challenges for the Future. International Journal of Applied Glass Science, 1–15, 2014.

[27] C. A. Angell et Al. Relaxation in glassforming liquids and amorphous solids. J. Appl. Phys., 88/6, 2000.

[28] P. G. Debenedetti, F. H. Stillinger. Supercooled liquids and the glass transition. Nature, 410, 2001.

[29] J. Zarzycki. Glasses and the Vitreous State. Cambridge, 1998.

[30] B. Fischer. Platinum for glass making at Jena. Platinum Metals Rev. 38, 74-82, 1994.

[31] http://www.optstd.org/. 2014.

[32] H. Bach, N. Neuroth. The Properties of Optical Glass. Springer, 1998.

[33] http://www.ifw-dresden.de. 2014.

[34] P. Y. Huang et Al. Direct Imaging of a Two-Dimensional Silica Glass. Graphene Nano Lett. 12, 1081–1086, 2012.

[35] http://www.feve.org. 2014.

[36] http://www.prtr-es.es. 2014.

[37] H. Scholze. Glass: Nature, Structure, and Properties. Springer, First edition, 1991.

[38] A. C. Wright, M. F. Thorpe. Eighty years of random networks. Phys. Status Solidi B, 250, 931–936, 2013.

[39] http://www.glassallianceeurope.eu. 2015.

[40] A. Paul. Chemistry of glasses. Second edition, Chapman and Hall, 1990.

[41] W. Vogel. Structure and Crystallization of Glasses. First edition, Pergamon Pres, 1971.

[42] M. K. Choudhary, R. Venuturumilli, M. R. Hyre. Mathematical Modeling of Flow and Heat Transfer Phenomena in Glass Melting, Delivery, and Forming Processes. International Journal of Applied Glass Science 1-2, 188–214, 2010.

[43] SCHOTT AG. http://www.schott.com. 2015.

[44] W. Martienssen, H. Warlimont. Handbook of Condensed Matter and Materials Data. Springer, 2005.

[45] D. R. Coupland, P. Williams. New Stirrer Technology for the Glass Industry. Platinum Metals Rev. 49/2, 62-69, 2005.

[46] C. Couderc. Platinum Group Metals in Glass Making. Platinum Metals Rev. 54/3, 186–191, 2010.

[47] J. M. Bauer. Forehearth Coloring Advancements, In Proceedings: 68th Conference on Glass Problems, Ohio/ USA, 16-17.10.2007.

[48] Plansee SE. www.plansee.com. 2015.

[49] FERRO GmbH. http://www.ferro.com/NR/rdonlyres/B8C56DE8-5765-4D0A-8F99-99BCB076DAFA/0/GlassColorationMadeEasyAddingValuetoGlass.pdf. 2016.

[50] FERRO GmbH. http://www.ferro.com/Our+Products/ColorsGlass/DecoMaterials/Forehearth+Color+FHC+Technology/Markets.htm. 2016.

[51] D. Ehrt, R. Keding. Electrical conductivity and viscosity of borosilicate glasses and melts. Eur. J. Glass Sci. Technol. B, 50/3, 165–171,2009.

[52] M. Hubert. Basics of industrial glass melting furnaces. http://www.lehigh.edu/imi/teched/GlassProcess/GlassProcessingSpr2015.html, CelSian Glass & Solar B.V, 2015.

[53] L. Shartsis, S. Spinner. Viscosity and Density of Molten Optical Glasses. Journal of Research of the National Bureau of Standards, 46/3, 1951.

[54] SCHOTT AG. http://www.schott.com/advanced_optics/english/download/schott-hh-glasses-october-2013-eng.pdf. 2016.

[55] SCHOTT AG. http://www.schott.com/advanced_optics/chinese/download/schott-optical-glass-pocket-catalog-february-2016-row.pdf. 2016.

[56] B. Bechtloff. Gezielte Beeinflussung der Kinetik von Fest-Flüssig-Reaktionskristallisationen. Ph.D. Thesis, Martin Luther Universität Halle, 2002.

[57] H. Scherzberg, K. Kahle, K. Käseberg. Continuous precipitation and reaction crystallization of inorganic substances in agitated crystallizers with an integrated clarification zone. Chem. Eng. Technol. 21, 412-417, 1999.

[58] H. Martens, H. Hoffmann. Anwendung der Reaktionskristallisation in der Hydrometallurgie und der anorganisch-chemischen Technik. Kristall und Technik 9, 789-798, 1974.

[59] J.W. Mullin. Crystallization, Fourth Edition, Butterworth-Heinemann, 2001.

[60] A.S. Myerson. Handbook of industrial crystallization. Second Edition, Butterworth-Heinemann, 2002.

[61] L.D.Schmidt. The Engineering of Chemical Reactions. First Edition, Oxford University Press, 1998.

[62] D. Thoenes. Chemical Reactor Development: from Laboratory Synthesis to Industrial Production

[63] J. O. Torres, B. Halbedel. High-performance Forehearth Coloring using Lorentz Forces. Technische Universität Ilmenau, Internal Report, 29.02.2012.

[64] J. O. Torres, B. Halbedel. Up-scaling of the Numerical Model of Lorentz Force Application in the Melt Zone on a real Forehearth. Technische Universität Ilmenau, Internal Report, 09.05.2014.

[65] J. O. Torres, B. Halbedel, C. Weber, R. Reche. High-performance Forehearth Coloring using Lorentz Forces. Heat processing, Issue 04, pp. 85 – 89, 2015.

[66] B. Halbedel, J. O. Torres, G. Tünker. Vorrichtung und Verfahren zum elektromagnetisch unterstützten Färben von Glasschmelzen in Speisern von Glasschmelzanlagen. DE 10 2013 017 384.1, angemeldet: 21.10.2013, WO 2015/ 05 8833 A1; angemeldet: 02.10.2014.

[67] J.O. Torres, B. Halbedel. Numerical Study of the effectiveness of an electromagnetic mixer in the glass melt homogenization process. In Proceedings: 11th ESG Conference together with 86th DGG Annual Meeting ICG, Maastricht/ Netherland, 03-06.06.2012.

[68] J.O. Torres, B. Halbedel. A novel electromagnetic mixer for the glass melt homogenization – evaluation with a numerical and physical model. In Proceedings: Workshop Elektroprozesstechnik, Ilmenau/ Ortsteil Heyda, 06-07.09.2012.

[69] J.O. Torres, B. Halbedel. Evaluation of the glass melt homogenization in a feeder channel with the novel electromagnetic mixer technique. In Proceedings: 23th International Congress on Glass, Prague/ Czech Republic, 01-05.07.2013.

[70] J. O. Torres, B. Halbedel. Systematic study of RANS-based turbulence models for the electromagnetic driven flow in an annular inorganic crystallizer. 8. Ansys CFD Hochschultag, Ilmenau / Germany , 26 September 2013.

[71] J.O. Torres, B. Halbedel. Suitable turbulent model for the analysis of the electromagnetic driven flow in an annular inorganic crystallizer. In Proceedings: Workshop Elektroprozesstechnik, Ilmenau/ Ortsteil Heyda, 06-07.09.2013.

[72] J.O. Torres, B. Halbedel. High-performance Forehearth Coloring using Lorentz Forces. In Proceedings: Workshop Elektroprozesstechnik, Ilmenau/ Ortsteil Heyda, 04-05.09.2014.

[73] J.O. Torres, B. Halbedel. High-performance Forehearth Coloring using Lorentz Forces. In Proceedings: 24th International Congress on Glass, Parma/ Italy, 21-25.09.2014.

[74] J.O. Torres, B. Halbedel. A Numerical Approach to High-performance Forehearth Coloring using Lorentz Forces based on a verified Simulation Model. 16th MHD Days, Ilmenau / Germany, 7-9 December, 2015.

[75] S. Soubeih , U. Luedtke , B. Halbedel. Numerical simulation of a glass melting tank with a magnet system to improve the residence time distribution. In Proceedings: 24th International Congress on Glass, Parma/ Italy, 21-25.09.2014.

[76] S. Soubeih , U. Luedtke , B. Halbedel. Improving Residence Time Distribution in Glass Melting Tanks Using Additionally Generated Lorentz Forces. J. Chem. Chem. Eng., 9, 203-210, 2015.

[77] http://www.tu-ilmenau.de/anw/forschung/werkstoffforschung-in-mit-magnetfeldern/. 2015.

[78] J. D. Jackson. Classical Electrodynamics. First Edition, John Wiley & Sons, 1962.

[79] D. J. Griffiths. Introduction to Electrodynamics. Third Edition, Prentice-Hall, 1999.

[80] A. M. Bork. Maxwell, Displacement Current, and Symmetry. Am. J. Phys. 31, 854, 1963.

[81] B. Nacke, A. Muiznieks. Numerical modelling of the industrial silicon single crystal growth processes. GAMM-Mitt., 30/1, 113–124, 2007.

[82] L.D. Landau, E.M. Lifshitz. Fluid Mechanics. Third Edition, Pergamon Press, 1966.

[83] G.K. Batchelor. An Introduction to Fluid Dynamics. First Edition, Cambridge University Press, 2000.

[84] J.H. Spurk, N. Aksel. Fluid Mechanics. Second Edition, Springer, 2008.

[85] S. B. Pope. Turbulent Flows. First Edition, Cambridge University Press, 2000.

[86] N.Rott. Note on the history of the Reynolds number. Annu. Rev. Fluid Mech. 22, 1-11, 1990.

[87] J. C. Rotta. Turbulente Strömungen. Universitätverlag Göttingen, 2010.

[88] R. S. Rogallo, P. Moin. Numerical simulation of turbulent flows. Annual Review of Fluid Mechanics, 16/1, 99–137, 1984.

[89] P. A. Davidson. An Introduction to Magnetohydrodynamics. First Edition, Cambridge University Press, 2001.

[90] Incropera et Al. Fundamentals of Heat and Mass Transfer. Sixth Edition, John Wiley & Sons, 2007.

[91] R.Siegel, J.R. Howell. Thermal Radiation Heat Transfer. Third Edition, Hemisphere Publishing Corporation, 1992.

[92] S. Chandrasekhar. Radiative Transfer. Third Edition, Dover Publications Inc, 1960.

[93] S.V. Patankar. Numerical Heat Transfer and Fluid Flow. First Edition, Hemisphere Publishing Corporation, 1980.

[94] B. J. van der Linden. Radiative heat transfer in glass: the algebraic ray trace method. Ph.D. thesis,Technische Universiteit Eindhoven, 2002.

[95] K. T. Alligood, T. D. Sauer J. A. Yorke. CHAOS: An Introduction to Dynamical Systems. Springer, 1996.

[96] H. Goldstein, C. Poole, J. Safko. Classical mechanics, Third edition, Addison Wesley, 2000.

[97] Krause, Loch. Mathematical Simulation in Glass Technology, Springer, 2002.

[98] J. M. Ottino. The mixing of fluids. Scientific American, 1989.

[99] J. M. Ottino. Mixing, Chaotic Advection, and Turbulence. Annu. Rev. Fluid Mech. 22, 207-53, 1990.

[100] H. Aref. Chaotic Advection of Fluid Particles. Phil. Trans. R. Soc. Lond. A 333, 273-288, 1990.

[101] H. J. Kim, A. Beskok. Quantification of chaotic strength and mixing in a micro fluidic system. J. Micromech. Microeng. 17, 2197-2210, 2007.

[102] V. Geža A. Jakovičs, U. Krieger, B. Halbedel. Modelling of electromagnetic heating and mixing conditions in glass melt output equipment. COMPEL - The international journal for computation and mathematics in electrical and electronic engineering, 30/5, 1467-1478, 2011.

[103] E. B. Nauman. Residence Time Theory. Ind. Eng. Chem. Res.,47/10, 2008.

[104] M. Leidel. Optische Bewertung der Homogenisierungswirkung von Rührmethodenals Beitrag für die Optimierung von Glasschmelztechnologien. Diplomarbeit, TU-Ilmenau, 2012.

[105] C. Schmitt. Aufbau eines physikalischen Modells – Vergleich mechanisches und elektromagnetisches Rühren von Glasschmelzen, TU-Ilmenau, Institut für Werkstofftechnik, FG Anorganisch-nichtmetallische Werkstoffe, Studienarbeit, 2012.

[106] B. Halbedel. Werkstoff- und Verfahrensentwicklung zur Herstellung und Applikation neuartiger hartmag-netischer Magnetobeads in der chemischen und biologischen Technik. Abschlußbericht AiF-Projekt, TU Ilmenau, Institut für Werkstofftechnik, FG Glas- und Keramiktechnologie, 30.04.2003.

[107] G. S. Bratsch. Standard electrode potentials and temperature coefficients in water at 298.15 K J. Phys. Chem. 18 / 1, 1989.

[108] Zemax LLC. http://www.zemax.com. 2015

[109] Plansee SE. www.plansee.com. 2015

[110] OWIS GmbH. http://www.owis.eu. 2015

[111] Digia Plc. http://www.qt.io. 2015

[112] Canon Inc. https://www.usa.canon.com/cusa/consumer/standard_display/sdk_homepage. 2015.

[113] OpenCV. http://opencv.org. 2015.

[114] ISO 12123:2010. Optics and photonics — Specification of raw optical glass. International organization for standardization, Second edition, 2010.

[115] E. C. JR. Baukal, Heat transfer in industrial combustion, Florida, CRC Press LLC 2000.

[116] E. Litovsky, M. Shapiro, A. Shavit, Gas pressure and temperature dependences of thermal conductivity of porous ceramic materials: Part 2, refractories and ceramics with porosity exceeding 30%. J. Am. Ceram. Soc. 79 (5), 1366-1376, 1996.

[117] D. C. Phan, Optimierung thermischer Prozesse bei der Glasproduktion durch Modellierung und Simulation. Dissertation. Universität Bayreuth, 2007.

[118] Lawrence Berkeley national laboratory, http://www.lbl.gov, 2014.

[119] J. Pischke, Wärmestrommessungen an opaken Quarzglas-Flanchen. Experimentelle Studienarbeit, Technische Universität Claushal, 1994.

[120] P. Boulet, et al., Experimental Investigation of Radiation Emitted by Optically Thin to Optically Thick Wildland Flames. Journal of Combustion, 137437, 2011.

[121] A. P. Roychowdhury, J. Srinivasan, The modelling of radiation heat transfer in forehearths units in glass melting. Wärme- und Stoffübertragung 30, 71-75, 1994.

[122] G.D. Raithby and E.H. Chui. A Finite-Volume Method for Predicting a Radiant Heat Transfer in Enclosures with Participating Media. J. Heat Transfer, 112, 415–423, 1990.

[123] J. O. Torres, B. Halbedel. Numerical Study of EM Controlled Flow in Crystallizers of Inorganic Materials. Technische Universität Ilmenau, Technische Universität Ilmenau, Internal Report, 15.12.2010.

[124] P. S. Marcus. Simulation of Taylor-Couette flow. Part 1. Numerical methods and comparison with experiment. J . Fluid Mech., 146, 45-64, 1984.

[125] P. S. Marcus. Simulation of Taylor-Couette flow. Part 2. Numerical results for wavy-vortex flow with one travelling wave.. J. Fluid Mech., 146, 65-113, 1984.

[126] D.C. Wilcox. Turbulence Modeling for CFD, third edition, DCW Industries, 2006.

[127] P. K. Kundu, I. M. Cohen. Fluid Mechanics, second edition, Academic Press,2002.

[128] W. S. Saric. Görtler vortices. Annu. Rev. Fluid Mech., 26, 379-409, 1994.

[129] S. Altmeyer, Y. Do, Y. C.Lai. Transition to turbulence in Taylor-Couette ferrofluidic flow. Sci. Rep. 5, 10781, doi: 10.1038/srep10781, 2015.

[130] http://www.femm.info. 2015.

[131] http://www.k-utec.de/fileadmin/redakteur/Dowloads/Veroeffentlichungen_und _Praesentationen/Precipitation1.pdf. 2015.

[132] www.k-utec.de. 2015.

[133] J. Wang, S. She, S. Zhang. An improved Helmholtz coil and analysis of its magnetic field homogeneity. Rev. Sci. Instrum. 73, 2175, 2002.

[134] M. E. Somervuori, M. T. Alenius, H. E. Hänninen, R. Karppi. Corrosion fatigue of spot-welded austenitic stainless steels in 3.5% NaCl solution. Materials and Corrosion, 55, 921–929. 2004.

[135] K. Amouzegar, G.S. Amant, S. Harrison. Process for the purification of lithium carbonate. US6048507 A, 2007.

[136] Ronald M. C. So and George L. Mellor, Experiment on convex curvature effects in turbulent boundary layers, J. Fluid Mech., 60, 43–62, 1973.

[137] K. C. Muck, P. H. Hoffmann and P. Bradshaw. The effect of convex surface curvature on turbulent boundary layers, J. Fluid Mech., 161, 347–369, 1985.

[138] L. Temmerman, M. Hadžiabdić, M. A. Leschziner, K. Hanjalić. A hybrid two-layer URANS-LES approach for large eddy simulation at high Reynolds numbers. Int. J. Heat and Fluid Flow, 26, 173-190, 2005.

[139] S. Abawi. Messberichte. Unveröffentlichtes Dokument. TU Ilmenau, Fachgebiet Anorganisch-nichtmetallische Werkstoffe, 19.05.2012.

[140] Z. Zhengji. LDA Application Methods: Laser Doppler Anemometry for Fluid Dynamics. Springer-Verlag, 2010.

[141] M. Raffel, C. E. Willert, J. Kompenhans. Particle image velocimetry. Springer-Verlag, first edition, 1998.

[142] P. Mattern, S. Sieber,M. Dues, S. Caglar,M. Gabi. Simultaneous High Speed Stereo PIV and LDA Measurements in the highly transient vortical wake of an axial fan. In Proceedings: 16th Int Symp on Applications of Laser Techniques to Fluid Mechanics, Lisbon/ Portugal, 09-12.07.2012.

List of Figures

List of Tables

Nomenclature

Symbol	Description
$\mathbf{A_{ef}}$	magnetic vector potential [T·m]
A_η	fitting constant of the Vogel-Tammann-Fulcher equation [1]
A_ρ	fitting constant of the equation for the density [1]
A_σ	fitting constant of the equation for the conductivity [1]
B_η	fitting constant of the Vogel-Tammann-Fulcher equation [1]
B_ρ	fitting constant of the equation for the density [1]
B_σ	fitting constant of the equation for the conductivity [1]
$\mathbf{B_{ef}}$	eigenfeld [T]
$\mathbf{B_e}$	externally created magnetic flux density [T]
$\mathbf{B}$	total magnetic flux density [T]
$\hat{\mathbf{B}}_\mathbf{e}$	steady part of $\mathbf{B_e}$ [T]
$B_{PM,z}$	axial component of the magnetic flux density of the electromagnetic mixer physical model [mT]
$\mathbf{B_{OI}}$	magnetic flux density of the high performance forehearth [mT]
$\mathbf{B_{EC}}$	magnetic flux density of the crystallizer physical model [mT]
$B_{EC,z}$	axial component of the magnetic flux density of the crystallizer physical model [mT]
B_{EC}	mean magnetic flux density of the crystallizer physical model [mT]
B_F	width of the high performance forehearth [m]
B_G	glass melt width of the high performance forehearth [m]
b_F	refractory width of the high performance forehearth [m]
C_s	constant of Smagorinski-Lilly model [1]
C_k	parameter of the WALE model [1]

Symbol	Description
C_ω	cross diffusion term [Kg/(m^{3}s^2)]
C_{lw}	constant of the law of the wall ≈ 5 [1]
C_μ	constant of the $k-\varepsilon$ models [1]
Cp_{RF}	specific heat capacity of the molten glass used in the real feeder [J/(K·Kg)]
Cp_G	specific heat capacity of the molten glass used in the high performance forehearth [J/(K·Kg)]
Cp_{EC}	specific heat capacity of the fluid model used in the crystallizer physical model [J/(K·Kg)]
c_0	speed of light in vacuum [m/s]
c_p	specific heat capacity [J/(K·Kg)]
D_{AG}	diameter of the SCHOTT AG stirring cell [m]
D_{PM}	diameter of the electromagnetic mixer physical model [m]
$D_{EC,i}$	diameter of the inner electrode of the crystallizer physical model [mm]
$D_{EC,o}$	diameter of the outer electrode of the crystallizer physical model [mm]
D_k	dissipation of k [kg/(s^{3}m)]
D_ω	dissipation of ω [Kg/(m^{3}s^2)]
d_{PM}	distance between inner electrodes of the electromagnetic mixer physical model [m]
d_{cf}	distance between the center and the face of the cell [m]
dl	is a line element of the coil [m]
$d(t)$	total distance between particles [m]
d_w	closest distance to the wall [m]
$d_{50,3}$	particle size [μm]
$\mathbf{E}$	electric field [V/m]
$\mathbf{E_i}$	induced electric field [V/m]
F	state function [1]
Fr	Froud number [1]
$F_3(d)$	mean particle size distribution [1]
f	frequency [Hz]
f_{EC}	frequency of the applied electric current on the coils of the crystallizer physical model [Hz]
f_{cc}	curvature correction [1]
f_{RTD}	residence time distribution [s]
F_{RTD}	cumulative of the residence time distribution [s]
$\mathbf{f_{L,ef}}$	Lorentz force density related to the eigenfeld [N/m^3]
$\mathbf{f_L}$	total Lorentz force density [N/m^3]

Symbol	Description
$\mathbf{f_{L,ef}}$	natural Lorentz force density [N/m^3]
$\mathbf{f_{L,PM}}$	Lorentz force density of the electromagnetic mixer physical model [N/m^3]
$\mathbf{f_{L,OI}}$	Lorentz force density of the high performance forehearth [N/m^3]
$\mathbf{f_{L,EC}}$	Lorentz force density of the crystallizer physical model [N/m^3]
G	filter function [1]
$\mathbf{g}$	gravitational acceleration 9.81 [m/s^2]
$\dot{\mathbf{g}}$	dimensionless gravitational acceleration [1]
$H_3(d)$	mean frequency distribution [1]
H_F	height of the high performance forehearth [mm]
H_G	molten glass level of the high performance forehearth [mm]
h_F	refractory height of the high performance forehearth [mm]
h_{EC}	height of the crystallizer physical model [mm]
$h_{EC,m}$	distance from the middle coil to the top and bottom coil of the crystallizer physical model [mm]
h	Planck constant 6.63x10^{-34} [m^{2}Kg/s]
I_δ	identity matrix [1]
I	electric current [A]
$I_{PM,E}$	electric current in the fluid model used in the electromagnetic mixer physical model [A]
$I_{PM,C}$	electric current in the coils of the electromagnetic mixer physical model [A]
$I_{EC,C}$	electric current in the coils of the crystallizer physical model [A]
$\mathbf{J}$	electric current density [A/m^2]
$\hat{\mathbf{J}}$	steady part of $\mathbf{J}$ [A/m^2]
$\mathbf{J_{L,PM}}$	electric current density in the fluid model used in the electromagnetic mixer physical model [A/m^2]
$\mathbf{J_{OI}}$	electric current density in the molten glass of the high performance forehearth [A/m^2]
K	number of boxes
k	turbulent kinetic energy [m^2/s^2]
k_B	Boltzmann constant 1.38x10^{-23} [$m^2Kgs^{-2}K^{-1}$]
k_c	thermal conductivity [W/(m·K)]
k_{RF}	effective thermal conductivity of the molten glass used in a real feeder [W/(m·K)]
L_{sgs}	parameter of Smagorinski-Lilly model [m]
L_{AG}	length of the SCHOTT AG stirring cell [m]
L_{PM}	length of the electromagnetic mixer physical model [m]

Symbol	Description
L_{FS}	distance between the feed tubes and the stirring battery of the high performance forehearth [m]
L	characteristic length of the system [m]
L_{EC}	inductance of the coils of the crystallizer physical model [Vs/A]
l_k	Kolmogorov length scale [m]
$l(t)$	distance between particles over time [m]
M	square of the modified Hartmann number [1]
M_{PM}	square of the modified Hartmann number of the electromagnetic mixer physical model [1]
M_{EC}	square of the modified Hartmann number of the crystallizer physical model [1]
m	mean number of particles [1]
$\dot{m}$	volumetric flow rate [m^3/s]
$\dot{m}_{FM}$	volumetric flow rate of the fluid model used in the electromagnetic mixer physical model [ml/min]
$\dot{m}_G$	pull rate of the molten glass used in the high performance forehearth [t/d]
N	total number of particles [1]
N_{ip}	interaction parameter [1]
N_d	total number of mesh points [1]
N_{PM}	dimensionless switching frequency about the inner electrodes of the electromagnetic mixer physical model [1]
n	current time level [t]
n_i	number of particles in the box i [1]
n_w	unitary vector normal to the wall [1]
n_r	refractive index [1]
n_p	refractive index of PMMA [1]
n_f	refractive index of the fluid model used in the electromagnetic mixer physical model [1]
n_a	refractive index of the air [1]
n_G	refractive index of the molten glass used in the high performance forehearth [1]
Pe	Péclet number number [1]
Pr	Prandtl number [1]
P_ω	production of ω [Kg/(m^{3}s^2)]
P_k	production of k [kg/(s^{3}m)]
P_G	total thermal power carry by the molten glass used in the high performance forehearth [W]
P_B	total thermal power produced by the burners the high performance forehearth [W]

Symbol	Description
$P_{EC,T}$	total power of the coils of the crystallizer physical model [W]
$P_{EC,R}$	Ohmic losses of the coils of the crystallizer physical model [W]
p	pressure [Pa]
p_{EC}	pressure of fluid model used by the crystallizer physical model [Pa]
$\dot{p}$	dimensionless pressure [1]
$\bar{p}$	mean part of the instantaneous p [Pa]
$\widetilde{p}$	filtered or resolved part of p [Pa]
p'	fluctuating or residual part of p [Pa]
p_v	volumetric heat source [W/m^3]
$q_{r,0}$	reference radiative heat flux density [W/m^2]
q_{cv}	convective heat flux [W/m^2]
q_c	conductive heat flux [W/m^2]
q_b	radiative heat flux density for the black body [W/m^2]
q_r	radiative heat flux [W/m^2]
$\mathbf{r}$	position variable [m]
Re	Reynolds number [1]
Re_{AG}	Reynolds number of the SCHOTT AG stirring cell [1]
Re_{PM}	Reynolds number of the electromagnetic mixer physical model [1]
Re_{EC}	Reynolds number of the crystallizer physical model [1]
R_{EC}	resistance of the coils of the crystallizer physical model [Ω]
r_{EC}	radius of the Helmholtz coil arrangement of the crystallizer physical model [m]
St	Strouhal number [1]
S	surface vector [m^2]
$\bar{\bar{\mathrm{S}}}$	mean shear stress tensor [1/s]
$\bar{\bar{\mathrm{S}}}_{\mathrm{sgs}}$	filtered shear stress tensor [1/s]
s_{ST}	local stretch ratio [1]
T	temperature [K]
T_0	parameter of the Vogel-Tammann-Fulcher equation [1]
T_g	transformation temperature [K]
T_m	melting point temperature [K]
T_s	surface temperature [K]
T_∞	surrounding air temperature [K]
T_G	temperature of the molten glass used in the high performance forehearth [°C]
T_F	temperature of the surface of the high performance forehearth [°C]

Symbol	Description
$\bar{\bar{\mathbf{T}}}$	shear stress tensor [Pa]
t	time [s]
$\dot{t}$	dimensionless time [1]
t_k	Kolmogorov time scale [s]
t_{RTD}	residence time [s]
$\bar{t}_{RTD}$	mean residence time [s]
$t_{EC,p}$	particle residence time of the crystallizer physical model [s]
$\bar{\mathbf{U}}$	mean part of $\mathbf{U}$ [m/s]
$\mathbf{u}'$	fluctuating part or residual part of $\mathbf{U}$ [m/s]
$\mathbf{U}$	instantaneous velocity vector field [m/s]
$\dot{\mathbf{U}}$	dimensionless instantaneous velocity vector field [1]
$\widetilde{\mathbf{U}}$	filtered or resolved part of $\mathbf{U}$ [m/s]
U_c	velocity at the cell center [m/s]
U_f	velocity at the faces of the cell [m/s]
$U_{FM,z}$	mean axial velocity of the fluid model used in the electromagnetic mixer physical model [mm/s]
$U_{G,z}$	axial velocity of the molten glass of the high performance forehearth [mm/s]
U_{EC}	velocity magnitude of fluid model used by the crystallizer physical model [cm/s]
$U_{EC,\theta}$	azimuthal velocity component of fluid model used by the crystallizer physical model [cm/s]
$U_{EC,z}$	axial velocity component of fluid model used by the crystallizer physical model [cm/s]
$U_{EC,r}$	radial velocity component of fluid model used by the crystallizer physical model [cm/s]
u_k	Kolmogorov velocity scale [m/s]
u_τ	friction velocity [m/s]
u^+	dimensionless velocity [1]
V	volume [m^3]
w_{EC}	coil winding numbers of the crystallizer physical model [1]
$w_{EC,m}$	middle coil winding number of the Maxwell arrangement of the crystallizer physical model [1]
y_s	dimensionless distance from the wall surface [m]
y^+	dimensionless distance from the wall surface [1]

Symbol	Description
α	heat transfer coeffcient [W/(m^{2}K)]
β	closure coefficient of the SST $k-\omega$ model [1]
β^*	closure coefficient of the SST $k-\omega$ model [1]
γ	closure coefficient of the SST $k-\omega$ model [1]
δ_τ	length scale [m]
ε	dissipation rate [m^2/s^3]
ε_r	emissivity [1]
ε_G	emissivity of the molten glass used in the high performance forehearth [1]
ε_e	permitivity [F/m]
ε_{SI}	stirring index [1]
η	dynamic viscosity [Pas]
η_{AG}	dynamic viscosity of the molten glass used in the SCHOTT AG stirring cell [Pas]
η_{FM}	dynamic viscosity of the fluid model used in the electromagnetic mixer physical model [Pas]
η_{RF}	dynamic viscosity of the molten glass used in a real feeder [Pas]
η_G	dynamic viscosity of the molten glass used in the high performance forehearth [Pas]
η_{EC}	dynamic viscosity of the fluid model used in crystallizer physical model [Pas]
η_t	turbulent viscosity [Pas]
η_{sgs}	turbulent viscosity of LES [Pas]
κ	Von Kármán constant ≈ 0.41 [1]
λ	wavelength [m]
λ_L	Lyapunov exponent [1]
λ_s	slop of the local stretch ratio [1]
λ_{alfons}	lambda Alfons [1]
λ_G	thermal conductivity of the molten glass used in the high performance forehearth [W/(m·K)]
λ_{EC}	thermal conductivity of the fluid model used in crystallizer physical model [W/(m·K)]
μ_0	magnetic permeability $4\pi \times 10^{-7}$ [N/A^2]
ν	cinematic viscosity [m^2/s]
ξ	parameter of viscosity [Pas]

Symbol	Description
ρ	density [Kg/m^3]
ρ_{AG}	density of the molten glass used in the SCHOTT AG stirring cell [Kg/m^3]
ρ_{FM}	density of the fluid model used in the electromagnetic mixer physical model [Kg/m^3]
ρ_{RF}	density of the molten glass used in a real feeder [Kg/m^3]
ρ_G	density of the molten glass used in the high performance forehearth [Kg/m^3]
ρ_{EC}	density of the fluid model used in crystallizer physical model [Kg/m^3]
ρ_e	electric charge density [C/m^3]
σ	electrical conductivity [S/m]
σ_{FM}	electrical conductivity of the fluid model used in the electromagnetic mixer physical model [S/m]
σ_{RF}	electrical conductivity of the molten glass used in a real feeder [S/m]
σ_G	electrical conductivity of the molten glass used in the high performance forehearth [S/m]
σ_{EC}	electrical conductivity of the fluid model used in crystallizer physical model [S/m]
σ_s	Stefan-Boltzmann constant 5.67x10^{-8} [$Wm^{-2}K^{-4}$]
σ_{RTD}	standard deviation of the residence time distribution [s]
σ_k	closure coefficient of the SST $k-\omega$ model [1]
σ_ω	closure coefficient of the SST $k-\omega$ model [1]
τ_{PM}	shifting period about the inner electrodes of the electromagnetic mixer physical model [t]
τ_w	wall shear stresses [Pa]
θ_{JB_e}	angle between $\mathbf{J}$ and $\mathbf{B_e}$
$\varphi_{EC,o}$	electric potential applied on the outer electrode of the crystallizer physical model [V]
$\varphi_{EC,i}$	electric potential applied on the inner electrode of the crystallizer physical model [V]
Ω	control volume [m^3]
ω	specific dissipation rate [1/s]
∇	gradient operator [1/m]
$\dot{\nabla}$	dimensionless gradient operator [1/m]
$\nabla\times$	rotational operator [1/m]
$\nabla\cdot$	divergence operator [1/m]
$\dot{\nabla}\cdot$	dimensionless divergence operator [1]

Erklärung

Ich versichere, dass ich die vorliegende Arbeit ohne unzulässige Hilfe Dritter und ohne Benutzung anderer als der angegebenen Hilfsmittel angefertigt habe. Die aus anderen Quellen direkt oder indirekt übernommenen Daten und Konzepte sind unter Angabe der Quelle gekennzeichnet.

Bei der Auswahl und Auswertung folgenden Materials haben mir die nachstehend aufgeführten Personen in der jeweils beschriebenen Weise unentgeltlich geholfen:

1. Die fachliche Betreuung der Arbeit erfolgte durch Dr. Bernd Halbedel und Prof. Dr. André Thess.
2. Dr. Bernd Halbedel hat den Dissertationsentwurf korrekturgelesen.
3. Die Messungen der Magnetischen Flussdichte im Physikalischen Modell des Projektes I "Elecromagnetic mixer" (Kapitel IV) wurden Unterstützung des Studenten, Herrn Daniel Löw der TU Ilmenau im Rahmen seiner studentischen Hilfkrafttätigkeit durchgefürt.

Weitere Personen waren an der inhaltlich-materiellen Erstellung der vorliegenden Arbeit nicht beteiligt. Insbesondere habe ich hierfür nicht die entgeltliche Hilfe von Vermittlungs- bzw. Beratungsdiensten (Promotionsberater oder anderer Personen) in Anspruch genommen. Niemand hat von mir unmittelbar oder mittelbar geldwerte Leistungen für Arbeiten erhalten, die im Zusammenhang mit dem Inhalt der vorgelegten Dissertation stehen.

Die Arbeit wurde bisher weder im In- noch im Ausland in gleicher oder ähnlicher Form einer Prüfungsbehörde vorgelegt.

Ich bin darauf hingewiesen worden, dass die Unrichtigkeit der vorstehenden Erklärung als Täuschungsversuch bewertet wird und gemäß §7 Abs. 10 der Promotionsordnung den Abbruch des Promotionsverfahrens zur Folge hat.

Ilmenau, den 01.07.2016 Jose Oskar Torres Perez